PONTIFICIA UNIVERSIDAD CATOLICA DE CHILE
ESCUELA DE INGENIERIA

HEMODYNAMIC AND BIOMECHANICS ASSESSMENT OF THE HEART AND GREAT VESSELS BY CARDIOVASCULAR MAGNETIC RESONANCE IMAGING

PAMELA ALEANDRA FRANCO LEIVA

Thesis submitted to the Office of Graduate Studies
In partial fulfillment of the requirements for the Degree of
Doctor in Engineering Sciences

Advisor:
SERGIO ANDRÉS URIBE ARANCIBIA

Santiago de Chile, June 2022

PONTIFICIA UNIVERSIDAD CATOLICA DE CHILE
ESCUELA DE INGENIERIA

HEMODYNAMIC AND BIOMECHANICS ASSESSMENT OF THE HEART AND GREAT VESSELS BY CARDIOVASCULAR MAGNETIC RESONANCE IMAGING

PAMELA ALEANDRA FRANCO LEIVA

Members of the Committee:

SERGIO URIBE

MARCELO ANDIA

DIEGO CELENTANO

RODRIGO SALAS

JULIO GARCIA

GUSTAVO LAGOS

Thesis submitted to the Office of Graduate Studies in partial fulfillment of the requirements for the Degree Doctor in Engineering Sciences

Santiago de Chile, June, 2022

“A mis Padres: Leonor y Robinson.”

ACKNOWLEDGEMENTS

"In long-distance running the only opponent you have to beat is yourself, the way you used to be."

Haruki Murakami, *What I Talk About When I Talk About Running*.

This is the result of a remarkable journey, through time, the steps of which I can not go back or redo, full of memories; valuable or insignificant depending on the moment, but that would not have been possible without pillars that illuminated with signs the uncertain path that I followed many times. Therefore, I would like to thank all people who contributed directly or indirectly to the development of this research. First, to my advisor Sergio Uribe, professors, especially Rodrigo Salas and Cristóbal Bertoglio, and Biomedical Imaging Center teammates for the opportunity, support, motivation, and patience to perform this thesis.

I gratefully acknowledge my family, especially my parents (Leonor Leiva and Robinson Franco) and grandparents (Celinda Cataldo and Caupolicán Leiva), my faithful hairy friends (La Gorda and Momo), and my friends, especially: Carlos Rojas, Melissa Benítez, Sergio Manzano, and Cristian Montalba. And to all those who have already left but will never be forgotten.

Hence, I would like to thank to ANID-PCHA/Doctorado-Nacional/2018-21180391, CONICYT-PIA-Anillo ACT1416, and ANID-Millennium Science Initiative Program-NCN17_129.

TABLE OF CONTENTS

LIST OF FIGURES

LIST OF TABLES

ABSTRACT

Cardiac magnetic resonance imaging (MRI) is the gold standard technique for assessing cardiac function. Moreover, cardiac MRI also provides a unique technique called 4D Flow MRI that includes velocity images of the three-orthogonal planes within a 3D volume for the entire cardiovascular system throughout the cardiac cycle. It allows obtaining several hemodynamic parameters providing the evaluation of several cardiovascular diseases. Nevertheless, 4D Flow MRI and processing methods suffer from several issues, e.g., prolonged scanning times, incorrect flow measurements, and missing the clinical relevance through calculating several hemodynamic parameters. In this Thesis, three research articles intended to tackle some of these previous issues.

The first article compares the uni-directional Dual Velocity-Encoding (VENC) PC-MRI methods for different noise levels and proposes a correction algorithm for the Optimal Dual-VENC (Carrillo *et al.,* 2018), which is based on theoretical considerations.

The second article describes a methodology for quantitative evaluation of intraventricular hemodynamics using a single segmentation from a 4D Flow dataset and a finite-element method. Our approach was able to identify abnormal flow patterns in a small cohort of dilated cardiomyopathy patients and can be applied to any other cardiovascular disease.

The third article provides a comprehensive overview of the relative performance of different machine learning algorithms applied over 4D flow data for bicuspid aortic valve aortopathy classification. For that purpose, we analyzed and extracted multiple correlation patterns of hemodynamic parameters, finding which parameters showed high collinearity between them, which allows us to diminish their size to a few variables.

This investigation of this thesis for assessing different Dual-VENC reconstruction techniques, image processing, data quantification, pattern recognition, and machine

learning in three independent articles. Thought the fact that the topics aborded in the articles were not tested together, future research may combine all these topics to investigate and improve the examination in the cardiovascular system.

Keywords: Cardiovascular MRI, 4D Flow MRI, Hemodynamic Parameters, Unwrapping Methods in Dual-VENC MRI, Flow Quantification, Pattern Recognition, Machine Learning

RESUMEN

La resonancia magnética (RM) cardíaca es la técnica estándar para evaluar la función cardíaca. Además, la RM cardíaca también proporciona una técnica única llamada RM de flujo 4D que incluye imágenes de velocidad de los tres planos ortogonales dentro de un volumen 3D para todo el sistema cardiovascular a lo largo del ciclo cardíaco. Permite obtener varios parámetros hemodinámicos proporcionando la evaluación de varias enfermedades cardiovasculares. No obstante, los métodos de procesamiento de imágenes de RM de flujo 4D sufren varios problemas, por ejemplo, tiempos de exploración prolongados, mediciones de flujo incorrectas y falta de relevancia clínica al calcular varios parámetros hemodinámicos. Por ello, tres artículos de investigación pretenden abordar algunos de estos problemas.

El primer artículo compara los métodos unidireccionales de codificación de velocidad dual en PC-MRI para diferentes niveles de ruido agregado y propone una corrección para el método de Optimal Dual-VENC (Carrillo *et al.*, 2018) que se basa en consideraciones teóricas.

El segundo artículo describe una metodología para la evaluación cuantitativa de la hemodinámica intraventricular utilizando una segmentación única de un conjunto de datos de flujo 4D y un método de elementos finitos. Nuestro enfoque fue capaz de identificar patrones de flujo anormales en una pequeña cohorte de pacientes con miocardiopatía dilatada y puede aplicarse a cualquier otra enfermedad cardiovascular.

El tercer artículo proporciona una descripción general completa del rendimiento relativo de diferentes algoritmos de aprendizaje de máquinas sobre datos de flujo 4D para la clasificación de la aortopatía de la válvula aórtica bicúspide. Para ello, analizamos y calculamos múltiples patrones de correlación de parámetros hemodinámicos, encontrando qué parámetros presentaban alta colinealidad entre ellos, lo que nos permite reducir su tamaño a unas pocas variables.

Esta investigación analizó información relevante sobre técnicas de reconstrucción, procesamiento de imágenes, cuantificación de datos, reconocimiento de patrones y aprendizaje de máquinas en tres artículos independientes. Aunque los temas abordados en los artículos no fueron probados en conjunto, investigaciones futuras podrían combinar los tópicos abordados en esta Tesis con el objeto de mejorar el diagnóstico del sistema cardiovascular.

Palabras Claves: RMI cardiovascular, Flujo 4D, Parámetros Hemodinámicos, Métodos de Desenvolvimiento en RMI Dual-VENC, Cuantificación de Flujo, Reconocimiento de Patrones, Aprendizaje de Máquinas

1. INTRODUCTION

Cardiovascular diseases have the highest worldwide mortality rates, representing 32% of all global deaths (World Health Organization, 2019). It is known that changes in anatomy and hemodynamic affect the cardiovascular system's performance (Mark *et al.,* 2012). Particularly, blood flow is an important factor in gaining insight into the occurrence and progression of this disease (Al-Wakeel *et al.,* 2015).

Modern imaging techniques such as Cardiac Magnetic Resonance (CMR) are now routinely being used to evaluate the function and structure of the cardiovascular system (Frangi *et al.,* 2007). Furthermore, a 4D Flow Magnetic Resonance Imaging (MRI) technique has become available over the last years (Markl *et al.,* 2012). This technique allows visualization and quantification of velocity-related parameters in all major blood vessels and the whole heart, time-resolved over the cardiac cycle (Wu *et al.,* 2004). Visualization tools aim to display the direction and magnitude of the blood flow velocity from 4D Flow data by using a vector glyph or streamline representation or by constructing pathlines from particle tracing (Wigstrom *et al.,* 1999) (Kvitting *et al.,* 2004) (Markl *et al.,* 2007) (Stalder *et al.,* 2008) (Uribe *et al.,* 2009) (Markl *et al.,* 2011). The quantitative assessment of 4D Flow data has allowed obtaining novel hemodynamics markers (Zajac *et al.,* 2015) (Sotelo *et al.,* 2016) (Sotelo *et al.,* 2018). The flow information can be evaluated qualitatively and quantitatively for obtaining several hemodynamic parameters providing additional information about the heart's function globally and regionally (Dyverfeldt *et al.,* 2008) (Lorenz *et al.,* 2014) (Van Ooij *et al.,* 2015). The evaluation of the intracardiac flow has proven to be useful for evaluating certain cardiovascular pathologies, such as some cardiomyopathies, vascular diseases, congenital heart disease, and others (Dragulescu *et al.,* 2013) (Föll *et al.,* 2013) (Cibis *et al.,* 2015) (Sotelo *et al.,* 2016) (Sotelo *et al.,* 2017) (Sotelo *et al.,* 2018). For example, figure 1-1 shows the left intraventricular hemodynamics in the left ventricle from 4D Flow MRI using a finite element method applied in a cohort of dilated cardiomyopathy patients. Consequently, this

technique provides a unique approach for a comprehensive hemodynamic analysis to identify biomarkers and their relationships with cardiovascular disease. It is thought that these novel biomarkers may play an important role in the diagnosis and follow-up of abnormalities in the cardiovascular system.

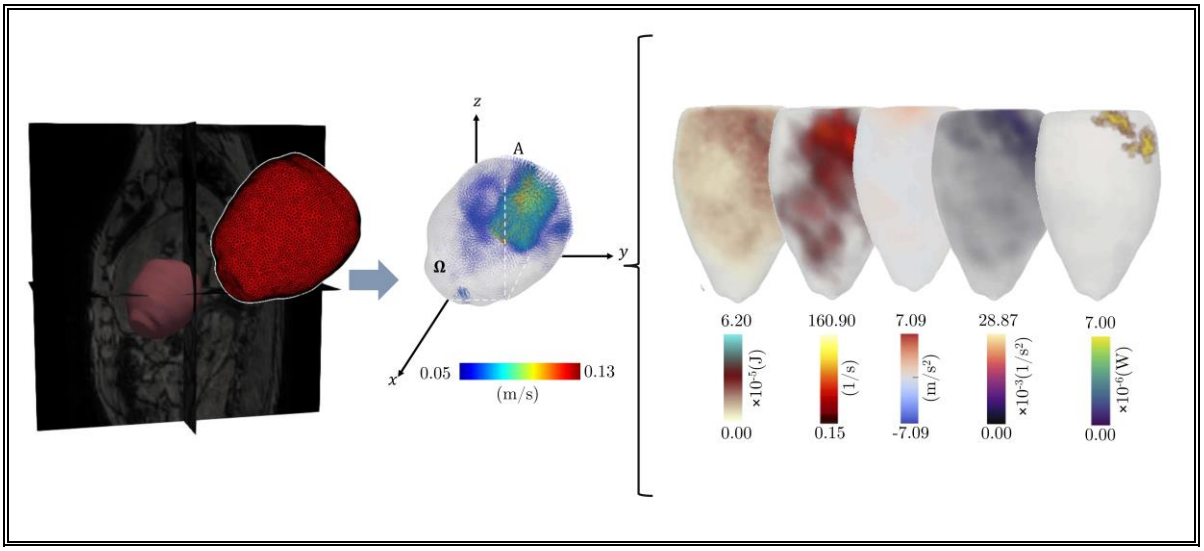

Figure 1-1. Left intraventricular hemodynamics in the left ventricle from 4D Flow MRI using a finite element method. Binary mask, mesh, and 3D maps of velocity, kinetic energy, vorticity, helicity density, viscous dissipation, and energy loss from left to right.

Therefore, this thesis aims to obtain accurate and non-invasively hemodynamic parameters in the heart and great vessels from velocity MRI. First, regarding Phase-contrast (PC-MRI) reconstruction techniques, we implemented and compared the uni-directional Dual Velocity-Encoding (VENC) PC-MRI methods for different added noise levels and a correction algorithm for the Optimal Dual-VENC (Carrillo *et al.*, 2018), which is based on theoretical considerations. Second, regarding image processing and data quantification, we developed a semi-automatic approach for quantifying intracardiac hemodynamic based on velocity data using the finite element method applied in a small cohort of dilated cardiopathy patients. Finally, regarding pattern recognition and machine learning, we analyzed and extracted

multiple correlation patterns of hemodynamic parameters from velocity data and found which parameters allow an accurate classification between healthy volunteers and bicuspid aortic patients with dilated and non-dilated ascending aorta using machine learning.

In this thesis, the proposed methods were tested on different volunteers for developing the different technologies. Nevertheless, the proposed approaches could be applied to the same cohort of patients. This is, acquiring 4D Flow Dual-VENC data and using the ODV corrected method to unwrap the velocity data, then calculating hemodynamic parameters over the unwrapping Dual-VENC data, and finally applying machine learning over the cohort of patients to identify hemodynamic biomarkers.

1.1. Overview

This thesis is structured as follows: In Section 1.2., the generalities of MRI are explained. Section 1.3. explores cardiovascular magnetic resonance (CMR) imaging, including velocity and functional imaging and the application of machine learning in CMR. In Section 1.4., the main and specific objectives and the hypothesis.

In Chapter 2, the first publication is presented. This research aimed to compare some dual-VENC unwrapping methods for different noise levels. We compare four unwrapping methods, the Standard Dual-VENC (SDV) (Lee *et al.,* 1995), the Optimal Dual-VENC (ODV) (Carrillo *et al.,* 2019), bi-, and tri-conditional (Ma *et al.*, 2020). Also, we developed a correction of the ODV.

In Chapter 3, the second publication is given. In this research, we adapted a method for quantifying 4D Flow in the aorta. We modified a methodology applied in the aorta, to obtain several hemodynamic parameters in the left ventricle from a single segmentation using 4D Flow and cine MRI. To show the applicability of this approach, we performed a proof-of-concept study in which we applied the method in a small cohort of dilated cardiomyopathy patients to find which parameters were different from volunteers. We obtained three-dimensional hemodynamic

parameters, including kinetic energy, vorticity, helicity density, viscous dissipations, and energy loss.

In Chapter 4, the third article is provided. This study aimed to identify hemodynamic biomarkers for BAV patients and their relationships with aortic dilation. For that purpose, we analyzed and extracted multiple correlation patterns of hemodynamic parameters, finding which showed high collinearity between them, which allows us to reduce their size to few variables. And finally, we applied machine learning algorithms to discriminate between healthy volunteers and bicuspid aortic valve patients with and without ascending aorta dilation.

Finally, in Chapters 5 and 6, the current work's perspectives and the conclusions of this research are listed and discussed.

1.2. Generalities of Magnetic Resonance Imaging

Since its introduction in the medical field in the early 1980s, magnetic resonance (MR) has become an increasingly important imaging modality to study the human body, whose core equation is the Faraday-Maxwell Equation. It exploits ensemble phenomena in which the composition of a sample can be probed by sensing its magnetic properties through radio frequency (RF) waves. Here, we describe the various parts of MRI and their respective role in the whole.

A rigorous understanding of MRI begins with the elementary particles that give rise to tissue's magnetic properties. Elementary particles have two independent properties which manifest magnetic moments: orbital angular momentum and intrinsic spin. These two properties are independent only to the first order. Their very interaction via spin-orbit coupling led to detectable energy differences in the hydrogen spectrum and, consequently, the discovery of intrinsic spin. The hydrogen atom (^{1}H) is the most frequently targeted nucleus in MRI due to its biological abundance and high gyromagnetic ratio. The ^{1}H nucleus consists of a single proton. Protons are made of quarks, specifically one down and two up quarks, each of them are of spin 1/2. The change and spin of the proton are both directly due to its quark composition. The down quark has a charge of -1/3 while the up quarks each have a

charge +2/3, which all sum up to +1. The nuclear spin is 1/2 by spin cancellation from the antiparallel alignment of two of the three quarks.

1.2.1. Magnetism

Subatomic particles, i.e., electrons, protons and neutrons, are magnets. They derive their magnetism from intrinsic spin and orbital angular momentum. In the absence of an external magnetic field, each particle's spin is oriented in an essentially arbitrary direction, as shown in Figure 1-2.a However, in the presence of an external magnetic field, a bulk magnetism of sample tissue occurs via spin alignment, as illustrated in Figure 1-2.b. The dipole moment, μ, of a single unpaired e.g., proton is given by,

$$\boldsymbol{\mu} = \gamma \boldsymbol{S} \tag{1.1}$$

where γ is the gyromagnetic ratio measured in Hz/T, $\gamma_{1H}/2\pi$ = 42.58 MHz T^{-1}, and **S** is the spin observable. The spin observable has the following two defining properties,

$$\begin{aligned} \mathbf{S}^2|\mathrm{s},\mathrm{m}\rangle &= \hbar^2 \mathrm{s}(\mathrm{s}+1)|\mathrm{s},\mathrm{m}\rangle \\ \mathbf{S_z}|\mathrm{s},\mathrm{m}\rangle &= \hbar^2 \mathrm{m}|\mathrm{s},\mathrm{m}\rangle \end{aligned} \tag{1.2}$$

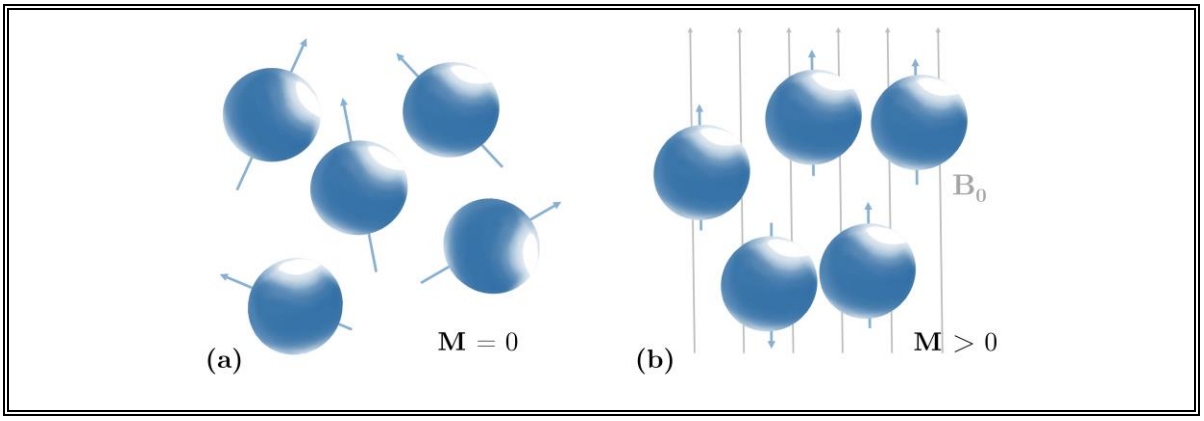

Figure 1-2. (a) Randomized spin orientations. Nuclear spin orientations are random in the absence of an external magnetic field. (b) Nuclear spins align parallel or antiparallel to an applied external magnetic field.

where $|s, m\rangle$ is spin eigenstate vector for a particle of spin s and magnetic spin quantum number m, $\mathbf{S}^2$ is the square of the spin, $\mathbf{S}_z$ is the z-component of spin, and ħ is the Planck's constant (6.626×10^{-34} Js). For the proton s = 1/2 and m ∈ {-1/2, 1/2}.

1.2.2. The Magnetic Potential Energy

The magnetic potential energy is,

$$U = -\boldsymbol{\mu} \cdot \boldsymbol{B} \tag{1.3}$$

The force on a magnetic moment, the torque on a magnetic moment, and the Larmor precession frequency, can be described in terms of the magnetic potential energy *U*.

The magnetic moment aligns itself in parallel or antiparallel orientation to the external field $\mathbf{B}_0$. This process is called magnetization. In the case of a population sample, upon application $\mathbf{B}_0$, the spin orientations go from a somewhat arbitrary array of directions to being composed of only two directions, parallel and antiparallel. The parallel orientation is the lower energy state and is the more populous state for protons in the sample. The population distribution is temperature

dependent, such that the proportion of protons in the higher energy state increases with temperature. This is given by,

$$\frac{N_h}{N_l} = e^{-E/kT} \tag{1.4}$$

where N_h is the higher energy state, N_l is the lower energy state, E is the energy difference between the two states, k is the Boltzmann constant (1.38×10^{-23} J K^{-1}), and T is the absolute temperature in Kelvin. Since $\gamma\hbar\mathbf{B}_0 << kT$ at body temperature and clinical field strengths, we can write the follows,

$$\frac{N_h}{N_l} = 1 + \frac{\gamma\hbar B_0}{kT}$$
$$\Rightarrow N_h - N_l = N_{total}\frac{\gamma\hbar B_0}{2kT} \tag{1.5}$$

This difference creates the net magnetization $\mathbf{M}_0$. If we replace N_{total} with proton density ρ we will get $\mathbf{M}_0$ per unit volume. We also know that the magnetic moment of the proton has a magnitude of $1/2\ \hbar$, thus we can calculate,

$$M_0 = \frac{\rho\gamma^2\hbar^2 B_0}{4kT} \tag{1.6}$$

Since the water contains 6.67×10^{22} protons ml^{-1}, we can show that at body temperature and 1.5 T we get $M_0 = 0.02$ μT ml^{-1}. Assuming that the human head has a volume of approximately 1500 ml and is about 80% water, $\mathbf{M}_0 = 20\ \mu T$, which is small, but measurable.

1.2.3. Precession

When an external magnetic field, $\mathbf{B}_0$, is applied to a proton particle, the particle's magnetic moment precesses about the direction of $\mathbf{B}_0$ at a frequency called the Larmor frequency given by,

$$\omega = \gamma \boldsymbol{B}_0 \tag{1.7}$$

In the equilibrium magnetization state with $\mathbf{B_o} = \hat{z}B_o$ and $M_{xy} = 0$, there is no precession of the bulk magnetization M between $\mathbf{M} \times \mathbf{B}_0 = 0$. Figure 1-3 shows the magnetization of the individual spins, their precession about the applied field direction, and the net magnetization vector.

Considering only the spin of a spin 1/2 proton in a magnetic field and De Broglie's wave equation, which tells us that the frequency is associated with the energy, we get the Hamiltonian,

$$H = -\boldsymbol{\mu} \cdot \boldsymbol{B} = \boldsymbol{\omega} \cdot \boldsymbol{S} = \omega S_z \tag{1.8}$$

Equation 1.10 leads us that the Hamiltonian is proportional to the *z*-component of spin. Therefore, the magnetic spin eigenstates are simultaneously energy eigenstates. Also, the energy eigenvalues are proportional to the magnetic spin quantum numbers. Specially,

$$E_{\pm} = \pm \frac{1}{2} \hbar \omega \tag{1.9}$$

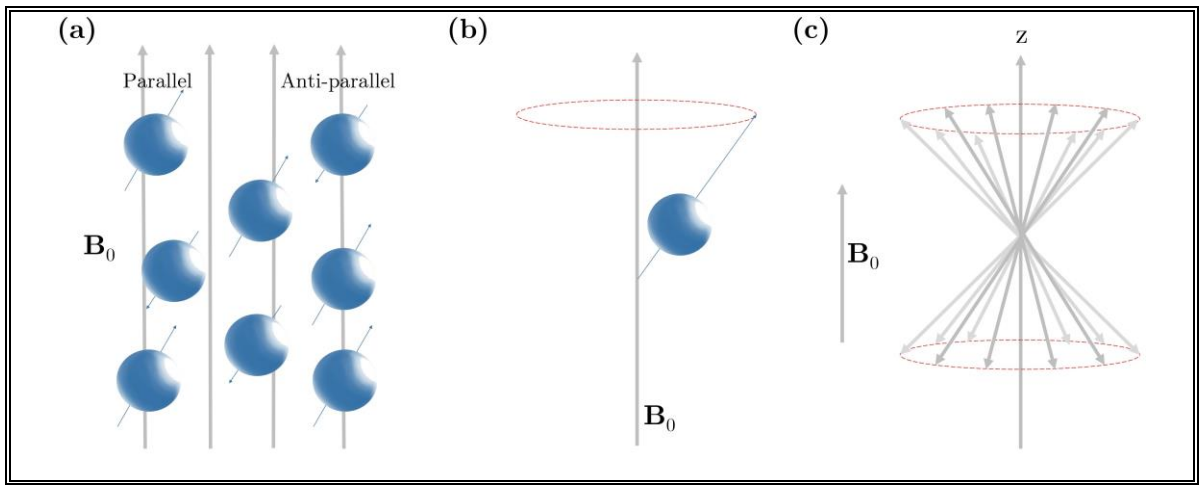

Figure 1-3. (a) Two possible orientations for the protons in an external magnetic field. (b) Precession of the magnetic moment. (c) Average of many protons produces the net magnetization.

1.2.4. Pulse Magnetization

The magnetization in the body is very small (e.g., 1 μT) compared to the main magnetic field (e.g., 1.5 T). It is virtually impossible to measure it at equilibrium, lying parallel with $\mathbf{B}_0$. Nevertheless, applying a 90° radiofrequency (RF) pulse of a weaker magnetic field, $\mathbf{B}_1$, will transition the individual protons from dephased to in-phase oscillation. This manifests as the acquisition of a transverse phase M_{xy} and oscillations of **M** about the *z*-axis at the Larmor frequency ω. This tilting of the magnetization vector also implies a decrease in M_z. Both effects are shown in Figure 1-4. The net external magnetic field is the sum of $\mathbf{B}_0$ and $\mathbf{B}_1$ during the pulse. If the pulse duration was extended indefinitely, the result would be an alignment of the bulk magnetization with a new direction, $\mathbf{B}_0 + \mathbf{B}_1$, and no resultant oscillation would be observed.

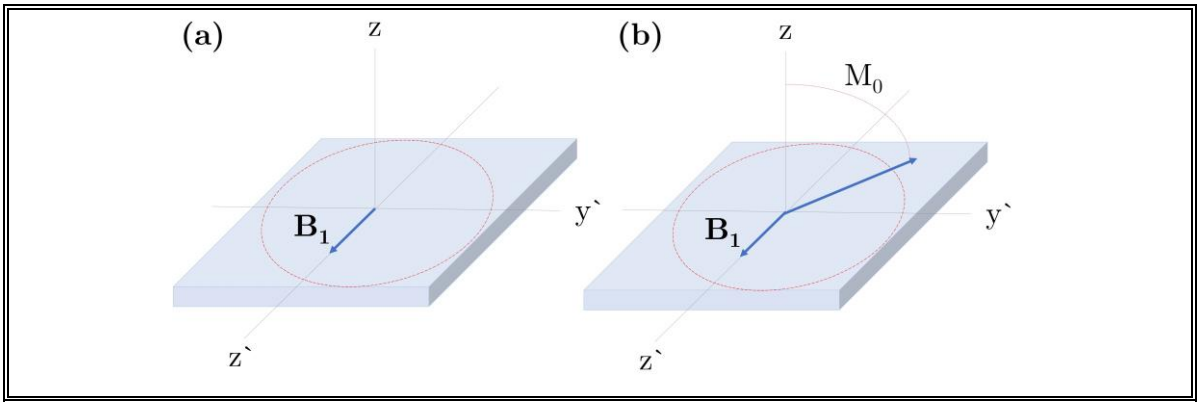

Figure 1-4. (a) The RF pulse produces a fixed magnetic field $\mathbf{B}_1$ in the rotating frame. (b) **M** processes about $\mathbf{B}_1$ until the RF is switched off.

Having rotated **M** into the transverse plane, we measure it by detecting the voltage it induces in a receive coil which is sensitive only to magnetization perpendicular to $\mathbf{B}_0$. **M** is now precessing in the transverse plane, so the coil sees an oscillating magnetic field which induces a voltage varying at the Larmor frequency. The amplitude of the signal decays exponentially to zero in only a few milliseconds, because the protons rapidly dephase with respect to each other. This signal is known as Free Induction Decay (FID).

1.2.5. Relaxation Times

Having excited the protons to flip them into the transverse plane, they begin to relax back to their equilibrium position as soon as the RF pulse is switched off. There are two main features of the relaxation: a dephasing of the spins following their phase coherence after the pulse and realignment along the *z*-axis as they lose the energy they absorbed from the pulse.

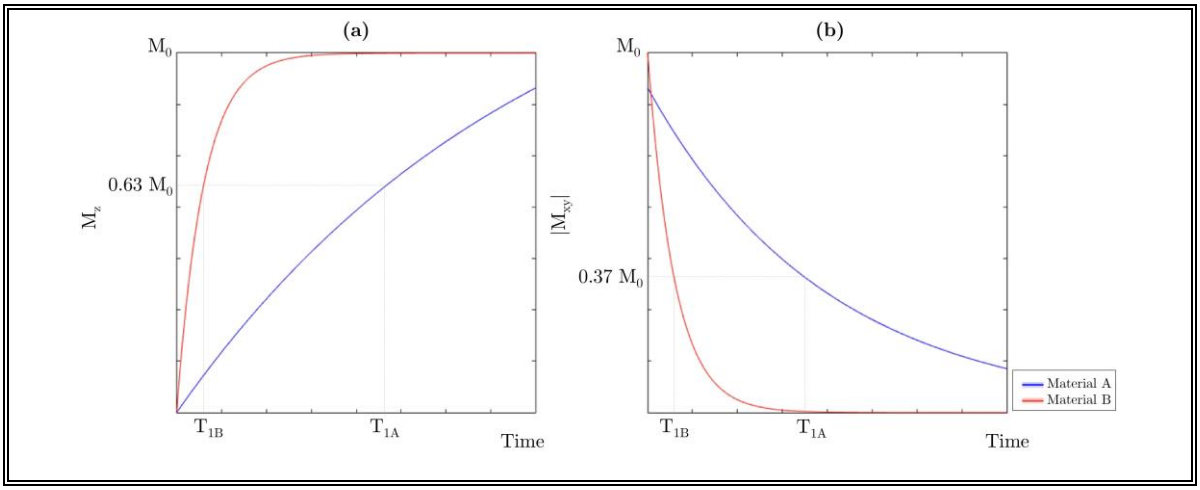

Figure 1-5. (a) Longitudinal and (b) Transverse magnetization of two materials, A and B. In both relaxation times, the material B is quicker than A.

1.2.5.1. Spin-Lattice Relaxation

Then spin-lattice relaxation, also known as T_1 relaxation or longitudinal relaxation is the process of longitudinal magnetization recovery following a $\mathbf{B}_1$ perturbation. Specifically, T_1 is the time that takes to recover 63% of the longitudinal magnetization, and is given by,

$$\boldsymbol{M}_z(t) = \boldsymbol{M}_0\left(1 - e^{-t/T_1}\right) + \boldsymbol{M}_z(0)e^{-t/T_1} \tag{1.10}$$

where $\mathbf{M}_0$ is equilibrium magnetization, and $\mathbf{M}_z(0)$ is the longitudinal magnetization instantaneously after the excitation pulse. Figure 1-5a shows the T_1 recovery process of two materials with different T_1 values. Material B is quicker than A, which means that material B had a lower T_1 value than material A.

1.2.5.2. Spin-Spin Relaxation

The spin-spin relaxation, also known as T_2 relaxation or transverse relaxation, is the process of transverse magnetization relaxation following a $\mathbf{B}_1$ perturbation.

Specifically, T_2 is the time that takes the magnetization to decay 37% of its original value, and is given by,

$$\boldsymbol{M}_{xy}(t) = \boldsymbol{M}_{xy}(0)e^{-t/T_2} \tag{1.11}$$

where $\mathbf{M}_{xy}(0)$ is the transverse magnetization instantaneously after the excitation pulse, following the $\mathbf{B}_1$ induction of in-phase precession, the proton spins again begin to dephase according to T_2 time. Figure 1-5b illustrates the T_2 relaxation process of two materials: A and B. Material B had a lower T_2 value than material A. Of note, the relaxation of transverse magnetization is faster than the recovery of longitudinal magnetization, i.e., $T_2 < T_1$.

1.2.6. Gradients

In MRI, the term gradient refers to an additionally spatially linear variation in the static field strength in the z-direction, i.e., along with $\mathbf{B}_0$. For instance, an x-gradient ($\mathbf{G}_x$) will add to or subtract from the magnitude of the static field at different points along the x-direction. Gradients can be applied in any direction or orientation, and their field strength is measured in mili-tesla per meter (mT m^{-1}). Three sets of gradient coils, $\mathbf{G}_x$, $\mathbf{G}_y$, and $\mathbf{G}_z$, are included in the MR system. They are normally applied only for a short time as pulses. It is these three sets of gradients that give MR its three-dimensional capability. Mathematically the three-orthogonal spatial gradients of $\mathbf{B}_z$ are defined as,

$$\boldsymbol{G}_x = \frac{\partial \boldsymbol{B}_z}{\partial x}, \quad \boldsymbol{G}_y = \frac{\partial \boldsymbol{B}_z}{\partial y}, \quad \boldsymbol{G}_z = \frac{\partial \boldsymbol{B}_z}{\partial z} \tag{1.12}$$

When a gradient is applied, the total field in the *z*-direction experienced by nuclei will be dependent upon the position in space, by

$$\boldsymbol{B}_z(x,y,z) = \boldsymbol{B}_0 + \boldsymbol{xG}_x + \boldsymbol{yG}_y + \boldsymbol{zG}_z \tag{1.13}$$

When a gradient is applied the Larmor frequency will depend upon the total *z*-component of the magnetic field and thus becomes spatially dependent,

$$\omega(\boldsymbol{r},t) = \frac{\gamma}{2\pi}\left(\boldsymbol{B}_0 + \boldsymbol{x}\cdot\boldsymbol{G}_x + \boldsymbol{y}\cdot\boldsymbol{G}_y + \boldsymbol{z}\cdot\boldsymbol{G}_z\right) \tag{1.14}$$

1.2.7. Selective Excitation

In selective excitation, we apply a specially designed RF excitation pulse simultaneously as a gradient. The designer RF pulse contains a narrow range of frequencies of RF, centered about the Larmor frequency. Mathematically, it is expressive as,

$$\Delta\omega(z) = \frac{\gamma}{2\pi}(\boldsymbol{B}_0 + \boldsymbol{zG}_z) \tag{1.15}$$

The principle of slice selection is shown in Figure 1-6. The presence of the gradient causes the resonant frequency to vary with position in the gradient direction. At the isocenter where the additional value of the gradient is zero, the normal Larmor frequency will apply. Further away along the selection axis, either a higher or lower RF frequency will be needed. Resonance will happen if the required frequency is present within the RF pulse's bandwidth, i.e., protons will be excited. Nothing will happen if the frequency necessary is not present within the RF pulse's bandwidth. Thus, excitation for signal production can only take place at or close to the isocenter. If the slice-select gradient is applied along the *z*-axis, the resultant slab of excited nuclei or slice will form a transverse plane.

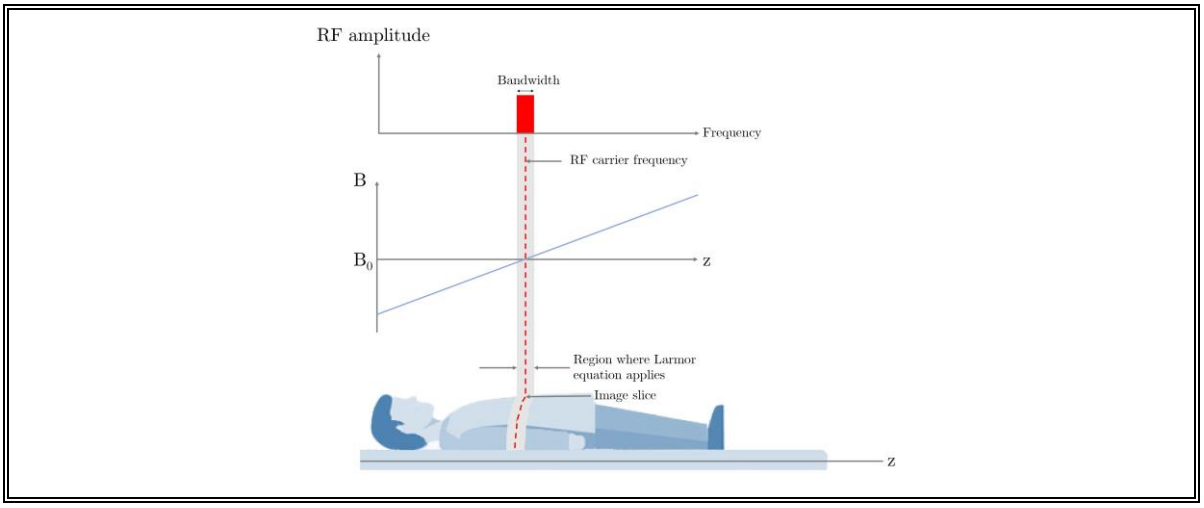

Figure 1-6. Selective excitation of an image slice by applying a shaped RF pulse and a field gradient simultaneously.

1.2.8. In-Plane Localization

In MRI, we use the gradients to measure the two- (or three-) dimensional spectrum of the object being imaged. This spectrum is k-space consists of an array or matrix of individual spatial frequencies. Following the excitation of a localized slice, the next sections will explain the phase and frequency encoding gradients to manipulate the MR signal to encode spatial frequencies.

1.2.8.1. Phase Encoding

Consider the following in conjunction with Figure 1-7, which shows the effect of the phase-encoding gradient on the transverse magnetization at three different locations and times. Furthermore, suppose we already have an MR signal with all the spins in the phase. If we apply the phase-encode gradient (G_{PE}) at time A in the *y*-direction, then the precession of the nuclei will speed up or slow down according to their position along the *y*-axis. This causes the spins to dephase or fan out progressively greater for as long as the gradient is applied. When we switch off the gradient at time B, all the nuclei will revert to their original frequency but keep their different phase angles. This is called phase-encode. The relative phase differences

between signals in other locations remain until either another gradient or the MR signal decays due to T_2 relaxation.

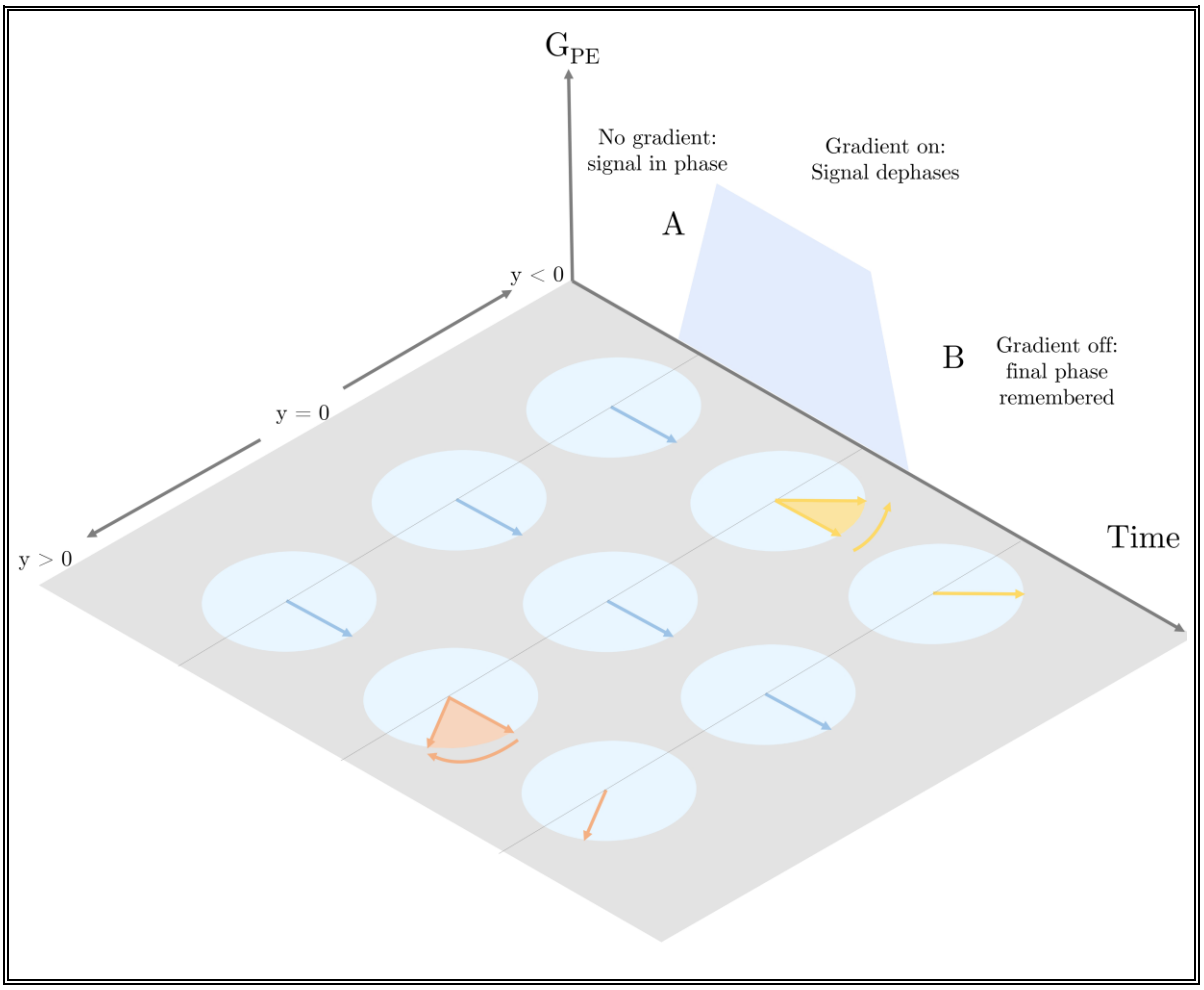

Figure 1-7. Phase encoding returns the signal to the Larmor frequency but with position-dependent phase changes.

The MR experiment consist on the acquisition of several spatial frequencies. Each value of phase-encoding can be considered as a template or a filter that only responds to one spatial distribution of MR signal or spatial frequency. The entire range of possible spatial frequencies must be interrogated to build up a whole picture. When no gradients are applied, we get a signal from the whole object, called zero spatial frequency or zero k.

The MR sequence consists of multiple repetitions of the excitation process followed by a different phase-encode gradient until all possible spatial frequencies are collected. Once all these signals are collected, the application of a Fourier transform converts the spatial frequency distribution into the spatial distribution of the excited nuclei, i.e., an image of the patient.

1.2.8.2. Frequency Encoding

In frequency encoding we can acquire all the spatial frequency information needed from on MR signal following one RF excitation. In phase encoding, we required one MR excitation (RF pulse) for every line of data (i.e., every value of k_{PE}). For a 256-pixel image we thus required 256 MR excitations, and this will take 256 x time-repetitions (TR) ms.

If we apply a gradient continuously and measure or sample the MR signal at different time points during the application of that gradient. The MR signal is affected by a different gradient moment at each point and has an additional amount of phase change. Therefore, each data point reflects a different amount of phase encoding and thus corresponds to a different spatial frequency. Hence, we can collect all the spatial frequencies for that direction from the evolving MR signal in real-time following a single RF excitation. This is analogous to the phase-encode acquisition, which works in pseudo-time, with a sampling separated by TR, as shown in Figure 1-8. The resulting raw data matrix is called *k*-space.

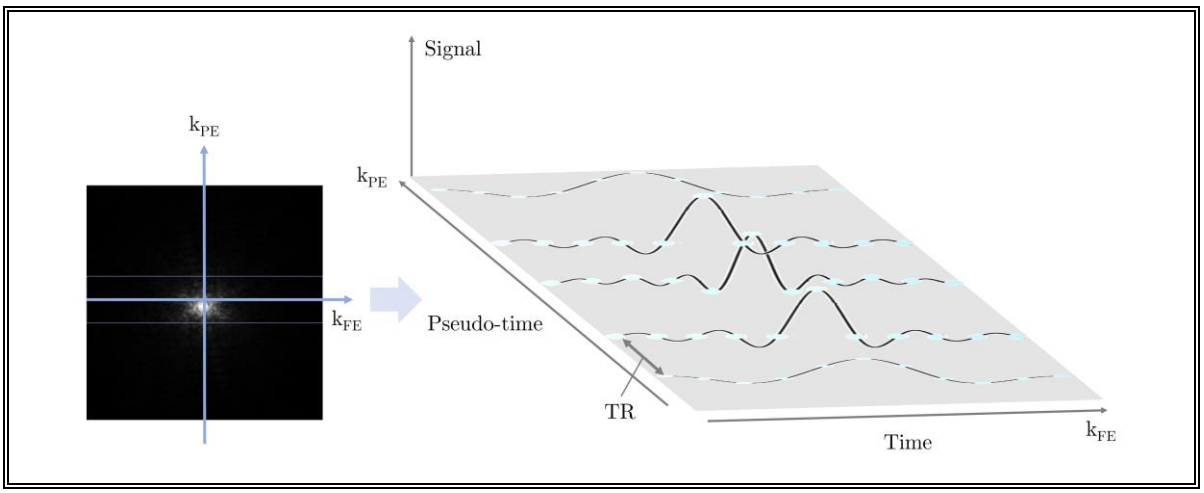

Figure 1-8. Central lines of k-space (magnified) show the equivalence of phase and frequency axes. Signal strength is shown in the vertical direction in the magnified portion. Each phase-encode (PE) line is separated by repetition-time (TR). FE: phase-encode.

1.2.9. Encoding for 2D Fourier Transform Imaging

Following the excitation of a localized slice, frequency- and phase-encoding gradients are applied to manipulate the MR signal to encode spatial frequencies. The effect of frequency-encode gradient G_{FE} applied along the x-direction following the initial excitation on a discrete signal element ∂s is,

$$\partial s(t) = \rho(x)\, e^{-t/T_2^*}\, e^{i\gamma x G_{FE} t} dx \tag{1.16}$$

where $\rho(x)$ is the proton density along the x-direction, and i is the square-root of -1, denoting complex notation. This gradient is applied continuously during the signal acquisition. A dephasing gradient is usually applied prior to sampling to generate a symmetrical echo.

The phase encoding is applied (along the y-direction) through a gradient G_{PE} with a duration of τ prior to the signal measurements. The signal from a small element following the application of both gradients is,

$$\partial s(t) = \rho(x,y)\, e^{-t/T_2^*}\, e^{i\gamma x G_{FE} t}\, e^{i\gamma y G_{PE} \tau} dx dy \tag{1.17}$$

The total MR signal is the integral of this with respect to *x* and *y*. In complete MR acquisition the signal is sampled *M* times at intervals Δ*t*, and the pulse sequence repeated N times, each time incrementing the G_{PE} amplitude such that,

$$G_{PE}(n) = \Delta G n \tag{1.18}$$

For $n = (N/2)$ to $(N/2 - 1)$. Now we define quantities k_{FE} and k_{PE} such that,

$$\begin{aligned} k_{FE} &= \gamma G_{FE} \Delta t\, m \\ k_{PE} &= \gamma \Delta G\, n\, \tau \end{aligned} \tag{1.19}$$

The total signal *S* acquired in two dimensions time *t* and pseudo-time $n\tau$ is found by integrating over *x* and *y*,

$$S(m,n) = \iint \rho(x,y) e^{-t/T_2^*} e^{i2\pi x k_{FE}}\, e^{i2\pi y k_{PE}} dx\, dy \tag{1.20}$$

Which (except for the T^*_2 term) is the form of an inverse Fourier transform (FT) of the spin density $\rho(x,y)$, i.e., $S(m,n) = \rho(k_{FE}, k_{PE})$, allows us to reconstruct the image of the patient's body.

1.3. Cardiovascular Magnetic Resonance Imaging

Cardiac MRI has always been one of the most challenging clinical applications. Imaging in the presence of cardiac and respiratory motion and blood flow requires the development of robust methods to obtain good-quality images. Fortunately, developments in system hardware, pulse sequence, and reconstruction algorithms have improved the reliability of standard imaging methods and introduced new

techniques for myocardial tissue characterization and flow quantification. Given these technical advancements, challenges remain for the user in understanding and optimizing the sequences and methods.

This section will explain

- how to measure the velocity-induced phase shift.
- the velocity imaging without an exogenous contrast agent using the phase-contrast and 4D Flow MRI sequences.
- the meaning and role of velocity-encoding value in the velocity imaging sequences.
- how to assess and quantify the velocity and flow imaging.
- how to measure the functional imaging using the balanced steady-state-free-precession sequence.
- how to quantify and evaluate the functional cardiac analysis.
- a review that summarizes machine learning applications in cardiac magnetic resonance.

1.3.1. Velocity-Induced Phase Shift

Velocity can be measured using velocity encoding gradients, leading to an image whose phase is proportional to the blood flow velocity.

The phase dependency of the MR signal to moving spins can be derived from the precession frequency of spins in local magnetic fields (as shown in the Section 1.2.3). The Larmor frequency, ω, of spins at spatial location **r** in a static magnetic field $\mathbf{B}_0$, local field inhomogeneity Δ $\mathbf{B}_0$, and a magnetic field gradient **G** is given by,

$$\omega(\boldsymbol{r},t) = \gamma B_z(\boldsymbol{r},t) = \gamma B_0 + \gamma \Delta B_o + \gamma \boldsymbol{r}(t)\boldsymbol{G}(t) \tag{1.21}$$

where γ is the gyromagnetic constant, the acquired FID is demodulated concerning the Larmor frequency in the static magnetic field after signal reception.

This corresponds to a transformation of the MR signal into a rotating reference frame such that the main field contribution to the signal frequency can be omitted for further calculations. The integration of equation 1.21 results in the phase of the precessing magnetization and thus the phase of the measured MR signal after an excitation pulse (at t_0) at echo time TE,

$$\phi(\boldsymbol{r},TE) - \phi(\boldsymbol{r},t_o) = \int_{t_0}^{TE} \omega(\boldsymbol{r},t)dt = \gamma \Delta B_0 (TE - t_o) + \gamma \int_{t_0}^{TE} \boldsymbol{G}(t)\boldsymbol{r}(t)dt \tag{1.22}$$

which can be expanded in the following Taylor series,

$$\phi(\boldsymbol{r},TE) = \phi(\boldsymbol{r},t_0) + \gamma \Delta B_0 (TE - t_0) + \sum_{n=0}^{\infty} \phi_n(\boldsymbol{r}^n,TE) = \phi_0 \sum_{n=0}^{\infty} \gamma \frac{\boldsymbol{r}(n)}{n!} \int_{t_0}^{TE} \boldsymbol{G}(t)(t-t_0)^n dt \tag{1.23}$$

where $r^{(n)}$ being the n^{th} derivative of the time dependent spin position and ϕ_n the corresponding n^{th} order phase. The initial signal phase and field inhomogeneities result in an additional background phase ϕ_0. Suppose the motion of the tissue under investigation does not change fast concerning the temporal resolution of data acquisition. In that case, the corresponding velocities can be approximated to be constant during data acquisition. Thus $\boldsymbol{r}(t)$ can be introduced as first order displacement $\boldsymbol{r}(t) = \boldsymbol{r}_0 + \boldsymbol{v}$ (t- r_0), equation 1.23 can be simplified to,

$$\phi(\boldsymbol{r},TE) = \phi_0 + \gamma \boldsymbol{r}_0 \int_0^{TE} \boldsymbol{G}(t)dt + \gamma \boldsymbol{v} \int_0^{TE} \boldsymbol{G}(t)tdt = \phi_0 + \gamma \boldsymbol{r}_0 M_0 + \gamma \boldsymbol{v} M_1 \tag{1.24}$$

The second and third terms are the phase accumulations from the stationary and moving spins under the magnetic gradient **G**. The integral terms describing the influence of the magnetic gradient on the static and moving spins are named the zeroth and the first gradient moments, M_0 and M_1, respectively.

Velocity encoding is usually performed using bipolar gradients, as shown in Figure 1-9. Equation 1.24 results in zero M_0, which does not lead to any phase encoding of stationary spins. However, moving spins will experience a linear velocity depending on phase change, which is proportional to the amplitude and timing of the gradient.

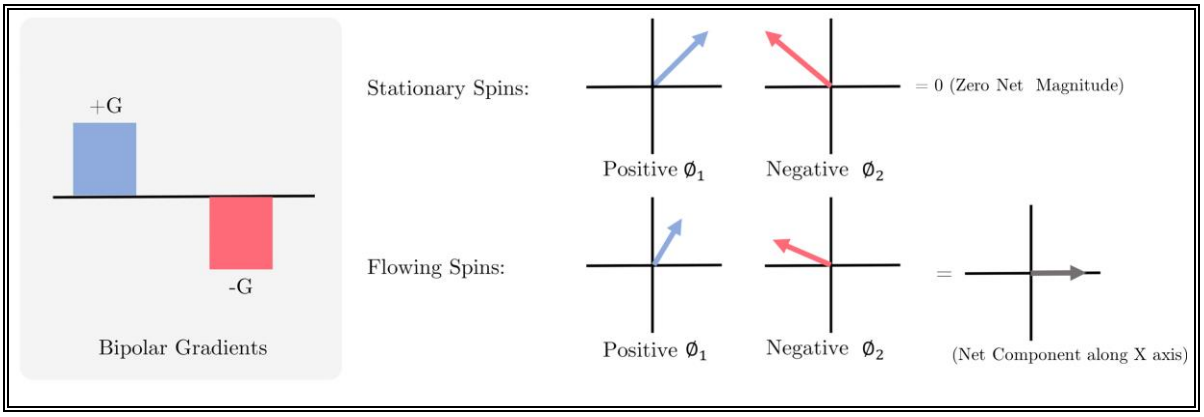

Figure 1-9. A bipolar velocity-encoding gradient. Two lobes have equal areas with opposite polarities. No phase change is observed by stationary spins (i.e., M0 = 0). However, flowing spins will yield a net phase change proportional to their velocity.

By changing the polarity of the bipolar gradients and subtracting the two resulting phase images allows the quantitative assessment of the velocities of the underlying flow or motion. In this way, the desired velocity component can be calculated for every volume element simultaneously, since the difference of the phase is proportional to the velocity as,

$$\Delta\phi(\boldsymbol{r}, TE) = \phi_0 + \gamma \boldsymbol{r}_0 M_0 + \gamma \boldsymbol{v} M_1 - (\phi_0 + \gamma \boldsymbol{r}_0 M_0 - \gamma \boldsymbol{v} M_1) = \gamma \boldsymbol{v} \Delta M_1 \qquad (1.25)$$

where $\Delta M_1 = 2M_1$.

1.3.2. Velocity Imaging without an Exogenous Contrast Agent

Most velocity imaging without contrast is done with the techniques used to create angiograms without using an exogenous contrast agent, e.g., gadolinium, throughout the cardiac cycle. The original velocity imaging without contrast is based on the phase-contrast (PC) sequence that we will explore in the following section.

1.3.2.1. Phase-Contrast Magnetic Resonance Imaging Sequence

Phase-contrast magnetic resonance imaging (PC-MRI) exploits the changes in the phase of blood's transverse magnetization as it moves along a magnetic field gradient. We have already seen how a bipolar gradient gives zero phase shift to stationary spins, but a non-zero phase shift for moving spins. Figure 1-10 shows the PC-MRI sequence in the *x*-direction.

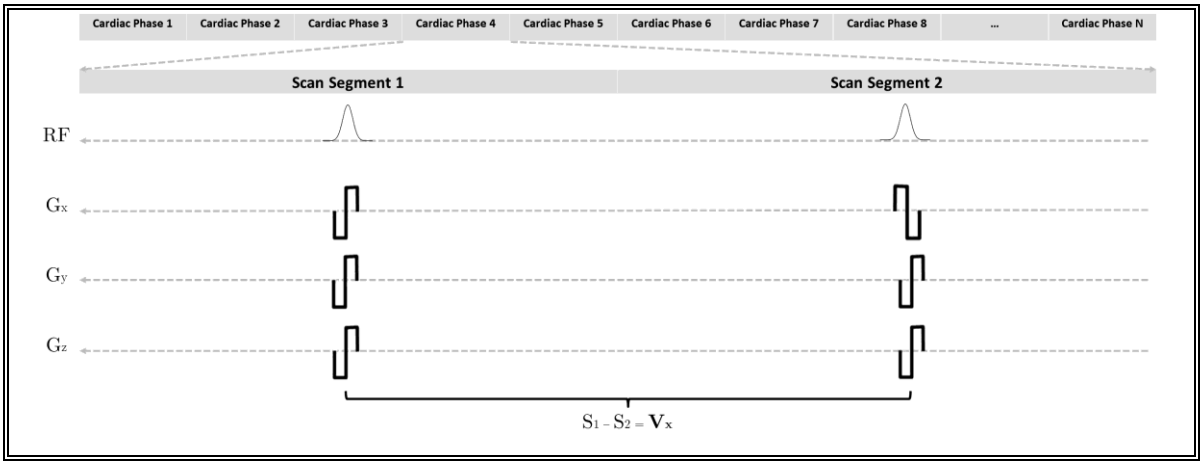

Figure 1-10. Phase-Contrast MRI sequence that allows acquiring images in the, e.g., *x*-direction.

1.3.2.2. 4D Flow Magnetic Resonance Imaging Sequence

The PC-MRI sequence can be extended to construct the velocity vector along each of the three gradient directions to create a linear relationship between the velocity of the blood and the phase of the MR signal. This sequence is called 4D Flow MRI. Figure 1-11 shows the schematic illustration of the sequence.

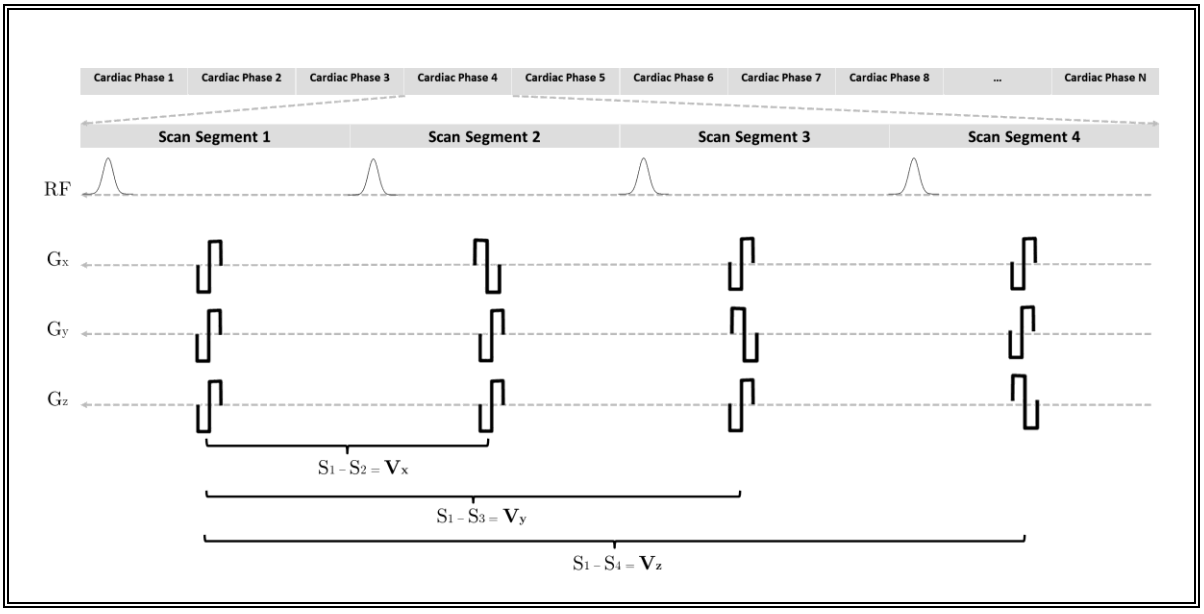

Figure 1-11. 4D Flow MRI sequence that allows acquiring images along each of the three directions.

The individual phase images can be combined to produce a single 3D angiogram by calculating the result flow magnitude image $|v|$ from the x, y, and z, i.e., slice-select, phase encoding and frequency-encoding directions for each pixel using,

$$|v| = \sqrt{v_x^2 + v_y^2 + v_z^2} \tag{1.26}$$

The resultant magnitude image has no directional information and is often a called ‘speed’ image. Also, since each velocity value is squared in the calculation, all the positive and negative velocity information is eliminated, and so any

directional information is lost. However, the greyscale is still proportional to the speed.

In 4D Flow MRI, you excite a slab of tissue, with each slice encoding having velocity sensitization, applied along each of the required directions, all three. This makes 4D Flow MRI studies quite time-consuming. You may have to sacrifice some resolution in the phase-encoding direction or employ parallel imaging techniques to achieve an acceptable acquisition time.

1.3.2.3. Velocity-Encoding in PC- and 4D Flow MRI

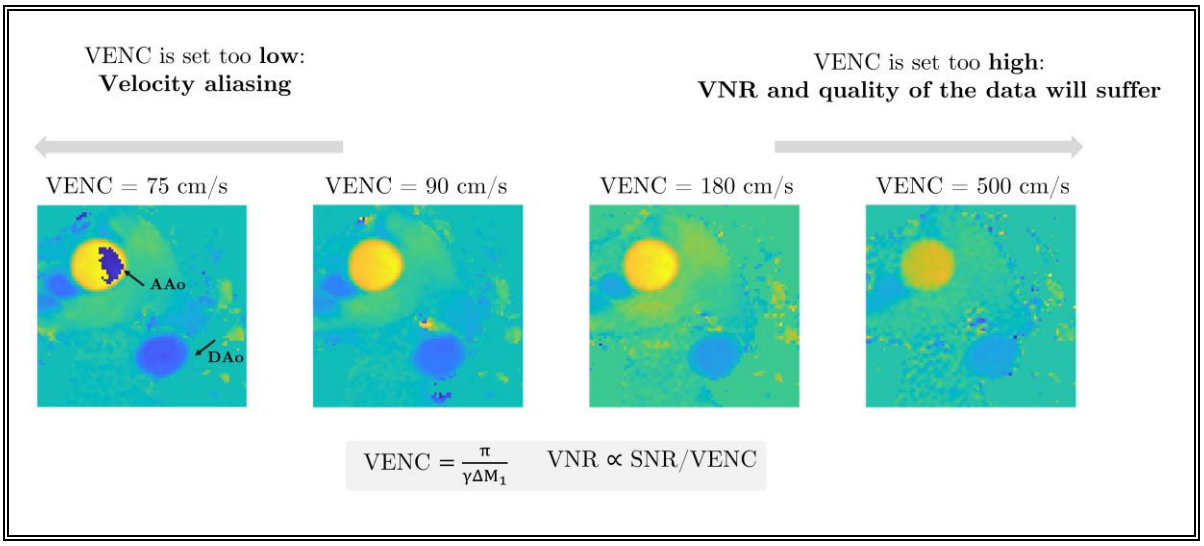

Figure 1-12. PC-MRI with different VENCs (i-iv). The inlay in each image shows the ascending aorta. Black arrows point to locations of uncorrected velocity aliasing. Incrementing the value of VENC worsens the Velocity-to-Noise-Ratio (VNR) because sensitivity has decreased for changes in the velocity.

The relationship between the blood velocity and the MR signal phase is scaled by setting a user-controlled velocity encoding (VENC) value. Since we have 360° of unique phase available, flow in one direction, relative to the gradient, is allocated 0° to + 180°, while flow in the opposite direction is allocated 0° to -180°. The VENC

is the maximum velocity, VENC = $\pi/\gamma\Delta M_1$, is defined as the (positive or negative) maximum velocity that can be detected within π.

With PC- and 4D Flow MRI, you must set a VENC. If you know the velocities in the vessels in interest, you should set your VENC about half the peak velocity. It is possible to use a PC-MRI method whereby you prescribe just a single slice that is thick enough to cover the vessels of interest. This produces a projection angiogram of the blood flow within that thick slice. Since the method is quick, i.e., only a single slice, you can acquire images with different VENCs to find the most suitable value for your time-consuming 4D Flow MRI acquisition.

It is essential to note that VENC is inversely proportional to the Velocity-to-Noise-Ratio (VNR) in the final measured velocity map. Therefore, setting up the VENC is important to obtain velocity data with high VNR but without wrapping artifacts. If the images have wrapping artifact or low VNR, several images need to be acquired with different VENCs, as shown in Figure 1-12. This issue increases the total scanning time.

1.3.2.4. Quantitative Velocity and Flow Imaging

Quantitative blood flow imaging is a powerful technique for assessing cardiac pathologies such as dilated cardiomyopathy and quantifying stenotic valves. The last section explained how it is possible to encode the velocity of moving spins using PC-MRI or 4D Flow MRI sequences. In quantitative velocity/flow imaging, we usually perform a single-slice PC acquisition perpendicular to the vessel's direction or valve in which we wish to quantify the velocity. The velocity-encoding gradients are usually applied along the slice-selection direction to quantify velocities through the slice.

Figure 1-13 shows a typical PC-MRI through the ascending aorta (AAo). Suppose the instantaneous flow is plotted against time for all the cardiac cycle. Then, the area under the curve represents the blood blow in one heartbeat. Multiplying this value by the heart rate gives the volume of blood ejected by minute, known as cardiac output.

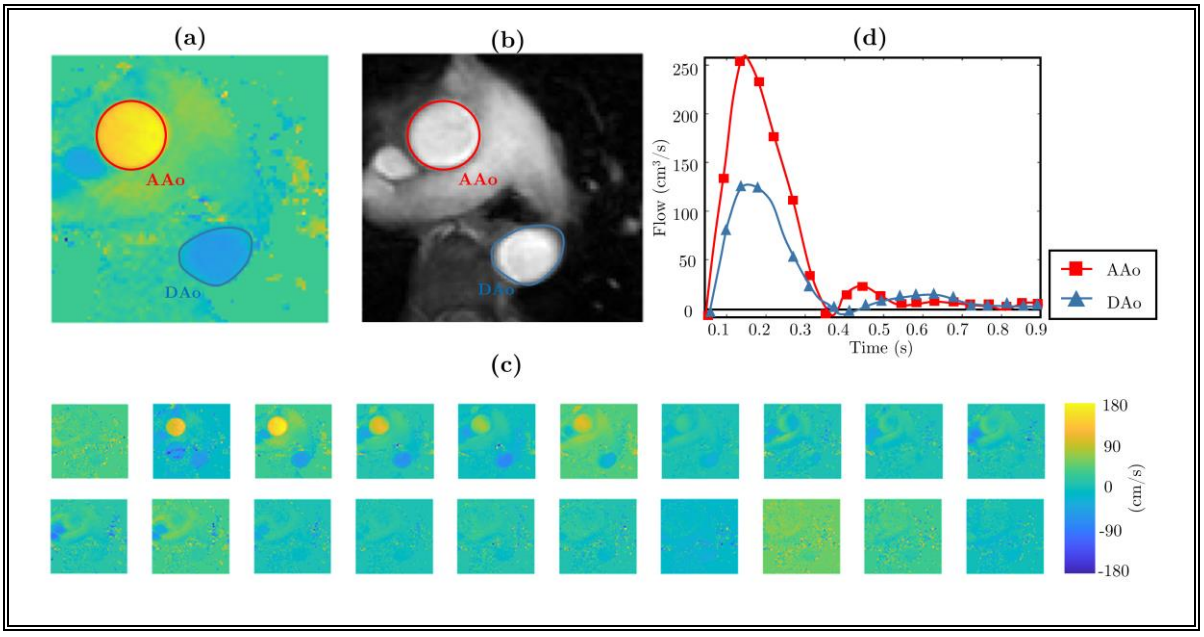

Figure 1-13. PC-MRI through the ascending aorta (AAo) and descending aorta (DAo). (a) Phase-contrast image and (b) Magnitude image from at peak-systole. (c) Phase-contrast images in the cardiac cycle. (d) The Flow vs. the time curve. The flow at each temporal phase is obtained by multiplying the average velocity in each region-of-interest (ROI) (cm/s) by the area of the ROI (cm^2) to give a flow in cm^3/s.

On the other hand, in section 1.3.2.3, we defined the velocity-encoding (VENC) parameter that sets the velocity for which a 180° phase shift occurs. If the actual velocity exceeds the VENC then aliasing will occur.

In several cases, it is important to obtain quantitative information of low and high blood flow velocities simultaneously, which can differ by order of magnitude, even in normal subjects. This can be observed in Figure 1-14 where velocity aliasing occurs in the AAo when velocity exceeds the VENC. To solve this issue, unwrapping methods approaches have been proposed to obtain low and high velocities simultaneously and, by consequence, obtain a unique image without aliasing (Lee *et al.*, 1995) (Lan *et al.*, 2008) (Johnson *et al.*, 2010) (Zwart *et al.*, 2013) (Schnell *et al.*, 2017) (Carrillo *et al.*, 2019) (Ma *et al.*, 2020). Otherwise, it will be necessary to repeat the acquisition using a higher VENC. Nevertheless, velocity images will appear noisier as the VENC is increased.

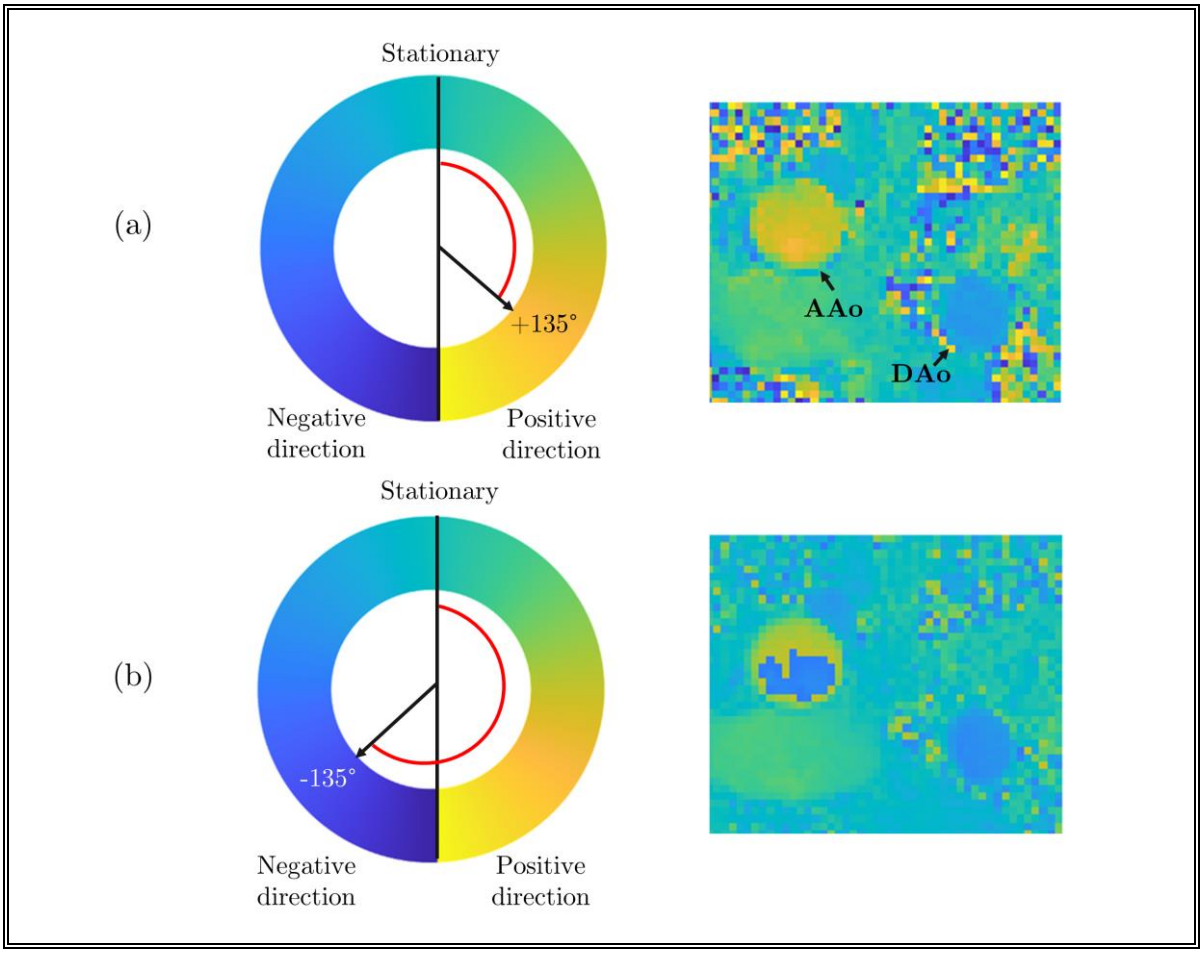

Figure 1-14. PC velocity aliasing. Velocities in one direction are allocated the range 0° to 180° and velocities in the opposite direction 0° to -180°. The parula colormap 0° is represented by teal blue, while +180° is allocated yellow and -180° is allocated blue. The velocities in the ascending aorta (AAo) are shown as teal blue to yellow, while the descending aorta (DAo) are shown as teal blue to blue. (a) VENC is set to 150 cm/s, so a velocity of 112.5 cm/s results in a phase shift of +135°. (b) In this case, a VENC of 75 cm/s a velocity of -56.25 cm/s results in a shift of -135°. Due to the fact, velocity exceeds the VENC; aliasing velocity occurs in the AAo.

Even though the phase images from positive and negative flow encoding are subtracted to eliminate background phase errors, there may be residual errors due to the different eddy currents produced by the different flow-encoding gradient polarities. These errors appear as offsets in the data, so the stationary background is

typically no longer zero. Correction of the data using the background signal offset may be required.

Velocity mapping can also be performed in-plane by applying the flow-encoding gradients on the approximate axis. Furthermore, using 4D Flow MRI, it is possible to acquire velocity data along with all three directions at the cardiac cycle. These data can then be used to calculate temporally resolved 3D hemodynamic, as shown in Figure 1-15. These acquisitions are quite time-consuming and require respiratory gating.

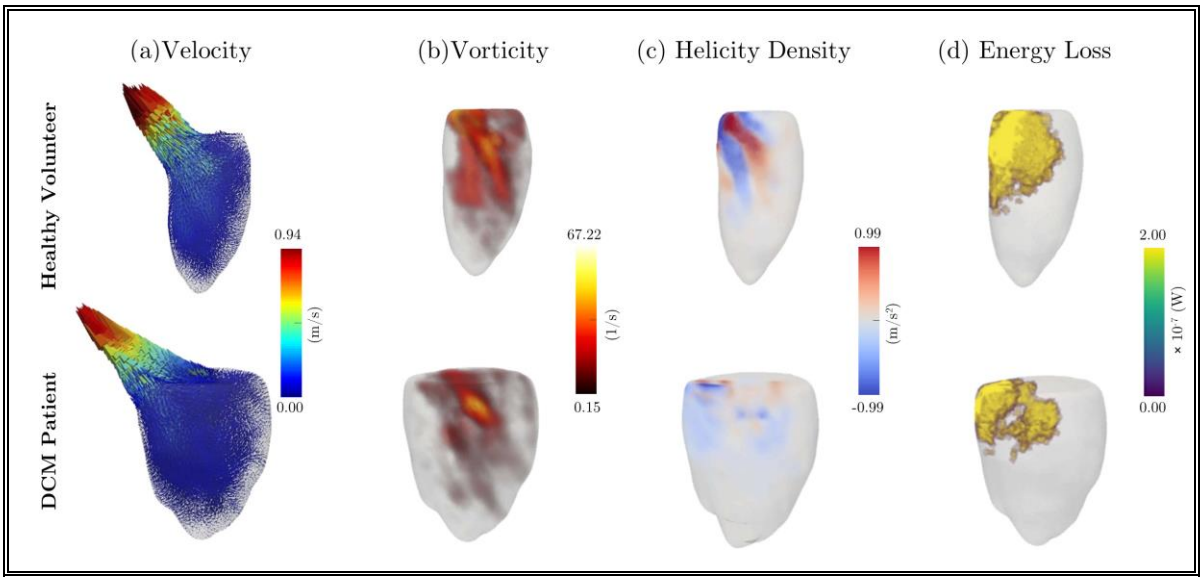

Figure 1-15. 3D maps of (a) velocity, (b) vorticity, (c) helicity density, and (d) energy loss (streamlines) of the left ventricle at peak-systole for a healthy representative volunteer and dilated cardiomyopathy (DCM) representative patient. We adjusted the color bar range for visualization purposes.

1.3.3. Functional Imaging

Functional cardiac imaging is designed to visualize the heart motion throughout the cardiac cycle. We use gradient-echo sequences triggered by the

vectorcardiography (VCG). Gradient-echo sequences have very short repetition times (TR), so data from the same slice location can be acquired at different time points through the cardiac cycle. Each time-point is known as a 'cardiac phase' or 'temporal phase'. Thanks to the flexibility of MR slice selection, it is possible to acquire multiphase 'cine' images in any plane (Bogarert *et al.*, 2000). The following section will explain one MR technique that allows us to obtain functional imaging.

1.3.3.1. Balanced Steady-State-Free-Precession

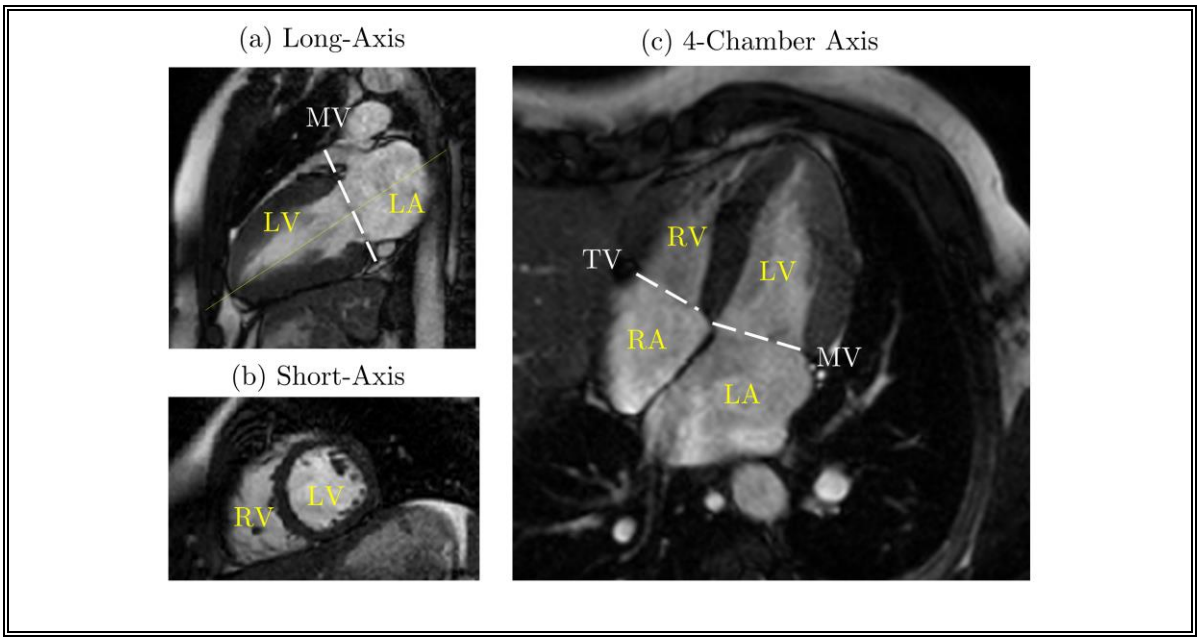

Figure 1-16. b-SSFP images with different cardiac planes starting from (a) long-axis, (b) short-axis, and (c) 4-chamber axis. RV: right ventricle, LV: left ventricle, LA: left atrium, RA: right atrium, MV: mitral valve, and TV: tricuspid valve.

Cine imaging used spoiled gradient-echo sequences. These sequences relied on the in-flow of blood to provide the contrast between the bright blood pool and the darker myocardium. Hence, image quality could be quite variable. Therefore, cardiac MRI was improved with the development of cine balanced steady-state-free-precession (b-SSFP). Since the contrast in b-SSFP depends mainly on the ratio T_2/T_1, the contrast between blood (where the ratio is high) and myocardium (where

it is less) is much better. These images can be used to extract functional information of the heart. Note that cardiac MRI does not typically use standard, axial, sagittal, and coronal views. Most imaging planes are oblique, orientated to the heart chambers the valves, as shown in Figure 1-16.

1.3.3.2. Functional Cardiac Analysis

In the short-axis stack of cine slices covering the entire left ventricle, we can measure the blood pool volume at the end-systolic (smallest ventricular volume) and end-diastolic (largest ventricular volume) phases calculate the percentage of blood ejected in each heartbeat (Bogaert *et al.*, 2000). This is known as the ejection fraction (EF) and is an important measure of cardiac function. Specialized cardiac processing software can be used to either manually or (semi-) automatically define the endocardial border between the blood pool and the myocardium. Summing the left ventricular blood pool volume (blood pool area × slice thickness) across all slices acquired at the end-diastolic phase gives the left ventricle end-diastolic volume (LVEDV). Similarly, summing all the volumes at the end-systolic phase gives the left ventricle end-diastolic volume (LVESV). The left ventricular stroke volume (LVSV), the volume of blood ejected during each heartbeat, is calculated as the differences between LVEDV and LVESV,

$$LVSV = LVEDV - LVESV \tag{1.28}$$

The ejection fraction (EF) as a percentage can be calculated from,

$$EF = \frac{LVSV}{LVEDV}\,100\% \tag{1.29}$$

If we also define the outer contour of the myocardium, called the epicardial border, we can then measure the volume of the myocardium. Multiplying the myocardial volume by the density of tissue (1.06 g ml^{-1}) gives us an estimate of the

myocardial mass. This is another quantitative metric than can be used to monitor patients who have thickened ventricular walls (American Heart Association, 2020).

The last measure is the cardiac output (CO), which corresponds to the volume of blood the heart pumps per minute. Cardiac output is calculated by multiplying the left ventricular stroke volume by the heart rate (HR),

$$CO = LVSV \cdot HR \tag{1.30}$$

The normal range for cardiac output is about 4 to 8 L/min, but it can vary depending on the body's metabolic needs. Cardiac output is important because it predicts oxygen delivery to cells (American Heart Association, 2020).

1.3.4. Machine Learning in Cardiovascular Magnetic Resonance

Artificial intelligence (AI) methods have gained increased attention in cardiology and cardiovascular imaging (Damini *et al.*, 2019). The application of AI may reduce cost and improve value at all image acquisition, interpretation, decision-making stages, and subsequent clinical pathways. For instance, in CMR, AI methods have been applied to segment left and right ventricles and thoracic aorta to automatic cardiovascular volume assessment and enhance reproducibility in clinical assessments (Avendi *et al.*, 2017) (Tan *et al.*, 2018) (Tao *et al.*, 2019) (Campello *et al.*, 2021) (Aviles *et al.*, 2021).

Machine learning, i.e., the technique used to give AI to learn. This technique can learn rules and progressively identify patterns from large datasets without explicitly programmed or prior assumptions. For a compelling performance of the ML algorithm, it must be considered: (1) data that are relevant and detailed enough to answer the question being asked, and (2) a computational ML algorithm appropriate for the type of data available (Ciaburro 2017). Therefore, the quality, accuracy, and richness of features in data will determine how effective computational techniques can deliver an AI. Provision of inappropriate or incorrectly categorized data effectively means that the dataset does not closely resemble the real world enough

for ML to create a representative model, which may result in inappropriate decisions (Mester *et al.,* 2011) (Singh *et al.,* 2019).

The following sections will explain the different types of ML algorithms, selecting the correct algorithm, and the proper construction of an ML model.

1.3.4.1. Types of Machine Learning

We already discussed that ML's power is due to the quality of its algorithms. There are divided into several types depending on the nature of the dataset used for learning or the type of feedback adopted by the system.

1.3.4.1.1. Supervised Machine Learning Algorithms

The algorithm generates a function that links input values to the desired output by observing a set of examples. Each data input has its relative output data, which is used to construct predictive models. Table 1-1 summarizes some examples of these types of algorithms. These algorithms are based on the following concept: similar inputs correspond to similar outputs. Nevertheless, this assumption is not valid in the real world. The proper functioning of such algorithms depends significantly on the input data. If there are only a few training inputs, the algorithm might not have enough experience to correct output. Another issue is that the algorithm will function excessively slow if there is much input. Moreover, this type of algorithm are very sensitive to noise.

In supervised ML, it is possible to split problems based on the nature of the data. If the output value is categorical, such as female/male to a particular class, it is a classification problem. If the output is a continuous real value in a certain range, it is a regression problem.

Table 1-1. Examples of supervised ML algorithms with their description.

Algorithm	Description
Regression Analysis	Uncomplicated form of supervised ML that generates an algorithm to describe a relation between multiple variables and an outcome of

	interest. Stepwise models automatically add or remove variables based on the strength of their association with the outcome variable, until a significant model is developed or learned (Mayr *et al.,* 2014).
Support Vector Machine (SVM)	SVM provides nonlinear models by defining planes in higher dimension that best separate out features into groups that predict certain outcomes (Chykekuk *et al.,* 2011) (Domingos *et al.,* 2014).
Random Forest (RF)	RF identifies the best outpoint values in different features of individual groups of related data to be able to separate them out to predict a particular outcome (Chykekuk *et al.,* 2011) (Domingos *et al.,* 2014).
Neural Networks	Features are fed through a nodal network of decision points, meant to mimic human neural processing (Mery 2015).
Convoluted Neural Networks	A multilayered network, often applied to image processing, simulating some pf the properties of the human visual cortex (Mayr *et al.,* 2014).
Deep Learning (DL)	DL is defined as a class of artificial neural network algorithms, in which more internal layers are used than in traditional neural network approaches (Lee *et al.,* 2017) (Krittanawong *et al.,* 2017).

1.3.4.1.2. Unsupervised Machine Learning Algorithms

The algorithm tries to derive knowledge from a general input without the help of a set of pre-classified examples used to build descriptive models. A typical example of the application of these algorithms is search engines. Table 1-2 summarizes some examples of unsupervised ML algorithms. Unlike supervised algorithms, there is no information on gender classes of the example or generally on the output corresponding to a certain input. The objective is to get a model that can discover interesting properties, i.e., groups with similar or different characteristics (clustering). Hence, given one or more keywords, they are able to create a list of links related to our search.

Table 1-2. Examples of unsupervised ML algorithms with their description.

Algorithm	Description
Principal Component Analysis (PCA)	PCA can identify the most variations in the features (Mery 2015).
Hierarchical clustering	This method grants a dataset into a multilevel cluster tree or dendrogram. The distance (dissimilarity) is defined as one minus Pearson's correlation coefficient. It expressed that if two features have a shorter distance, they are similar, i.e., the distance is 0, the correlation coefficient is 1. The variable that quantifies an effective representation of the pattern dissimilarities in the dendrogram is the cophenetic correlation. (Gu *et al.*, 2010) (Ciaburro 2017).
Partitioning algorithms (e.g., K-means clustering)	The cluster analysis identifies the degree of separation of different features within a dataset and tries to find groupings in which features are most differentiated. It does this by defining similarity based on proximity to the cluster's centroid. The algorithm modulates the data to build the cluster by iteratively evaluating the distance from the centroid (Ciaburro 2017).
Model-based clustering (e.g., Expectation-Maximization Algorithm)	This clustering algorithm makes a general assumption that the data in each cluster is generated from probabilistic model (Ciaburro 2017).

1.3.4.2. Choosing the Right Algorithm

In the previous section, we learned the difference between various types of ML algorithms. Now it is time to find which algorithm is the most suitable for our needs. If we have a classification problem, there are two options available:

- Classify based on input: We have a supervised learning problem, if we can label the input data. In the opposite option, it is unsupervised.
- Classify based on output: If our model output is a number, we must deal with a regression problem. But it is a classification problem if the model's output is a class. Finally, we have a clustering problem if the model's output is a set of input groups.

Having identified the tools, we need to evaluate their performance. We simply apply the selected algorithms on the datasets at our disposal to do this.

Subsequently, based on a series of carefully selected evaluation criteria, we compare the performance of each algorithm (Ciaburro 2017).

1.3.4.3. Construct the Proper Machine Learning Model

Finally, an algorithm has been defined; we will follow a procedure characterized by the following steps:

i. Collect the data: The data is collected in a database to then be analyzed to derive knowledge.
ii. Preparing the data: Once we have the database, we must make sure it is a format usable by the algorithm we want to use. To do this, we may need to do some formatting, e.g., recall that some algorithms need data in an integer format.
iii. Exploring the data: Using plots, we can recognize patterns or whether some data points are vastly different from the rest of the dataset.
iv. Training the algorithm: In this step, the ML begins to work with the definition of the model and the next training. The model starts to extract knowledge from large amounts of data that we had available, and that nothing has been explained so far. There is no training step for unsupervised learning because we do not have a target value.
v. Testing the algorithm: In this step, we use the information learned in the previous step to see if the model works. The evaluation of an algorithm is for seeing how well the model approximates the real system. In the case of supervised learning, we have some known values that we can use to evaluate the algorithm.
vi. Evaluating the algorithm: We can assess the approximation ability of the model by applying it to real data. The model preventively trained and tested is valued in this phase.
vii. Improving algorithm performance: Now that we have verified that the model works, we must evaluate the performance to analyze the whole process.

1.4. Hypothesis and Objectives

1.4.1. Hypothesis

We hypothesize that using more robust acquisition strategies, processing imaging techniques, and machine learning on velocity MR images will lead to more accurate and precise hemodynamic parameters than current methodologies.

1.4.2. Objectives

This research aims to obtain accurate and non-invasively hemodynamic parameters in the heart and great vessels from velocity MR images, improving data acquisition and reconstruction techniques regarding the velocity aliasing correction, image processing, and data quantification applying pattern recognition and machine learning. Therefore, the specific objectives of this investigation are: (1) to compare the uni-directional Dual Velocity-Encoding PC-MRI methods for different added noise levels and to propose a correction algorithm for the Optimal Dual-VENC method (Carrillo *et. al.,* 2018), which is based on theoretical considerations. (2) To develop a semi-automatic approach for quantifying intracardiac hemodynamic based on velocity data using the finite element method applied in a small cohort of dilated cardiomyopathy patients. And (3), to analyze and extract multiple correlation patterns of hemodynamic parameters from velocity data and find which parameters allow an accurate classification between healthy volunteers and bicuspid aorta valve patients with dilated and non-dilated ascending aorta using machine learning.

2. FIRST ARTICLE: COMPARISON OF AND IMPROVED UNI-DIRECTIONAL DUAL VELOCITY-ENCODING MRI

2.1. Introduction

Phase-contrast (PC) MRI enables the quantification of velocities by subtracting two measured phases of the complex transverse magnetization (Markl *et al.,* 2012). This method, extended to 4D Flow, allows several applications for the quantitative analysis of cardiovascular diseases (Wigstrom *et al.,* 1999) (Wu *et al.,* 2004) (Kvitting *et al.,* 2004) (Markl *et al.,* 2007) (Stalder *et al.,* 2008) (Markl *et al.,* 2011). However, the applications of such techniques are limited by the Velocity-to-Noise-Ratio (VNR) of the images. The VNR is mainly managed by setting a velocity-encoding sensitivity (VENC). VENC is inversely proportional to VNR in the final measured velocity map. However, if VENC is lower than the true velocity, it leads to phase wrapping in the velocity map (Stalder *et al.,* 2007). Furthermore, even for VENC values slightly larger than the true velocity, velocity aliasing may occur due to measurement noise (Pelc *et al.,* 1991) (Ha *et al.,* 2016).

Therefore, setting up the VENC is important to obtain velocity data with high VNR without wrapping artifacts. If the images have wrapping artifacts or low VNR, several images may need to be re-acquired with different VENCs. This issue increases the total scanning time (Markl *et al.,* 2012).

In some cases, it is necessary to obtain quantitative information of low and high blood flow velocities simultaneously within the same field of view. For instance, velocities from veins and arteries can differ by orders of magnitude, even in normal subjects. Therefore, the images with high VNR can be obtained based on unwrapping low-VENC images by using the high-VENC reconstruction to correct those areas with velocity aliasing (Ghiglia *et al.,* 2012). In principle, phase unwrapping seems like a simple operation, which detects phase jumps and adds (or subtracts) the appropriate multiple of 2π to discrepant signal values. Nevertheless, the presence of noise, processing errors, undersampling, and spurious artifacts

converts this problem to a cumbersome process. To solve this issue, dual-VENC approaches have been proposed.

Lee et al. made the first implementation of dual-VENC 2D PC-MRI with through-plane velocity encoding that acquired three phases with different velocity encoding gradients, allowing reconstruction of two sets of velocity images corresponding to a high- and low-VENC. The low-VENC image is then unwrapped using the high-VENC (Lee *et al.*, 1995). We call here this method Standard Dual-VENC (SDV). The result is a single dataset with the favorable VNR of the low-VENC scan but without velocity aliasing.

Furthermore, Schnell et al. developed a dual-VENC 4D flow MRI sequence using a shared reference scan followed by two successive interleaved, which allowed the encoding of 3D blood flow velocities within 7-point (Schnell *et al.*, 2017). In this context, a different dual-VENC reconstruction method consisting of the high VENC data to correct for aliasing in the low VENC data based on empirically defined thresholds. Recently, Ma et al. proposed two improved ways to perform the dual-VENC reconstruction based on fixed thresholds using biconditional and triconditional statements (Ma *et al.*, 2020).

Carrillo et al. reformulated the phase-contrast velocity as a least-squares estimator. The method was called Optimal Dual-VENC (ODV) and justified theoretically high/low VENC ratios such that the aliasing velocity can be minimized (Carrillo *et al.*, 2019). The ODV formulation can be generalized to multiple-motion encoding in a straightforward manner, as it was done by Herthum et al. (Herthum *et al.*, 2022), where it was also successfully applied to MR Elastography in the brain.

In this study, we aimed to compare the SDV, ODV, bi-, and tri-conditional unwrapping methods under different noise conditions. In addition, we proposed a correction algorithm for the ODV method to improve the success of the methods, which is based on theoretical considerations.

2.2. Theory

2.2.1. Assumptions

We assume three measurements with gradients $G_0 = 0 < G_H < G_L$, this results in three measured phases φ_0, φ_H, and φ_L. Two motion images with normal distribution can then be estimated that share the background phase, φ_0, from the three-phase measurements:

$$u_H = \frac{\varphi_H - \varphi_o}{\pi} VENC_H, \quad u_H \sim \mathcal{N}\left(\overline{u_H}, 2\sigma_\varphi^2 VENC_H^2\right) \tag{1.1}$$

$$u_L = \frac{\varphi_L - \varphi_o}{\pi} VENC_L, \quad u_L \sim \mathcal{N}\left(\overline{u_L}, 2\sigma_\varphi^2 VENC_L^2\right)$$

u_H and u_l are related to velocities acquired with high- and low-VENCs, where $VENC_L = \beta VENC_H, 0 < \beta < 1$, $\overline{u_H}$ and $\overline{u_L}$ are the mean velocity of the high- and low-VENCs, respectively, the value of σ_φ^2 depends on the SNR of the magnetization measurements, and the variance of u_H and u_L - after successful unwrapping - are respectively, $Var(u_H) = 2\sigma_\varphi^2 VENC_H^2$ and $Var(u_L) = 2\sigma_\varphi^2 VENC_L^2$.

The four unwrapping methods that were investigated in this study are further described below.

2.2.1.1. Standard Dual-VENC Approach

Given two images with different VENC values, dual-VENC reconstructions aim to unwrap a velocity reconstructed with low VENC using images acquired with a high VENC as follows:

$$k = N.I.\left(\frac{u_{high} - u_L}{2VENC_L}\right) \qquad u_{SDV} = u_L + 2VENC_L k \tag{1.2}$$

with N.I. the nearest integer operator and u_{high} computed as,

$$u_{high} = \begin{cases} u_i & iVENC > VENC_H \\ u_H & \text{otherwise} \end{cases} \quad (1.3)$$

where u_i is defined as,

$$u_i = \frac{\varphi_L - \varphi_H}{\pi} iVENC \quad (1.4)$$

with

$$iVENC = \frac{VENC_H \ VENC_L}{VENC_H - VENC_L} \quad (1.5)$$

This method is a slightly modification of the Standard Dual-VENC (SDV) reported in (Lee *et al.*, 1995). In order to make a fair comparison with the other methods, we took full advantage of the VENCs used. In case iVENC > $VENC_H$, we used u_i rather than u_H as the original SDV would have used, maintaining the effective VENC value. Note that $VENC_L < VENC_H \leq$ iVENC.

2.2.1.2. Bi-conditional Approach

Following the logic of Dual-VENC methods proposed by Schnell *et al.* (Schnell *et al.*, 2017), in Ma *et al.* (Ma *et al.*, 2020) the three sets of phase-contrast images (u_i, u_H, u_L) are used to identify wrapped voxels in the lowest VENC image.

First, a biconditional unwrapping method was proposed by an extension of Equation (1.2), where the aliased velocities fell into two categories:

$$\begin{aligned} VENC_L < u_L - u_i < 3VENC_L &: u_{biconditional} = u_L + 2VENC_L \\ -3VENC_L < u_L - u_i < -VENC_L &: u_{biconditional} = u_L - 2VENC_L \\ 3VENC_L < u_L - u_i < 5VENC_L &: u_{biconditional} = u_L + 4VENC_L \\ -5VENC_L < u_L - u_i < -3VENC_L &: u_{biconditional} = u_L - 4VENC_L \end{aligned} \quad (1.6)$$

and

$$\begin{aligned} VENC_H < u_H - u_i < 3VENC_H &: u_{biconditional} = u_L + 2VENC_L \\ -3VENC_H < u_H - u_i < -VENC_H &: u_{biconditional} = u_L - 2VENC_L \\ 3VENC_H < u_H - u_i < 5VENC_H &: u_{biconditional} = u_L + 4VENC_L \\ -5VENC_H < u_H - u_i < -3VENC_H &: u_{biconditional} = u_L - 4VENC_L \end{aligned}$$

2.2.1.3 Tri-conditional Approach

Also, in Ma *et al.* (Ma *et al.*, 2020), following the same strategy refers in the bi-conditional unwrapping method, the tri-conditional reconstruction algorithm also considered the relationship between the low- and high-VENC images, using the same two aliased velocity categories, with a new last condition. It brings the high- and low-VENCs into the same VENC domain and adds an additional constraint to prevent incorrect unwrapping of aliased voxels.

$$\begin{aligned} VENC_L < u_L - u_i < 3VENC_L &: u_{triconditional} = u_L + 2VENC_L \\ -3VENC_L < u_L - u_i < -VENC_L &: u_{triconditional} = u_L - 2VENC_L \\ 3VENC_L < u_L - u_i < 5VENC_L &: u_{triconditional} = u_L + 4VENC_L \\ -5VENC_L < u_L - u_i < -3VENC_L &: u_{triconditional} = u_L - 4VENC_L \end{aligned} \quad (1.7)$$

and

$$\begin{aligned} VENC_H < u_H - u_i < 3VENC_H &: u_{triconditional} = u_L + 2VENC_L \\ -3VENC_H < u_H - u_i < -VENC_H &: u_{triconditional} = u_L - 2VENC_L \\ 3VENC_H < u_H - u_i < 5VENC_H &: u_{triconditional} = u_L + 4VENC_L \end{aligned}$$

$$-5VENC_H < u_H - u_i < -3VENC_H : u_{triconditional} = u_L - 4VENC_L$$

or

$$VENC_i < u_H - u_L < iVENC : u_{triconditional} = u_L + 2VENC_L$$
$$-3VENC_i < u_H - u_L < -iVENC : u_{triconditional} = u_L - 2VENC_L$$
$$3VENC_i < u_H - u_L < 5iVENC : u_{triconditional} = u_L + 4VENC_L$$
$$-5VENC_i < u_H - u_L < -3iVENC : u_{triconditional} = u_L - 4VENC_L$$

2.2.1.4 Optimal Dual-VENC Approach

Carrillo *et al.* (Carrillo *et al.*, 2018) proposed the Optimal Dual-VENC (ODV) method. This method is based on the formulation of the Dual-VENC problem as least-squares sum function. The cost function has the form:

$$J_{dual}(u) = \sum_{j=1}^{2}\left(1 - \cos\left(\frac{\pi}{VENC_j}(u_j - u)\right)\right) \quad (1.8)$$

In the ODV, the unwrapped motion corresponds to the global minimum with the smallest magnitude, which we will denote u_*. Note that the periodicity of $J_{dual}(u)$ is the least common multiplier between the periodicity of the single-VENC functions if $VENC_1/VENC_2$ is a rational number. That was recently mathematically proven in (Herthum *et al.*, 2020). Therefore, unwrapping is produced when half-of the periodicity of J_{dual} is larger than the true velocity. This allows $VENC_H$ to be smaller than the true velocity, and it is not required to construct a third velocity with iVENC. The periodicity depends on β and it corresponds to $2aVENC_H$, β = a/b, with a, b positive integers. It can be verified that iVENC match with $aVENC_H$ and iVENC when b = a + 1.

It is important to mention that u_* results in a combined version of u_H and u_L. Therefore, its variance is not the same as the one of u_L. In case that u_H and u_L are

i.i.d., the variance is reduced as it was proven in (Herthum *et al.,* 2020). However, this is no longer the case when u_1 and u_2 share the background phase. In that case the variance of u_* maybe even larger than for u_L depending on β. The detailed theoretical analysis is given in Appendix A.1.

In order to obtain comparable results with the other methods in terms of the variance of the unwrapped velocity, in this work we will adopt a simpler (and also computationally cheaper) version of ODV. To just use $J_{dual}(u)$ to guide the unwrapping of u_L, i.e., to find u_* by solving,

$$k_* = \arg\min_{k\in\mathbb{Z}} J_{dual}(u_L + 2VENC_L k), \quad \text{subject to} -VENC_{eff} \le u_L + 2VENC_L k \le VENC_{eff} \tag{1.9}$$

where the effective VENC is $VENC_{eff} = VENC_H \frac{\beta}{1-\beta}$ and then to set $u_* = u_L + 2VENC_L k$. This leads to $Var(u_*) = Var(u_L) = 2\sigma_\varphi^2 VENC_L^2$, as in the other methods. This approach was introduced - and applied to MR Elastography recently (Herthum et al., 2020).

2.2.1.5. Optimal Dual-VENC Correction Algorithm

Here we propose a new approach to improve the results of the ODV method. In the presence of noise, all methods may fail unwrap appropriately. However, in the case of the ODV, the cost function can be used to automatically detect potential failures and propose a corrected value.

To explain our ODV correction algorithm, an example is shown in the ascending aorta of a representative volunteer, Figure 2-1.a, with two pixels that the ODV method for ($VENC_1$, $VENC_2$) = (75, 50) was not able to correct, restricted in the red rectangle. We analyzed four points in the region of interest (ROI), two of them still had aliasing (points 1 and 3), and the other pixels the ODV found the true velocity values (points 2 and 4) as shown in Figure 2-1.b. The presence of noise deforms the dual-VENC functions, as in Figure 2-1.c, then the global minima with the smallest

absolute value will not be (close to) u_{true}, and velocity aliasing occurs, such as it occurs in points 1 and 3. Nevertheless, using the ODV formulation, we can correct it using the cost function values. Based on the considerations above, the ODV correction algorithm is as follows:

1. Locate 8-connected pixels for every image pixel for 2D.
2. Calculate the mean velocity of the neighborhood.
3. If this result does not have the same sign as the central pixel. Then, find the local minimum of $J_{dual}(u)$ with the smallest velocity value of the same sign as the neighborhood of the central pixel.
4. And finally, replace the velocity value corresponding to that local minimum of $J_{dual}(u)$ in the pixel of interest. The final result can be found in the Figure 2-1.d.

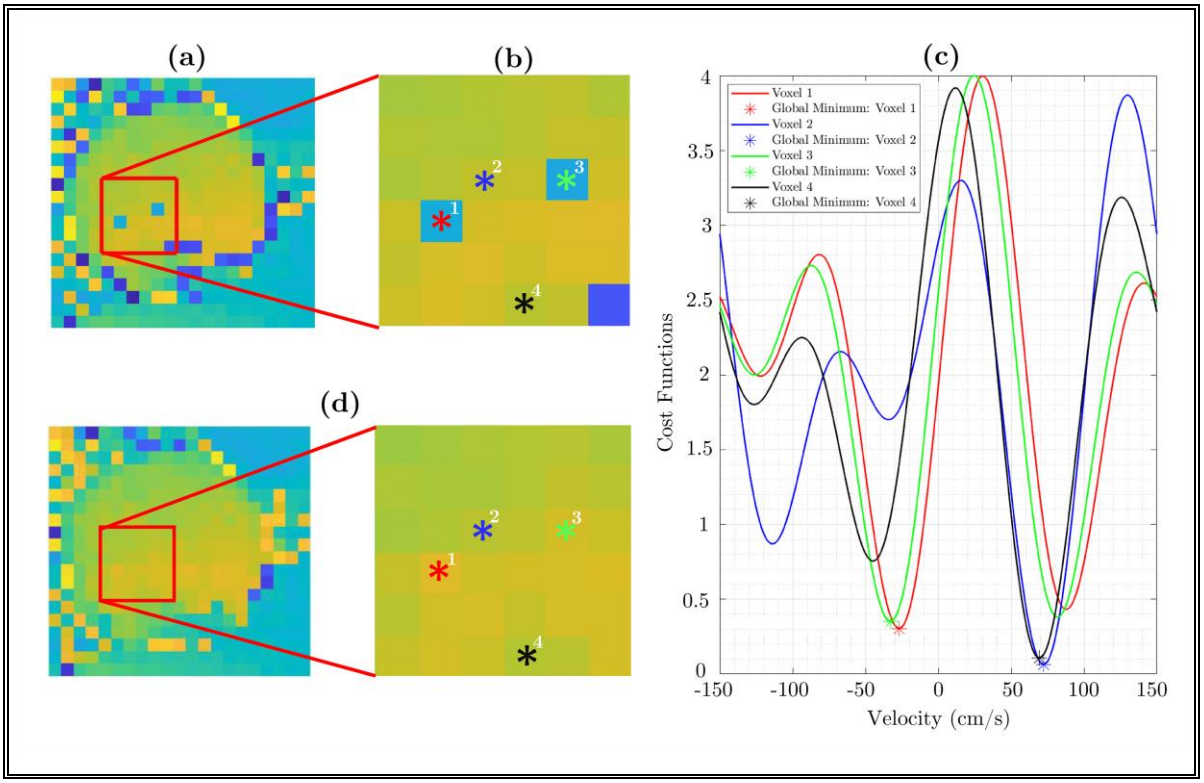

Figure 2-1. 2D PC-MRI for an ascending aorta of volunteer 1. (a) ODV 75,50 marking ROI, red rectangle. (b) ROI's zoom with points of interest. (c) Cost functions vs. velocity for each point of interest, with the global minimum marked as

asterisks. And (d) results of the ODV corrected methods marked the points of interest.

2.3. Methods

2.3.1. *In-vivo* Dataset

2D PC-MRI data were acquired in twenty-six volunteers, age 32.4 ± 11.6 years (range 22-73 years, nine females) using a clinical 1.5 T MR Scanner (Philips Achieva, Philips Medical Systems, Best, The Netherlands). The local committee approved the study, and informed consent was obtained from all participants. The protocol consisted of a through-plane 2D PC-MRI sequence perpendicular to ascending aorta above the Valsalva sinus. Acquisition parameters were: TE of 3.7 ms, TR of 5.5 ms, FA of 15°, VENCs of 50, 75, and 150 cm/s, Field-of-View (FOV) of 320 × 116 mm, Trigger Time 27 ms, 25 cardiac phases using prospective ECG triggering, in-plane resolution 1 × 1 × 8 mm3, and temporal resolution between 35-48 ms. The raw data was obtained, and the reconstruction of each bipolar gradient was performed offline using MATLAB. Data from a 5 elements phased-array cardiac coil were combined using the method proposed by Bernstein et al.19 and Nett et al.20. Since the acquisitions were performed using single-VENC protocols, we used the background phase from the scan with $VENC_H$ to reconstruct velocity image with the $VENC_L$. To compare the methods, we only used representative peak-systolic phase, when more aliasing occurs.

The in-vivo dataset was processed using an in-house MATLAB library (The MathWorks Inc., Natick, MA, USA), running in a 2.3 GHz Intel i7 processor equipped with 8GB of RAM, which included the data reconstruction, the implementation of the unwrapping methods (SDV, ODV, and bi- and tri-conditional), the ODV correction algorithm, the addition of artificial noise, and the analysis of the results.

2.3.2. Additional (Synthetic) Noise

We simulated different levels of noise for the in-vivo datasets. We assume three measurements with velocity encoding gradients $G_0 = 0 < G_H < G_L$, resulting in three measured complex magnetizations Z_{0k}, Z_{1k}, and Z_{2k}, for each coil k = 1,…,5,

$$\begin{aligned} Z_{0k} &= M_{0k}e^{i\emptyset_{0k}} \\ Z_{Hk} &= M_{Hk}e^{i\emptyset_{Hk}} \\ Z_{Lk} &= M_{Lk}e^{i\emptyset_{Lk}} \end{aligned} \tag{1.10}$$

The modulus of Z_k provides the single-coil magnitude image, M_k, and the subscripts H and L are related to phases acquired with high- and low-VENCs, respectively, and 0 to the background phase. For all magnetizations measurements, i.i.d. complex Gaussian noise $\varepsilon \sim \mathcal{N}(0,\sigma^2)$ was added with a variance of σ = M {0, 5, 10, 15} %, with M the maximal magnitude for all coils, voxels and encoding gradients. Denoting the perturbed measurements with a "hat", the phase-difference used in the velocity reconstruction for each voxel

$$\begin{aligned} \Delta\Phi_{H,L} &= \arg\left(\sum_k \widehat{Z_{(H,L)k}}\widehat{Z_{0k}}^*\right) \\ \Delta\Phi_i &= \arg\left(\sum_k \widehat{Z_{Hk}}\widehat{Z_{Lk}}^*\right) \end{aligned} \tag{1.11}$$

where * denotes complex conjugate and $\arg(A+iB)$ is the angle between the positive real axis and the line joining 0 and $A+iB$, in radians. Finally, the velocities $u_{H,L,i}$ are given by,

$$\begin{aligned} u_{H,L} &= \frac{\Delta\Phi_{H,L}}{\pi} VENC_{H,L} \\ u_i &= \frac{\Delta\Phi_i}{\pi} iVENC \end{aligned} \tag{1.12}$$

In order to compute the statistics of the results, we used 100 realizations of the noise.

2.3.3. VENC Combinations

In order to compare the methods, all used cases the VENC combinations: ($VENC_H$, $VENC_L$) = (150,75) cm/s, ($VENC_H$, $VENC_L$) = (150,50) cm/s, and ($VENC_H$, $VENC_L$) = (75,50) cm/s. The reasoning is that, according to the theory, this provides an effective VENC values of 150 cm/s, respectively, for all methods, since $\beta = VENC_L/VENC_H$ = 1/2, 1/3, and 2/3. Combining closer VENC values has been reported to have reduced noise robustness (Herthum *et al.*, 2020).

2.3.4. Unwrapping Performance Quantification

To quantify and compare the performance of the methods, we counted the number of aliased of pixels after the unwrapping methods for each set of additional noise levels.

In order to analyze only the results within the aortic lumen, we applied binary masks. First, we converted the magnitude image into a binary image. Then, we calculated the distance transform for the binary image. Due to the fact that the ascending (AAo) aorta has a circular geometry, we used the watershed transform (Preim *et al.*, 2013). Consequently, we identified the circle with the most extensive area. The segmentations were visually inspected and manually corrected if needed. Finally, we cropped the circles and automatically created the binary masks.

Then, we applied the mask to the result of each unwrapping method and VENCs combination and counted the pixels whose sign differed from the iVENC data.

2.3.5. Statistical Analysis

The datasets were checked for normality using a Shapiro-Wilk's normality test. The two-way ANOVA was conducted to examine the unwrap pixels by using the unwrapping methods with different noise levels. Homogeneity of variances was performed using Levene's test, with a p-value < 0.05 indicating statistical significance. Tukey's multiple post hoc analysis with Bonferroni correction were performed for pair-wise comparison of unwrapping methods and two groups of noise levels. The results of the *in-vivo* datasets were displayed in box-whisker plots. The statistical analysis was performed using the software R 4.1.1 (R Foundation for Statistical Computing, Vienna, Austria) (R Core Team 2013).

2.4. Results

Figure 2-2 illustrates the comparison of the unwrapping methods with different noise levels (0% and 10%) and VENCs combinations of a particular volunteer (26 years old, male). Figure A-1 shows the results for the same volunteer with 5% and 15% noise level. These examples demonstrated that without synthetic noise, all the methods delivered similar results. As expected, increasing the noise made all unwrapping methods less robust, making the difference in the results of the methods more appreciable. Moreover, the figure shows the pixels where there was a difference between the ODV and the ODV corrected method (eighth column). It is important to mention that with $\beta = 1/2$, the number of pixels corrected was less than $\beta = 1/3$ and $\beta = 2/3$.

To quantify the performance of the methods, the results in terms of unwrapping success in the AAo of all volunteers with a different VENCs combination are shown in Figure 3-2 and Figure A-2. Statistical analysis revealed that there were no extreme outliers, residuals were normally distributed ($p > 0.05$), and there was homogeneity of variances ($p > 0.05$). On the other hand, there was a statistically significant interaction between noise levels and the unwrapping method for the different VENCs combinations (iVENC, $VENC_H$, $VENC_L$) = (150, 150, 75),

(iVENC, $VENC_H$, $VENC_L$) = (75, 150, 50), (iVENC, $VENC_H$, $VENC_L$) = (150, 75, 50). Consequently, we found which pairs of unwrapping methods differed using the Turkey test receiving a Bonferroni adjustment, indicated with the line mark and asterisk. These results revealed a significant difference between the ODV corrected and the other methods for β = 1/2, β = 1/3, and β = 2/3 for both noise levels analyzed ($\sigma = 0{,}10\ \%$). Also, the ODV method presented statistically significant differences from the other methods with β = 1/3 and a noise level of 10%. Moreover, the figure shows the pixels where there was a difference between the ODV and the ODV corrected method (eighth column). It is important to mention that with β = 1/2, the number of pixels corrected were fewer than with β = 1/3 and β = 2/3.

For all methods and noise levels, the most robust VENC combination appeared to be $\beta = 1/2$, where $VENC_H = VENC_{eff}$ and $VENC_L = VENC_{eff}/2$, e.g., ($VENC_H$, $VENC_L$) = (150, 75) cm/s for (iVENC, $VENC_H$, $VENC_L$) = (150, 150, 75) cm/s. For $\beta = 1/3$, the reconstruction became less robust when increasing the noise level where $VENC_H = VENC_{eff}$ and $VENC_L = VENC_{eff}/3$ e.g., ($VENC_H$, $VENC_L$) = (150, 50) cm/s for (iVENC, $VENC_H$, $VENC_L$) = (75, 150, 50) cm/s. And finally, we obtained the less robust results with $\beta = 2/3$ where $VENC_H = VENC_{eff}/2$ and $VENC_L = VENC_{eff}/3$ e.g., ($VENC_H$, $VENC_L$) = (75, 50) cm/s for (iVENC, $VENC_H$, $VENC_L$) = (150, 75, 50) cm/s. Eventually, if β increased the distance in the cost functional is much smaller, which explained the errors of the method with $\beta = \{1/3, 2/3\}$, see details in (Herthum *et al.* 2022).

When comparing all methods, for each combination and noise level, the original ODV method showed the largest percentage of aliased pixels compared to the other of the methods for all VENC combinations and added noise. After that, the SDV, bi-conditional, and tri-conditional showed similar results. The best-performing method was the corrected ODV.

Computation times for a single volunteer dataset analyzed, the ODV and ODVcorrected were slower than the bi- and tri-conditional, and the SDV (ODV: ≈

1.11 s, ODVcorrected: ≈ 1.242 s, biconditional: ≈ 0.007 s, tri-conditional: ≈ 0.008 s, and SDV: ≈ 0.003 s).

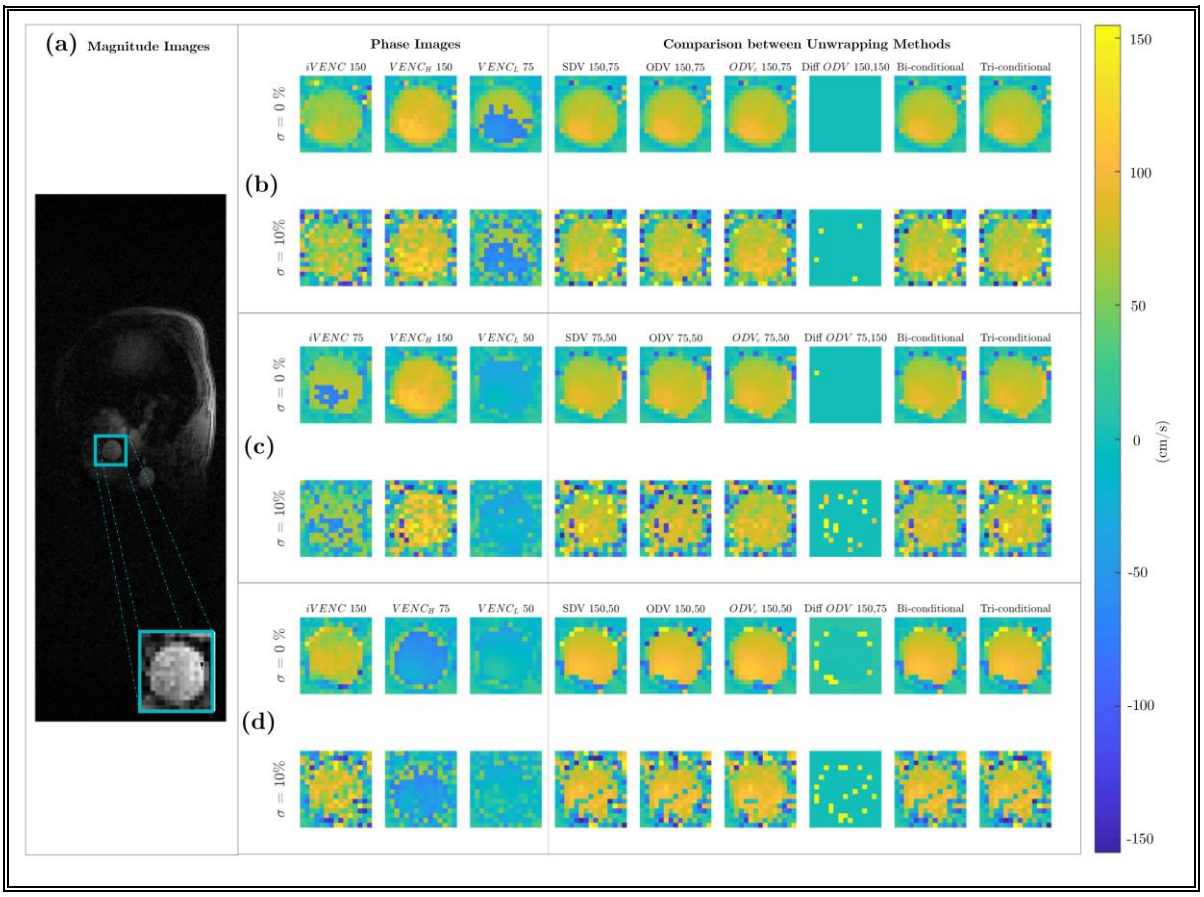

Figure 2-2. Ascending aorta at peak systole of a representative volunteer. (a) Magnitude Images: slice prescription and region-of-interest. Phase-differences images with VENCs combination of (b) (iVENC, $VENC_H$, $VENC_L$) = (150, 150, 75), (c) (iVENC, $VENC_H$, $VENC_L$) = (75, 150, 50) cm/s and (d) (iVENC, $VENC_H$, $VENC_L$) = (150, 75, 50) cm/s with different levels of synthetic noise, σ. The VENCs used by the SDV and ODV methods are in the top part of the figures. First column: iVENC, second column: $VENC_H$, third column $VENC_L$, fourth column: SDV, fifth column: ODV, sixth column: ODV corrected, seventh column: Different between the ODV and ODC corrected method, eighth column: bi-conditional, and ninth column: tri-conditional methods.

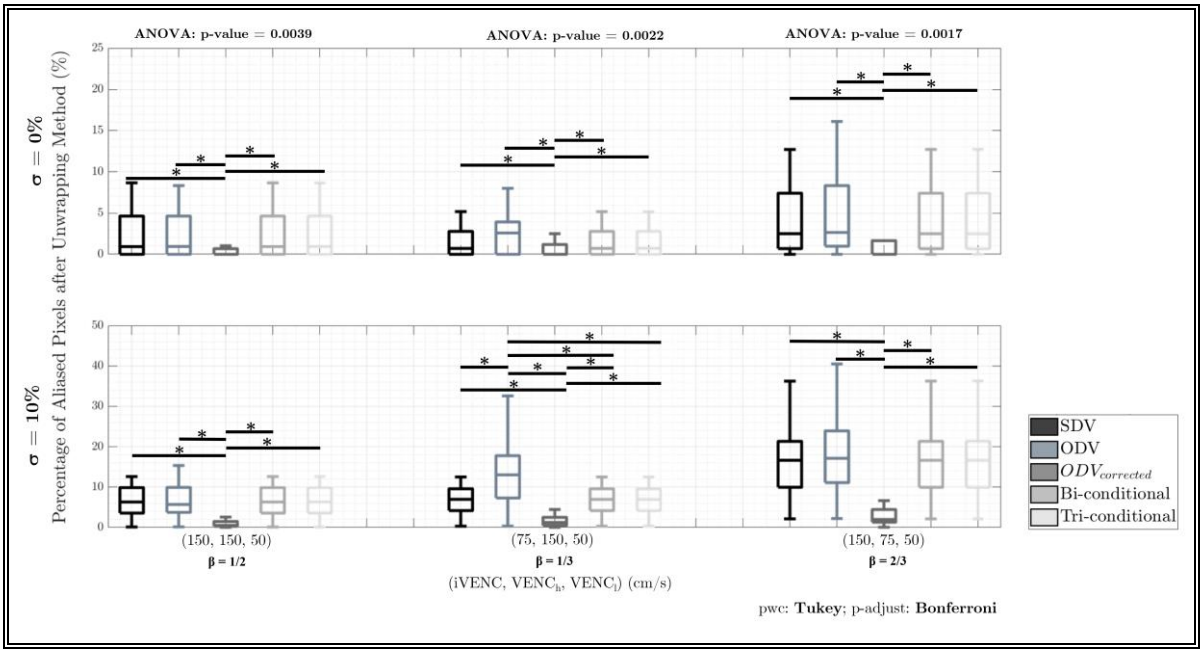

Figure 2-3. Box whisker plots for the evaluation of unwrapping methods of the volunteers at peak-systole in the ascending aorta with different levels of synthetic noise, σ, with VENCs combination of (first column) (iVENC, $VENC_H$, $VENC_L$) = (150, 150, 75) cm/s, (second column) (iVENC, $VENC_H$, $VENC_L$) = (75, 150, 50) cm/s, and (third column) (iVENC, $VENC_H$, $VENC_L$) = (150, 75, 50) cm/s. The SDV and ODV methods used in (first column) ($VENC_H$, $VENC_L$) = (150,75) cm/s β =1/2, (second column) ($VENC_H$, $VENC_L$) = (150, 50) cm/s β = 1/3, and (third column) the SDV (iVENC, $VENC_L$) = (150, 50) cm/s β = 1/3 and the ODV method ($VENC_H$, $VENC_L$) = (75, 50) cm/s β = 2/3. Aliased number of pixels after the unwrapping methods were performed as a percentage. On each box, the central mark is the median, the bottom and top edges of the box are the 25^{th} and 75^{th} percentiles, respectively, and the whiskers extend to the most extreme data points not considered outliers. The significance of the interaction between noise levels and the unwrapping method for the different VENCs combinations is in the top part of the figures with their p-values. The symbol * indicates statistically significant differences ($p < 0.05$).

2.5. Discussion

This work reviewed, theoretically analyzed, and compared five unwrapping methods based on an *in-vivo* dataset based on two acquired VENCs: the SDV, ODV, ODV corrected, and bi- and tri- conditional methods, where we developed the ODV corrected method based on theoretical considerations. This is the first reported comparison of all these methods.

It was shown that the most robust unwrapping method appeared to be the corrected ODV method without noise. In contrast, the other methods showed similar performance in unwrapping success for all values of β tested in this work.

With the addition of synthetic noise to the in-vivo datasets, the percentage of failed unwrapping increased for all values of β. We found that for $\beta = VENC_L/VENC_H = ½$ all methods performed similarly. These results were consistent with Carrillo *et al.* (Carrillo *et al.* 2018) and Herthum *et al*. (Herthum *et al.* 2022). For that β value, the most robust unwrapping methods appeared to be the corrected ODV method ($p < 0.005$), obtaining the lowest failure percentage (mean values for: β = 1/2, 0.68% and 0.93% for noise levels of 0% and 10%, respectively; β = 1/3, 0.99% and 1.83% for noise levels of 0% and 10%, respectively; and β = 2/3, 3.94% and 4.36% for noise levels of 0% and 10%, respectively) compared with the other methods. Our statistical analysis can adequately determine the difference between the pair of unwrapping methods. We considered the mean percentage of aliased pixels after two unwrapping methods of 10% and 11%, respectively, and a standard deviation of 1% with a power of 0.8. Furthermore, the unwrapping method had similar behavior independent of the noise level. As expected, as noise level increased of the number of aliased pixels increases as well.

To make a fair comparison among all methods, we took full advantage of the VENCs proposed by Ma *et al.* (Ma *et al.* 2020). For the SDV approach, in case iVENC > VENCH, we used u_i rather than u_H as the original SDV would have used it, maintaining the effective VENC value. Otherwise, Lee *et al*. (Le *et al.* 1995) reported that the SDV method cannot handle the aliasing when both VENC values are lower than the maximum velocity.

Carrillo et all did not perform a detailed analysis of robustness of unwrapping methods to noise, only qualitatively on synthetic data. Here, we presented such analysis both numerically and theoretically. For the ODV method, here we used the "reduced" version recently reported by Herthum *et al.* (Herthum *et al.* 2022). This is based on the statistical analysis in Appendix A, which includes the fact that the velocity images shared the background phase with different VENC values. Furthermore, we developed a correction method for the ODV based on the additional information provided by the method. Although it works for single isolated pixels with incorrect values, it is important to mention that our algorithm may fail in a region with contiguous and wrapped pixels if the number of aliased pixels is similar to the number of pixels in the window kernel. Nevertheless, as we observed in the experiments, the correction algorithm worked adequately, even in extreme cases as when we added 15% noise to the images. In that case, we had a few contiguous pixels aliased, and the algorithm unwrapped most of them. Also, our correction required more computational time than the ODV method. However, the ODV method was slower than SDV, bi-, and tri-conditional methods. Nevertheless, the computing time remained in the order of seconds, and therefore, it should not affect the applicability of the (corrected) ODV methods in clinical practice. It is important to clarify that we limited our study to methods where the velocity encoding is varied within the same spatial direction. Approaches using "diagonal" directions such as Johnson *et al.* and Zwart *et al.* (Johnson *et al.* 2010) (Zwart *et al.* 2013) were not included in the analysis since they dealt with different input images.

2.6. Limitations

From the acquisition point of view, the PC- MRI data were acquired using standard single-VENC PC-MRI sequences. Nevertheless, we performed the acquisitions so that all other acquisition parameters except VENC had the same value. Further, we only used one common phase to process all data for all methods,

and therefore, this single VENC acquisition would not affect the comparison of all methods. Another limitation is that all methods were assessed in healthy volunteers; future studies will investigate all methods in patients with stenotic valves, areas with high velocity, or in 4D flow sequences of a large FOV. Another issue is that phase errors could arise from a patient's motion during the MRI acquisition (Bernstein *et al.* 1992). We attempted to control this factor to the best of our ability, as the acquisition was performed under breath-holds; any residual motion may have affected all methods similarly as all methods were acquired in the same scan session. Finally, although we tested the method on 26 volunteers, future work will use a flow phantom to test these methods in a controlled experiment. Using a phantom flow will allow us to test the Dual-VENC unwrapping methods under different conditions of flow (turbulent and retrograde conditions), noise, and resolutions (Montalba *et al.* 2018).

2.7. Conclusions

In this study, we found that the quality of the results depends on the proportion of the VENCs of the input images, with $VENC_H/VENC_L$ = 0.5 being the best performing combination for all methods. For that VENC combination, the most robust unwrapping methods to noise was the corrected ODV approach, while the other methods show a similar performance in terms of unwrapping success.

2.8. Acknowledgements

Millennium Science Initiative of the Ministry of Economy, Development and Tourism, grants Nucleus for Cardiovascular Magnetic Resonance. We are also grateful to the Biomedical Imaging Center at Pontificia Universidad Católica de Chile, CMM ANID PIA AFB170001, and project CORFO 10CEII-9157 Inria, Chile.

3. SECOND ARTICLE: COMPREHENSIVE ASSESSMENT OF LEFT INTRAVENTRICULAR HEMODYNAMIC USING A FINITE ELEMENT METHOD: AND APPLICATION TO DILATED CARDIOMYOPATHY PATIENTS

3.1. Introduction

Dilated cardiomyopathy (DCM) is more common than non-ischemic cardiomyopathy and leads to left ventricular dilation and systolic and diastolic dysfunction (Hershberger *et al*., 2007) (Mahmaljv, *et al*., 2021). The process that alters the heart's size, geometry, and function is associated with increased hemodynamic demands, which cause abnormal mechanical stress in the muscle (Hill, *et al*., 2008) (Wong *et al*., 2004). The progression is associated with an incremented risk of heart failure and sudden cardiac death (McNally *et al*., 2007). However, poor survival and high mortality rate reveal that effective treatment of DCM-related heart failure remains challenging. Pharmacological and resynchronization therapies have improved DCM treatment by halting disease progression and leading to reverse remodeling (Hershberger *et al*., 2007).

The preferred imaging technique for assessing the heat in DCM patients is cardiovascular magnetic resonance (CMR). CMR allows the acquisition of anatomical, cine, and velocity images, including 4D Flow MR (McNally *et al*., 2007) (Frangi *et al*., 2007) (Markl *et al*., 2012) (Dyverfeldt *et al*., 2015).

4D Flow allows a qualitative and quantitative analysis of several hemodynamic parameters. It has been applied extensively in the great vessels, particularly in the aorta (Sotelo *et al*., 2016) (Sotelo *et al*., 2018) and in the left ventricle (LV) for assessing intraventricular flow in some cardiovascular diseases (Wong *et al*., 2009) (Töger *et al*., 2012) (Al-Wakeel *et al*., 2015) (Svalbring *et al*., 2016) (Hirtler *et al*., 2016) (Suwa *et al*., 2016) (Browning *et al*., 2017) (Fredriksson *et al*., 2018). Previous studies have demonstrated that lower kinetic energy values in diastole are associated with the deterioration of ventricular filling, induced by morphological

alteration commonly found in Fontan patients, mitral regurgitation, and LV dysfunction or remodeling (Al-Wakeel *et al*., 2015) (Svalbring *et al*., 2016) (Fredriksson *et al*., 2018). Additionally, turbulent kinetic energy has shown a stronger association with the ventricle's remodeling in patients with Tetralogy of Fallot and higher values in DCM patients compared with normal subjects (Töger *et al*., 2012). Vortex formation has been studied qualitatively (vortex size and location) and quantitatively (Lagrangian Coherent Structures and the curl of velocity) (Kanski *et al*., 2015) (Hirtler *et al*., 2016) (Suwa *et al*., 2016) (Browning *et al*., 2017). These studies suggest that parameters associated with the 3D intraventricular flow may be critical for LV filling and ejection and could be relevant to the development of dilation, dysfunction, and prognosis in patients with heart diseases. While these measures have a potential role in describing intraventricular flow, the difficulties of implementing them have led to the analysis of only a few combinations of these parameters in a single cohort of patients (Kanski *et al*., 2015) (Hirtler *et al*., 2016) (Suwa *et al*., 2016) (Sotelo *et al*., 2016) (Browning *et al*., 2017) (Sotelo *et al*., 2018).

Due to the multidirectional velocity data, although impressively comprehensive, it may need to be supplemented by more selective flow imaging at high temporal and spatial resolutions or computational fluid dynamics simulation. Reaching conclusions regarding small-scale methodology, which comprehensively describes the characteristics of intraventricular flow, could improve the use of intraventricular 4D Flow for clinical research and potential translation to clinical settings.

In this work, we adapted a method for quantifying 4D Flow in the aorta (Kanski *et al*., 2015) (Sotelo *et al*., 2016) (Sotelo *et al*., 2018). We modified the methodology applied in the left ventricle to obtain several hemodynamic parameters from a single segmentation from a 4D Flow dataset and cine MRI. To show the applicability of this approach, we performed a proof-of-concept study in which we applied the method in a small cohort of DCM patients to find which parameters were different from volunteers. We obtained three-dimensional hemodynamic parameters, including kinetic energy, vorticity, helicity density, viscous dissipation, and energy loss (Pedrizzetti *et al*., 2014) (Sotelo *et al*., 2015) (Al-Wakeel *et al*.,

2015) (Zajac *et al*., 2015) (Arvidsson *et al*., 2016) (Sjöberg *et al*., 2017) (Sotelo *et al*., 2018).

3.2. Materials and Methods

3.2.1. Population

Table 3-1. Demographical and clinical data for healthy and DCM patients. All quantitative data are expressed as the median (range). HR: Heart Rate, EF: Ejection Fraction, LVSV: Left Ventricle Stroke Volume, CO: Cardiac Output, LVEDV: Left Ventricle End-Diastolic Volume, and LVESV: Left Ventricle End-Systolic Volume. * indicates statistically significant differences ($p < 0.05$).

				DCM Group		
	HV	**DCM**	***p*-Value**	**LVEF ≥ 50 (Complete-Responders)**	**LVEF < 50 (Non-Responders)**	***p*-Value**
N	12	13		5	8	
Age (years)	39 (27,55)	51 (29,62)	0.060	40 (29,62)	53 (44,58)	0.502
Gender (female:male)	5:7	6:7	0.821	3:2	3:5	0.429
Weight (kg)	68 (50,111)	83 (43,116)	0.213	90 (72,116)	72.5 (43,95)	0.071
Height (cm)	173 (163,188)	168 (155,178)	0.203	168 (163,178)	166.5(155,175)	0.454
HR (bpm)	64 (58,78)	65 (56,101)	0.743	65 (56,101)	67.5 (57,89)	0.698
EF (%)	62.7 (54,69)	46 (29,66)	< 0.001*	55 (51,66)	44 (29,48)	0.002*
LVSV (mL)	95.5 (66.3,122.9)	62 (53,132.1)	0.039*	61 (53,89)	79 (55,132,1)	0.183
CO (L/min)	6.4 (4.8,7.9)	6.1 (4.4,7.9)	0.327	6.3 (5.2,7.9)	5.9 (4.4,7.7)	0.524
LVEDV (mL)	153 (105.6,197.1)	199(125,364.2)	0.015*	187 (151,201)	219.5 (125,364.2)	0.050*
LVESV (mL)	51 (39,88)	92 (37,232.1)	0.004*	75 (37,92)	125 (68,232.1)	0.045*

A total of twelve healthy volunteers (HV), mean age 40.8 years (range 27–55 years), and thirteen DCM patients, mean age 48.7 years (range 29–62 years),

matched according to age and gender, were included in this research. Demographical and clinical data are described in Table 1. At the time of diagnosis, DCM was defined as the presence of symptoms and signs of heart failure with echocardiographic signs of ventricular enlargement and systolic myocardial dysfunction in the absence of hypertension, valve diseases, or significant coronary artery diseases sufficient to cause global systolic impairment, by the definition of the European Society of Cardiology (Elliott *et al*., 2008). Our DCM cohort all received treatment with an improved LV ejection fraction (range 51–66%) and LV volume indices at CMR imaging. All patients received standard guideline-directed treatment for DCM following the 2008 heart failure guidelines from the European society of cardiology. The details of treatments were not available, as our center is the referral center for several clinics for cardiac CMR. The HV had normal electrocardiograms and echocardiographic examinations without valvular or ventricular dysfunction. All subjects participated under informed consent, with data collection approved by the Regional Ethics Committee, South East London, UK (REC, 12/LO/1456).

3.2.2. Data Acquisition

Multi-slice 2D cine balanced steady-state free precession (b-SSFP) and 4D Flow MRI data were acquired in all subjects using a clinical 1.5 T MT Scanner (Philips Achieva, Philips Medical Systems, Best, The Netherlands). During the MRI examination, multi-slice b-SSFP was used to acquire short-axis morphological images in 40 frames with 8 mm slice thickness, using retrospective cardiac gating. Acquisition parameters were echo time (TE) 1.4 ms, repetition time (TR) of 2.8 ms, flip angle (FA) of 60° and acquired and reconstructed pixel sizes were 2.47 × 2.53 mm^2 and 1.45 mm^2, respectively. 4D Flow MRI data were acquired during free-breathing with MR parameters, as follows: TE of 2.3 ms, TR of 4.7 ms, FA of 6°, velocity encoding of 130 cm/s, and spatial resolution (acquired and reconstructed) 2.5 × 2.5 × 2.5 mm^3. These settings gave a temporal resolution of 58 ms. After the

acquisition, the 4D Flow MRI data were reconstructed into 24 cardiac phases on the MRI system.

3.2.3. Data Analysis

The 4D Flow MRI datasets were processed using an-house MATLAB library (The MathWorks Inc., Natick, MA, USA), which included the registration of the b-SSFP cine and 4D Flow MR images, interpolation of the b-SSFP images, segmentation of the LV, and generation of the finite element mesh (Figure 3-1). The Eidolon software was used to perform the registration between the multi-slice b-SSFP and the 4D Flow MRI (King's College London, London, UK) (Kerfoot *et al*., 2016). To obtain a smooth tetrahedral mesh, we doubled the number of slices in the b-SSFP images by using a cubic interpolation of values at neighboring grid points in each respective dimension, obtaining a final voxel size of 1.43 × 1.43 × 4.04 mm^3. LV endocardium was automatically segmented throughout all cardiac phases in the short-axis cine b-SSFP images, using the image analysis software Segment v2.2R6410 (Medviso AB, Lund, Sweden) (Heiberg *et al*., 2005) (Heiberg *et al*., 2010) (Tufversson *et al*., 2015). The segmentation was visually inspected and manually corrected if needed. Segmentations were then used to generate a binary mask. Afterward, we created a tetrahedral mesh using the iso2mesh MATLAB Toolbox (Fang *et al*., 2009). Once the mesh was constructed, we computed the velocity vector at each mesh node from the 4D Flow datasets using a cubic interpolation. 3D maps of vorticity, helicity density, viscous dissipation, energy loss, and kinetic energy fields were then calculated using a previously published finite element approach (Sotelo *et al*., 2015) (Sotelo *et al*., 2016) (Sotelo *et al*., 2018). The description of the equations used to calculate each hemodynamic parameter is presented in Table B.1. The parameters were averaged at peak systole, e-wave, and end-diastole using one timeframe before and after to reduce noise in the data.

3.2.4. Local Hemodynamics

A 16-segment model was used to divide the LV. In contrast to a standardized nomenclature, a minor adjustment was made (Elliott *et al.*, 2008). Due to the generally intricate shape of the apical region of the LV, region 17 was excluded from our analysis. Accordingly, LV mesh was divided into 16 segmentations. The centerline of the LV was calculated automatically by detecting the centroid of the LV contour in each slice and connected to create a line. To determine the three sections of the LV, we divided the centerline into three equal parts perpendicular to the long axis of the heart. An additional point was then manually placed at the junction between the right ventricular free wall and the interventricular septum on the LV. Based on these positions, landmarks were uniformly distributed along the boundaries. Each section was then partitioned into six segments of 60° each on basal and mid-cavity sections and four segments of 90° each on apical section (Figure 3-1f). Finally, for visualization purposes, we used the scientific software ParaView version 5.3.0 (Kitware, Clifton Park, NY, USA).

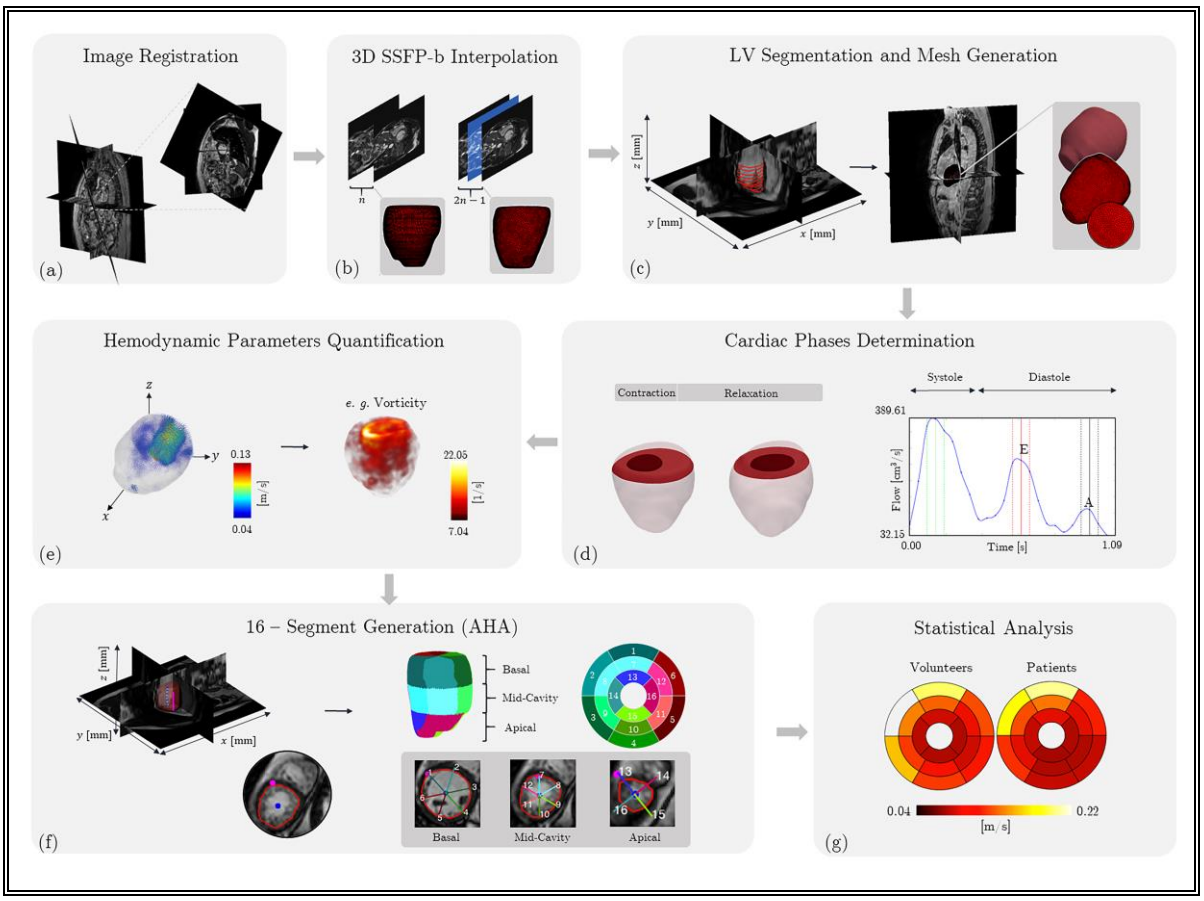

Figure 3-1. Schematic description of the quantification process. (a) First, we performed registration of the 4D Flow with the b-SSFP images. (b) Second, we doubled the number of slices in the b-SSFP images, (c) then the LV segmentation and tetrahedral mesh were generated. (d) We estimated the cardiac phases under study (e), and we transferred the velocity information at each node of the mesh from the 4D Flow MRI datasets using cubic interpolation. (f) Then, we calculated hemodynamic parameters under study. (g) Finally, the mean values of hemodynamic parameters were included in a bullseye plot to compare volunteers and DCM patients.

3.2.5. Statistical Analyses

Normal distribution in population demographics was evaluated using the Shapiro-Wilk test. Differences between groups for continuous parameters were

assessed by a Student t-test if they presented a normal distribution, and the Mann-Whitney U test otherwise. The $\chi 2$ test was applied for categorical variables, which were reported as percentages. A p-value < 0.05 was considered statistically significant. The statistical analyses were performed using GraphPad Prism version 6.0.1 (GraphPad Software Inc., San Diego, CA, USA).

These data were displayed in box-whisker and bullseye plots for global and local analyses, respectively. Additionality, a correlation matrix-based hierarchical clustering method was introduced to extract multiple correlation patterns from hemodynamic parameters. This method can effectively identify highly correlated data. The results are described with a tree structure plot called a dendrogram. The present study used Pearson's correlation method to measure the similarity between hemodynamic parameters (Gu *et al.*, 2010).

Furthermore, a sensitivity study was performed by looking at changes in the hemodynamic parameters subjected to the LV segmentation changes. We increased and decreased the size of the LV cavity from the first segmentations by moving the segmentation contour in 0.5 to 2 pixels of the b-SSFP image, equivalent to 0.72 to 2.89 mm. We compared the results with the original LV segmentation's respective mean value at each cardiac phase studied. We used the Kruskal-Wallis test to compare the variables across the different LV segmentation, with a p-value < 0.05 indicating statistical significance. The significance level was adjusted by using Dunn's test correction.

To assess the inter-observer agreement, data were analyzed by two independent observers, one with three years of experience in MR LV quantification and the other a medical technologist with no previous experience in this field. In addition, re-analyzed images with a 1-month interval to evaluate the intra-observer reproducibility. Inter- and intra-observer reproducibility were analyzed using Bland-Altman plots, and the results are shown in Appendix B.

3.3. Results

3.3.1. Study Population

There were no significant differences in age and heart rate (Table 3-1). However, ejection fraction and stroke volume were lower in DCM patients than volunteers, while end diastolic and end-systolic volumes were larger. These changes indicated that the LV in DCM patients was enlarged and its cardiac function was reduced, which is consistent with the pathological characteristics of DCM (Hershberger *et al.,* 2007) (Mashmaljy *et al.,* 2021). Additionally, eight patients still showed significantly impaired systolic function at CMR's time (non-responders), and five patients showed a complete response to treatment (complete responders). Between DCM groups, complete- vs. non-responders, there were differences in ejection fraction, end-diastolic volume, and end-systolic volume.

3.3.2. Global Hemodynamics

Assessment of global hemodynamic parameters is shown in Figure 3-2 and Table 3-2. Volunteers showed higher hemodynamics values than patients at peak systole and e-wave, except for helicity density. Remarkably, hemodynamic parameters in complete responder DCM patients remained low compared to volunteers. We found statistical differences between HV and DCM patients: non- and complete responders at peak systole and e-wave in velocity, vorticity, viscous dissipation, energy loss, and kinetic energy. In all cases, p-values were lower or equal to 0.005. There were no statistical differences in the parameters at end-diastole. Furthermore, we did not find statistical differences between DCM groups. In addition, ROC curves showed that previous parameters discriminated between HV and DCM patients (Figure A.7).

Table 3-2. Global hemodynamics data for HV, complete-, and non-responders DCM patients. All quantitative data are expressed as the mean ± standard deviation. *,+ Indicates statistically significant differences ($p < 0.05$).

		DCM Group		*p*-Value	
	HV	**Complete-Responders**	**Non-Responders**	**HV vs. Complete-Responders**	**HV vs. Non-Responders**
Peak-systole					
Velocity (m/s)	0.140 ± 0.014	0.099 ± 0.007	0.096 ± 0.008	<0.001 *	<0.001 +
Kinetic Energy (μJ)	43.722 ± 4.592	29.335 ± 1.917	31.288 ± 2.044	<0.001 *	<0.001 +
Vorticity (1/s)	20.306 ± 2.075	12.934 ± 0.814	13.331 ± 1.251	<0.001 *	<0.001 +
Helicity Density (m/s^2)	−0.042 ± 0.004	0.036 ± 0.161	−0.077 ± 0.139	0.125	0.417
Viscous Dissipation ($1/s^2$)	970.840 ± 412.093	412.093 ± 61.107	421.080 ± 54.870	<0.001 *	<0.001 +
Energy Loss (ηW)	173.080 ± 39.387	35.284 ± 14.144	47.734 ± 12.935	<0.001 *	<0.001 +
E-wave					
Velocity (m/s)	0.187 ± 0.059	0.097 ± 0.004	0.099 ± 0.014	0.007 *	<0.001 +
Kinetic Energy (μJ)	5.567 ± 1.810	3.008 ± 0.074	3.005 ± 0.423	0.007 *	<0.001 +
Vorticity (1/s)	26.309 ± 7.895	14.633 ± 0.755	14.931 ± 1.963	0.005 *	<0.001 +
Helicity Density (m/s^2)	0.106 ± 0.441	0.077 ± 0.065	0.056 ± 0.119	0.907	0.785
Viscous Dissipation ($1/s^2$)	1208.091 ± 574.696	393.994 ± 26.632	370.314 ± 80.785	0.007 *	<0.001 +
Energy Loss (ηW)	217.440 ± 126.751	28.408 ± 6.340	24.329 ± 11.540	0.005 *	<0.001 +
End-Diastole					
Velocity (m/s)	0.075 ± 0.015	0.077 ± 0.005	0.073 ± 0.002	0.796	0.673
Kinetic Energy (μJ)	2.291 ± 0.423	2.359 ± 0.165	2.266 ± 0.063	0.739	0.871
Vorticity (1/s)	13.629 ± 2.255	12.444 ± 0.633	12.203 ± 0.552	0.273	0.099
Helicity Density (m/s^2)	−0.025 ± 0.084	−0.082 ± 0.064	−0.027 ± 0.096	0.201	0.979
Viscous Dissipation ($1/s^2$)	300.577 ± 89.250	289.131 ± 54.300	256.496 ± 16.779	0.795	0.188
Energy Loss (ηW)	11.162 ± 7.191	10.459 ± 7.757	8.875 ± 1.896	0.859	0.395

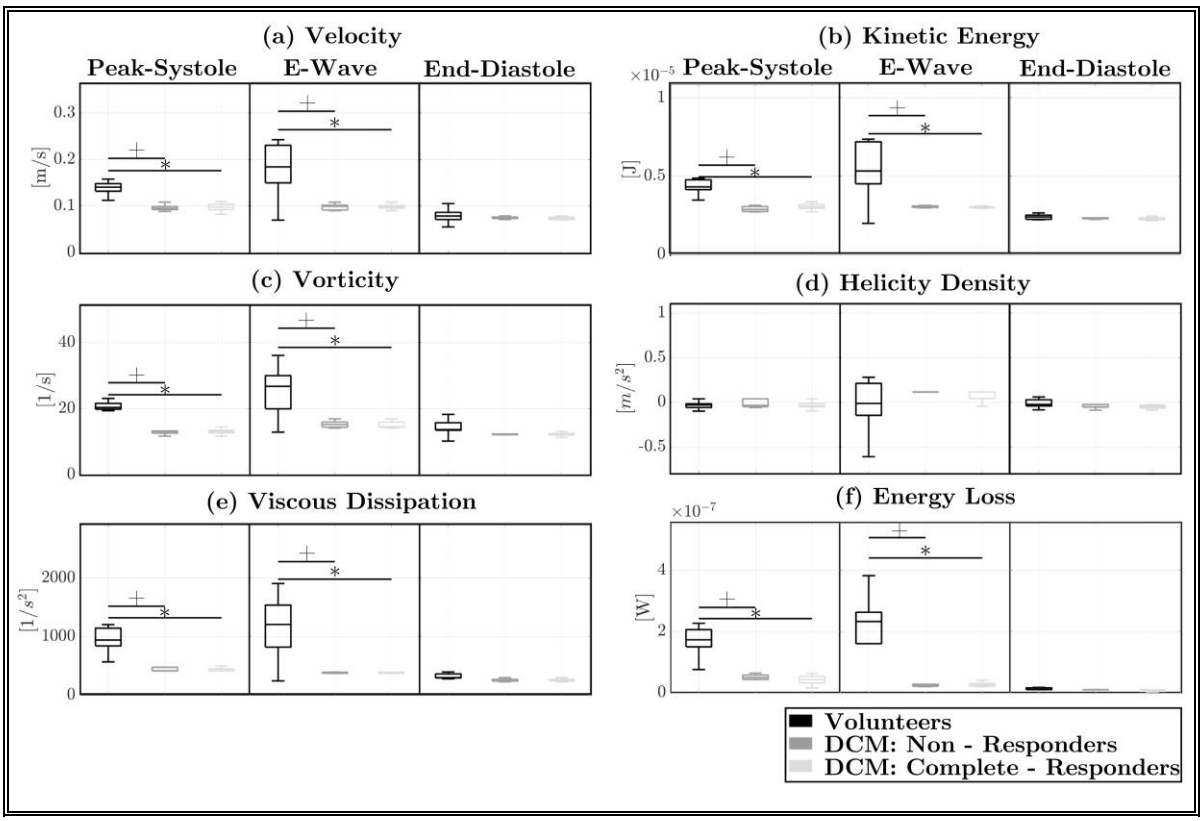

Figure 3-2. Box whisker plots for hemodynamic parameters (**a**–**f**) in the entire LV cavity of HV and DCM patients groups at peak systole, e-wave, and end-diastole. On each box, the central mark is the median, the bottom and top edges of the box are the 25th and 75th percentiles, respectively, and the whiskers extend to the most extreme data points not considered outliers. *,+ Indicates statistically significant differences ($p < 0.05$).extreme data points not considered outliers. *,+ Indicates statistically significant differences ($p < 0.05$).

The total computational time used to process the data, once the multi-slice b-SSFP was segmented and registered, varied between 30–40 s for one cardiac phase, using a standard computer (3.4 GHz Intel ® Core i7TM, 16 GB RAM).

Hierarchical cluster analysis (Figure 3-3) provides an alternative method for reliable identification of correlation between ejection fraction and hemodynamics parameters from 4D-flow MRI. According to their similarities, they are classified into two clusters identified at peak-systole, e-wave, and end-diastole. At peak-systole and e-wave, cluster 1 (black): helicity density; and cluster 2 (red): ejection

fraction, energy loss, vorticity, viscous dissipation, velocity, and kinetic energy. Finally, at end-diastole, cluster 1 (red): helicity density and ejection fraction, and cluster 2 (red): energy loss, viscous dissipation, vorticity, velocity, and kinetic energy. This means that ejection fraction correlates with all parameters except helicity density at peak systole and e-wave.

3.3.3. Sensitivity Study, Intra-, and Inter-Observer Reproducibility

Figure 3-4 shows a sensitivity analysis at peak-systole. The relative error in LV cardiac volumes and helicity density did not show significant differences between groups across LV segmentation. There were significant differences for some segmentation for the other parameters, particularly for the velocity magnitude, energy loss, and kinetic energy. The hemodynamic parameters showed a relative error proportional to the dilatation or erosion of the contour in the segmentation. When the segmentation was dilated or eroded 1 pixel or less, the relative error differences, with respect to the original segmentation for volunteers and DCM patients, were: velocity magnitude (9.03%, 6.78%), vorticity magnitude (5.49%, 2.74%), helicity density (12.11%, 13.98%), viscous dissipation (6.31%, 3.34%), energy loss (3.59%, 5.89%), and kinetic energy (7.66%, 6.09%). Similar results were obtained at e-wave and end-diastole, as shown in Figures B.8 and B.9. Those errors were more significant, particularly when the segmentation was dilated or eroded by more than 1 pixel. Helicity density and energy loss showed greater dependency on the segmentation error.

Regarding reproducibility, there was an excellent agreement of inter- and intra-observer analysis of global hemodynamic parameters. Details are given in the Appendix B.

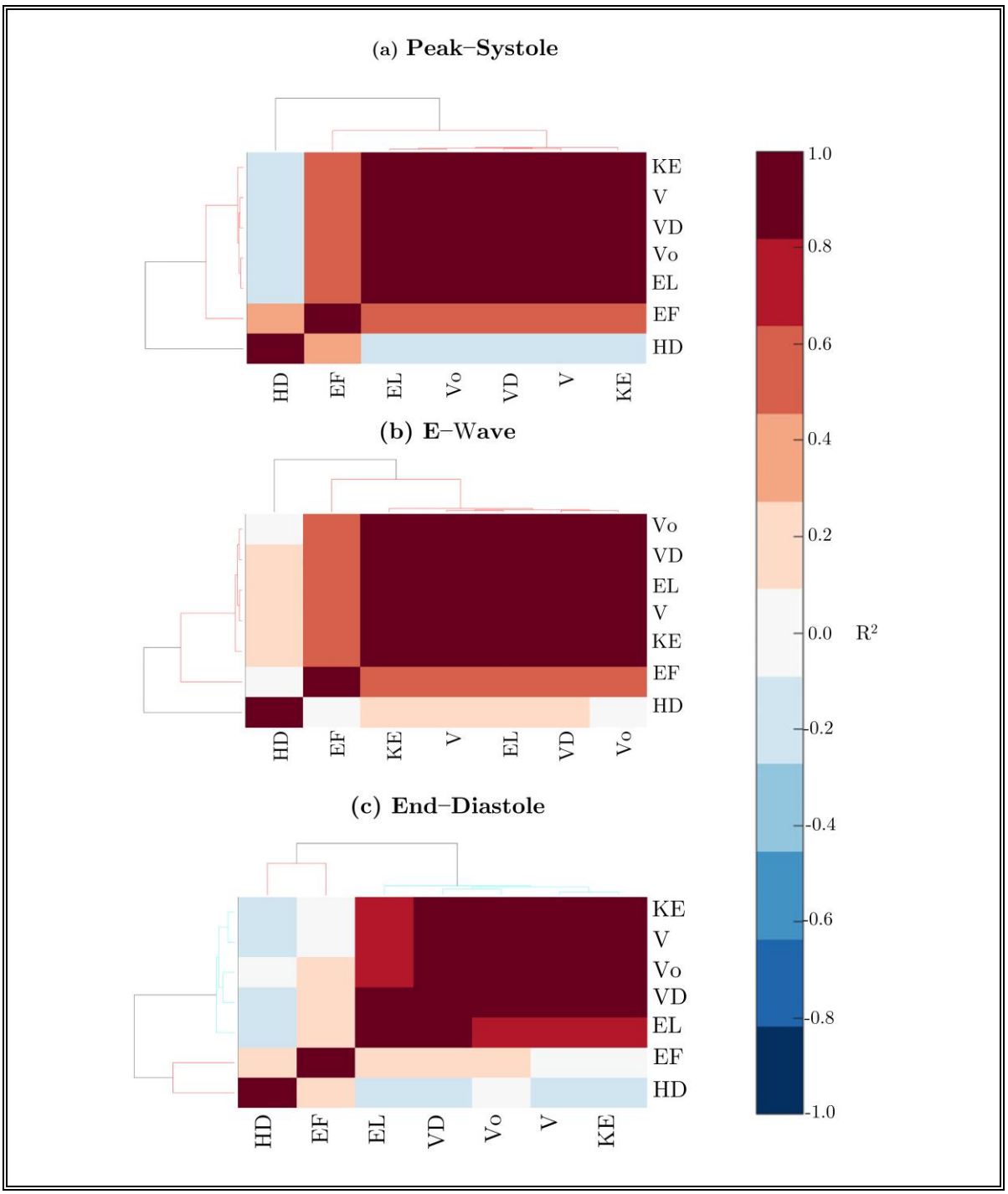

Figure 3-3. Dendrogram and hierarchical clustering results based on average linkage method for ejection fraction and hemodynamic parameters. EF: ejection fraction, V: velocity, KE: kinetic energy, Vo: vorticity, HD: helicity density, VD: viscous dissipation, and EL: energy loss.

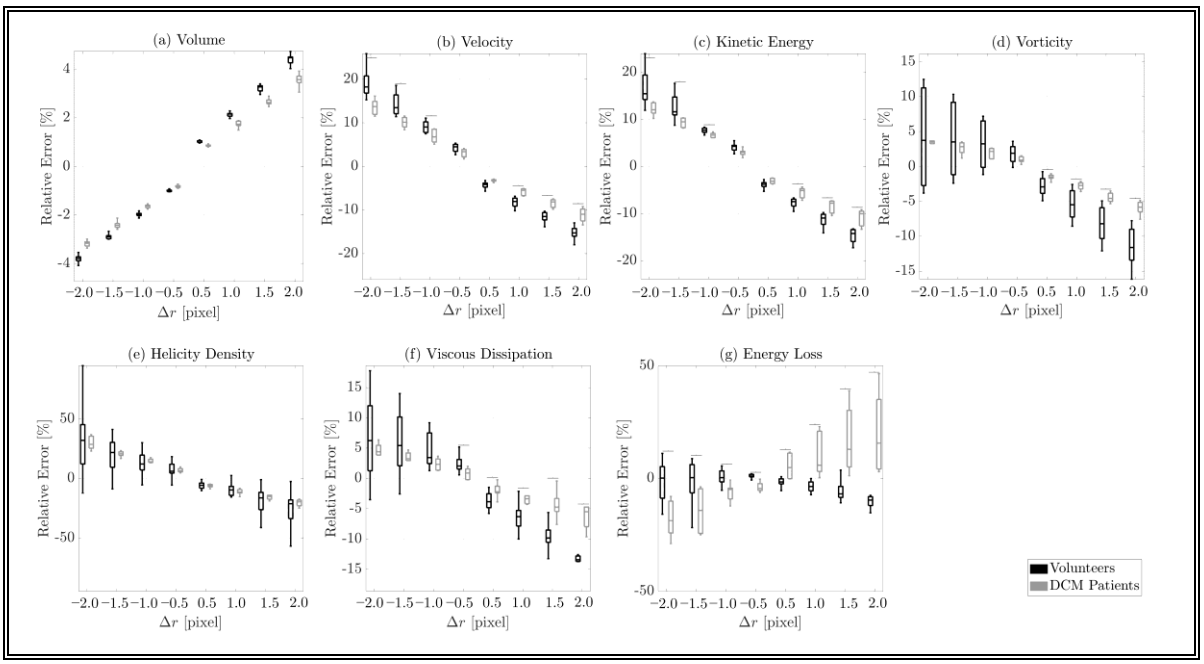

Figure 3-4. Relative error values of the volume (a) and each hemodynamic parameter (b-g) obtained comparing the reference segmentation with segmentations given by erosion or dilatation for each group of volunteers and patients at peak systole. * indicates statistically significant differences ($p < 0.05$).

3.3.4. Local Hemodynamics

Figure 3-5 shows the bullseye plots of the hemodynamic parameters for volunteers and DCM patients at peak systole. More areas with statistical differences were observed mainly in velocity magnitude and kinetic energy, particularly in anteroseptal, inferior, inferolateral basal, anterior, inferoseptal, inferior, inferolateral mid-cavity, anterior, septal, and lateral apical segments (all p-values < 0.033). Additionally, vorticity magnitude showed statistical differences in anteroseptal basal ($p = 0.045$) and inferoseptal mid-cavity ($p = 0.046$) segments. Energy loss showed statistical differences in inferoseptal ($p = 0.029$) and inferolateral ($p = 0.046$) mid-cavity segments and in anterior ($p = 0.023$), septal ($p = 0.070$), and inferior ($p = 0.077$) apical segments. Helicity density and viscous dissipation did not show statistical differences in any parcellation.

Figure B.10 shows the comparison at the e-wave. Similar to peak systole, statistical differences were in velocity magnitude and kinetic energy. Statistical differences in viscous dissipation and energy loss were found in inferolateral basal and septal, anterior, and lateral apical segments (all p-values < 0.049). Vorticity magnitude showed statistical differences in anteroseptal basal (p = 0.049) and septal (p = 0.039) and lateral (p = 0.039) apical segments. Helicity density did not show statistical differences in any parcellation of the LV.

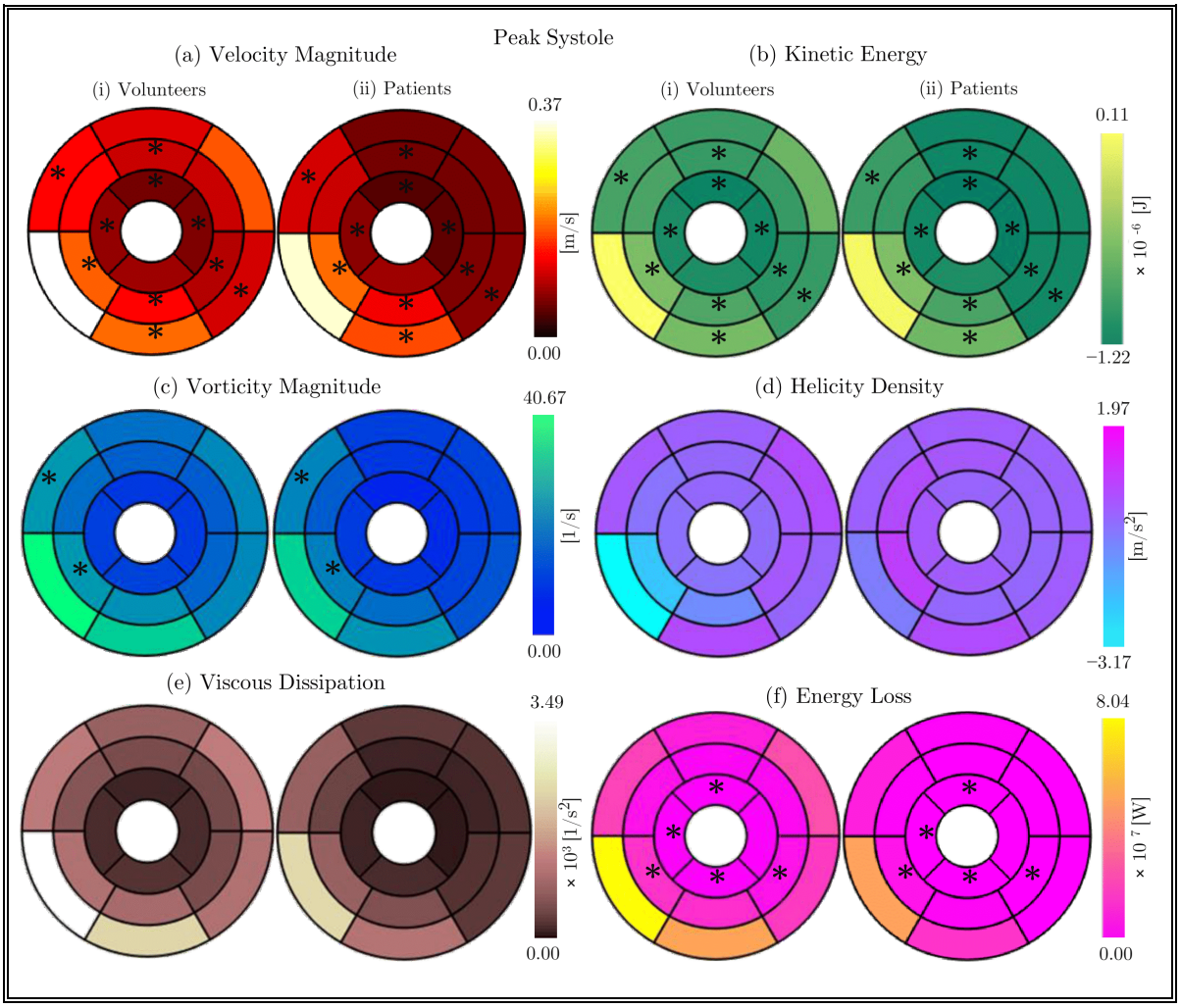

Figure 3-5. Bullseye plots of mean hemodynamic parameters (a–f) across 16 segments for volunteers (i) and patients (ii) at the peak systole. * indicates statistically significant differences (p < 0.05).

We did not find statistical differences in any segment at end-diastole.

The mean values of local hemodynamic parameters for both groups under study at peak systole, e-wave, and end-diastole are available in Tables A.2–A.4, respectively.

3.4. Discussion

We developed a method to characterize the left intraventricular hemodynamics in the LV from 4D Flow MRI using a finite element method, applied in a cohort of DCM patients. This approach estimates vorticity, helicity density, viscous dissipation, energy loss, and kinetic energy fields from a single segmentation. The hemodynamics results indicated that velocity magnitude, vorticity magnitude, viscous dissipation, energy loss, and kinetic energy revealed statistical differences between volunteers and patients, particularly at peak systole and e-wave.

Some of the parameters reported in this study have been reported before. Nevertheless, those parameters have been obtained from different methodologies in different cohorts of patients. In our case, we calculated several parameters from a single segmentation at once from only one 4D Flow dataset, which is difficult to determine with other methods. Some other methods are based on a finite difference approach, as in Lorenz et al. (Lorenz *et al.,* 2014). However, it is well known that finite difference cannot effectively handle complex geometries, such as those found in the cardiovascular system. Neither can impose boundary conditions on irregular surfaces directly but they are both sensitive to noise. Fouras *et al.* showed that this approach suffers from a loss of accuracy in estimating hemodynamic parameters due to the omission of out-of-plane velocity information (Fouras *et al.,* 1998). On the other hand, Sotelo *et al.* demonstrated the convergence and robustness of the finite element method in cardiovascular flow (Sotelo *et al.,* 2016) (Sotelo *et al.,* 2018). Further, they also showed that the finite element method is both stable and accurate in the presence of noise.

Although DCM mainly affects the systolic function, we evaluated the hemodynamic parameters at systole and diastole, as several papers have shown that

diastolic function is also affected by this disease. For instance, Friedberg *et al.* and Dragulescu *et al.* reported that diastolic wall-motion abnormalities are prevalent in pediatric DCM. Their presence is associated with diastolic ventricular dysfunction and adverse outcomes (Friedberg *et al.,* 2008) (Amorin *et al.,* 2017). Some papers have assessed diastolic function in DCM patients using 4D Flow data (Dragulescu *et al.*, 2013) (Eriksson *et al.,* 2013). They have described alterations in the flow components related to velocity, vorticity, and kinetic energy in a different cohort of patients, consistent with our results (Pedrizzetti *et al.*, 2014) (Zajac *et al.,* 2015) (Sotelo *et al.,* 2015) (Arvidsson *et al.,* 2016) (Sjöberg *et al.,* 2017).

As we showed in this study, intraventricular flow in DCM patients was altered compared to healthy volunteers at diastole. In addition, it is interesting to observe that, while end-diastolic volume was significantly larger in patients than healthy subjects, the maximum hemodynamic values for e-wave and end-diastole were smaller in patients than in volunteers. For instance, we found that in the normal LV, kinetic energy values were high. The highest kinetic energy values were observed during early diastole and regionally distributed near basal LV regions. In contrast, early- and end-diastole kinetic energy was lower than normal in a heterogeneous group of DCM patients and decreased with the LV volume. As we found in our results, this decrease of kinetic energy throughout diastole is associated with viscous dissipation and energy loss. That agrees with a previous study, where comparisons of inflow characteristics in healthy subjects and DCM patients showed more differences at e-wave between the two groups (Friedberg *et al.,* 2008) (Dragulescu v 2013) (Eriksson *et al.,* 2013) (Foell *et al.,* 2013) (Eriksson *et al.,* 2016) (Stoll *et al.,* 2019). These ventricular diastolic function aspects can be influenced by dynamic load and contractility; these may vary within the spectrum of normal conditions. Furthermore, large ventricles lead to weak suction pumps and have high wall tension, which has been previously suggested to cause energy waste and alter vortex ring dynamics (Pedrizzetti *et al.,* 2014) (Arvidsson *et al.,* 2016). These results indicate that, despite the complex nature of ventricular finding factors, clinically useful information regarding left ventricular diastolic function is

associated with distinct mitral flow velocity patterns. Therefore, these alterations of blood flow may be a factor in developing systolic and diastolic dysfunctions.

While eight patients showed significantly impaired systolic function at CMR's time, five showed a complete response to treatment. Despite a nearly normalized LV ejection fraction, it showed similar hemodynamic values to non-responders DCM patients that were markedly different from volunteers. These results suggest a significant increase in the ratio of outflow to inflow during systole in responders DCM patients, but the volumes were significantly smaller. Therefore, LV ejection fraction cannot reflect subtle ventricular dysfunction, which potentially can be better assessed using flow-based parameters because

of the sensitivity to abnormal pumping function (Friedberg *et al.,* 2008). Therefore, the problem of using LV ejection fraction as the pivotal risk marker for DCM patients is that this single parameter does not recapitulate the complexity of the disease.

The location and extent of the changes in intraventricular blood flow, for example, the depth (base to apex) of the vorticity changes or the spread of impaired flow through the ventricular cavity, can potentially be a sensitive marker of the severity of diseases or the progress of the treatment but are hard to quantify because of the 3D nature of the flow. We proposed to use the bullseye plots to depict this data. These plots allow us to display the most important regional differences and extend flow changes in a familiar way to many clinicians. These results could facilitate homogeneity among 4D Flow quantifiable analysis for clinical researchers and clinicians.

The sensitivity study showed a significant relative error, particularly in helicity density, when the differences in the segmentations were greater than 1 pixel in dilation and erosion cases. We performed this sensitivity study even under the pixel resolution of the 4D Flow data. In each pixel, there were four or five elements from the mesh, whose flow values were interpolated from neighborhood pixels. When the segmentation error was lower or equal to 1 pixel, the maximum mean relative error was less than 10% in most hemodynamic parameters studied. Previous research has shown that DCM patients have a lower mean value of velocity magnitude than

healthy volunteers (Pedrizzetti *et al.,* 2014) (Zajac *et al.,* 2015) (Sotelo *et al.,* 2015) (Arvidsson *et al.,* 2016) (Sjöberg *et al.,* 2017). These results were considered when the segmentation contour fell inside the LV blood pool. In general, we also observed that lower errors were obtained for almost all hemodynamic parameters when the segmentation underestimated the LV volumes.

Inter-observer and intra-observer assessments showed excellent reproducibility of the results with negligible mean differences and small limits of an agreement at peak systole, e-wave, and end-diastole for all the parameters assessed. It is important to note that the high intra- e inter-observer variability was obtained because we performed an automatic segmentation process using the software Segment. Therefore, the difference in segmentations was minimal, as previously reported by Tufvesson *et al.* (Tufversson *et al.,* 2015). The automated process corrections were also minimal, which led to a high intra- and interobserver variability. On the other hand, the sensitivity study was performed by modifying a reference segmentation in the entire contour by applying erosion or dilatation. This result implies a more significant volume difference concerning the reference, and, as a result, high sensitivity to the segmentation was obtained.

The limited size of this proof-of-concept study did not allow us to investigate the prognostic impact, but this will be our aim in future research. Nevertheless, in this small cohort of patients, we have shown that the velocity, vorticity, kinetic energy, viscous dissipation, and energy loss revealed statistical differences between volunteers and patients. This finding could be relevant to assess changes in a longitudinal study or to study the response to a particular therapy. Additionally, 4D Flow derived parameters showed that, in responding DCM patients, hemodynamics parameters were low, even though they had a recovered ejection fraction. Nevertheless, hierarchical cluster analysis underlined that a moderate correlation may exist between ejection fraction and 4D Flow-based metrics, which needs to be studied further. A clinical study involving more DCM patients should be performed in order to corroborate a prognostic impact and hence a clinical relevance of 4D Flow analysis in monitoring DCM patients.

The segmentation of the data need was performed over the multi-slice b-SSFP. Additionally, multi-slice b-SSFP and 4D Flow images need to be registered before analyzing the 4D Flow data. Ideally, the segmentation would be made directly on the 4D Flow data. However, the contrast between the blood pool and myocardium in our 4D Flow data was insufficient to perform accurate segmentation. New sequence developments will likely improve contrast in 4D Flow acquisitions, potentially allowing direct segmentation from the 4D Flow data.

3.5. Conclusions

This study describes a methodology for quantitative evaluation of intraventricular hemodynamics using a single segmentation from a 4D Flow dataset. We demonstrate that velocity, vorticity, viscous dissipation, energy loss, and kinetic energy can characterize changes in intraventricular flow in DCM patients compared to healthy volunteers. Further studies should focus on the impact of different treatments of DCM patients on those parameters. Our evidence shows that, although ejection fraction may be recovered, the hemodynamic parameters remain low.

3.6. Acknowledgments

This work has been funded by projects PIA-ACT 192064 and the Millennium Nucleus on Cardiovascular Magnetic Resonance NCN17_129 of the Millennium Science Initiative, both of the National Agency for Research and Development, ANID. The authors also give thanks to Fondecyt project 1181057, also by ANID. Franco P. gives thanks to ANID PCHA/Doctorado-Nacional/2018- 21180391. Sotelo J. gives thanks to CONICYT FONDECYT Postdoctorado 2017 #3170737 and ANIDFONDECYT de Iniciación en Investigación #11200481.

4. THIRD ARTICLE: IDENTIFICATION OF HEMODYNAMIC BIOMARKERS FOR BICUSPID AORTIC VALVE INDUCED AORTIC DILATION USING MACHINE LEARNING

4.1. Introduction

Bicuspid aortic valve (BAV) is the most common congenital cardiac defect (Kang *et al.,* 2013) with a prevalence of 1-2% in the general population (Siu *et al.,* 2010). Clinical manifestations of BAV are aortic dilation, aneurysm, and dissection, which typically develop in the ascending aorta (AAo) (Evangelista *et al.,* 2018) (Girdauskas *et al.,* 2018) and often extend to the aortic arch (AArch) (Dux-Santoy *et al.,* 2019). Current clinical management of aneurysms in BAV patients relies on quantifying aortic diameter, but its predictive capacity is limited (Pape *et al.,* 2007). Therefore, there is a need for new biomarkers to refine disease monitoring and improve patient risk stratification.

The most common BAV leaflet fusion phenotype involves the right-left cusps and right-non-coronary cups, with a prevalence of around 80% and 17%, respectively (Schaefer *et al.,* 2008) (Evangelista *et al.,* 2018). Recent studies have demonstrated that BAVs cause altered blood flow hemodynamic in the AAo, which implies increased flow asymmetry, helicity, and wall shear stress (WSS) overloads on the aortic wall (Liu *et al.,* 2018). The WSS abnormalities are associated with histological and proteolytic of the aortic wall damage demonstrating a role for hemodynamics in the etiology of BAV aortopathy (Bissell *et al.,* 2013) (Atkins *et al.,* 2014) (Allen *et al.,* 2015) (Pasipoularides *et al.,* 2019) (Soulat *et al.,* 2021) (Guala *et al.,* 2021). Nevertheless, increased WSS is not a unique feature in BAV disease. Aortic valve stenosis can also subject the aortic wall to high WSS (Boudoulas *et al.,* 2015). Furthermore, many other hemodynamic parameters beyond WSS can be used to study aortic blood flow in BAV patients, making it difficult to conclude which has more association to BAV aortopathy, especially with traditional statistical assessment.

Artificial intelligence (AI) methods have gained increased attention in cardiology and cardiovascular imaging (Dey *et al.,* 2019). For instance, in cardiac magnetic resonance (CMR), AI methods have been applied to segment left and right ventricles and aorta to enable automatic cardiovascular volume assessment and enhance reproducibility in clinical assessments (Avendi *et al.,* 2017) (Tan *et al.,* 2018) (Tao *et al.,* 2019) (Campello *et al.,* 2021) (Aviles *et al.,* 2021). Pattern recognition, i.e., the automatic discovery of regularities in data through machine learning (ML), has been recently applied to genomic data to stratify BAV patients, identify distinct patterns of aortopathy, and characterize their association with valve morphology (Ambale-Venkatesh *et al.,* 2017) (Wonjnarski *et al.,* 2018) (Cantor *et al.,* 2021). The absence of clear associations between several hemodynamics parameters has limited the use of a few uncorrelated parameters to characterize BAV pathology (Girdauskas *et al.,* 2011).

Assessing the impact of several hemodynamic parameters in BAV dilation is difficult due to extensive data. Different methods of feature selection (FS) can be used to reduce dimensionality and redundancy of data, which allows determining which features discriminate best between two or more classes. Given the increasing capacity to extract a large amount of data from images, FS methods have become essential to achieve effective classifications. FS selection method is mainly used to provide accurate classifier models for classification tasks (Mery 2015).

This study aimed to identify hemodynamic biomarkers for BAV patients and their relationships with aortic dilation. For that purpose, we analyzed and extracted multiple correlation patterns of hemodynamic parameters, finding which showed high collinearity between them, which allows us to reduce their size to few variables. And finally, we applied machine learning algorithms to discriminate between healthy volunteers (HV) and BAV patients with and without ascending aorta dilation.

4.2. Methods

4.2.1. Study Population

Data obtained from a previous prospective study (Dux-Santoy et al., 2019) was used in this work. We included sixty-seven BAV patients with a fusion of right and left coronary cusps (67.16 %) or right and noncoronary cusps, AAo diameters were less or equal than 45 mm, and had no severe aortic valve disease (aortic regurgitation ≤ 3, maximum aortic valve velocity < 3 m/s by echocardiography). Patients were recruited at the Hospital Universitari Vall d'Hebron (Barcelona, Spain). Other inclusion criteria include age > 18 years; without any congenital heart disease, including aortic coarctation; no connective tissue disorders; no previous aortic surgery or aortic valve replacement; and no contraindication for CMR. Forty-eight healthy volunteers (HV) matched for age, sex, and body surface area (BSA) were also included. The local ethics committee approved the study, and informed consent was obtained from all participants.

4.2.2. Cardiovascular Magnetic Resonance Protocol

Multi-slice two-dimensional balanced steady-state free precession (b-SSFP) and 4D Flow MRI using Vastly undersampled Isotropic Projection Reconstruction (VIPR) (Gu *et al.,* 2005) (Johnson *et al.,* 2010) were acquired in a clinical GE 1.5T scanner (Signa, General Electric Healthcare, Waukesha, Wisconsin, USA). MRI datasets of the thoracic aorta were acquired with retrospective ECG cardiac gating with free breathing and without administration of an endovenous contrast agent. Acquisitions parameters were: velocity encoding of (VENC) 200 cm/s, a field of view of 400×400×400 mm^3, scan matrix of 160×160×160 (voxel size of 2.5×2.5×2.5 mm^3), flip angle of 8°, repetition time between 4.2-6.4 ms, and echo time between 1.9-3.7 ms. The data were reconstructed offline with corrections for background phase, eddy currents, and trajectory errors (Johnson et al., 2012)

according to each patient's nominal temporal resolution, which was ranged between 21-36 ms.

4.2.3. Aortic Diameters and Valve Morphotype

BAV morphotype and aortic diameters were assessed using cine MR images (Rodríguez-Palomares *et al.,* 2018). The three aortic root cusp-to-commissure diameters were measured using double-oblique cine images at the aortic root level at end-diastole, and the maximum value was retained for the analysis. AAo diameter was measured at the level of the pulmonary artery bifurcation at the end-diastolic phase. To determine the existence of aortic root or ascending dilation, aortic diameters were adjusted with a logarithm transformation to calculate the z-score for both sinuses (zSoV) and AAo (zAAo) accounting for sex, age, and BSA as described by Campens *et al.* (Campens *et al.,* 2014). A z-core cut-off value was used to define the aortic dilation of two standard estimate errors. According to Della Corte's classification, patients were categorized concerning the aorta segment predominantly or exclusively involved in dilation (Della Corte *et al.,* 2 2014). Therefore, patients were classified as non-dilated (NON-DIL BAV) ($zSoV \leq 2$ and $zAAo \leq 2$) and dilated (DIL BAV) ($zAAo > 2$ and $zAAo > zSoV$) ascending aorta. Patients with only aortic root dilation were excluded from the study.

4.2.4. 3D Quantification of Hemodynamics Parameters

A detailed description of methods used to quantify hemodynamics descriptors is described in previous publications (Sotelo *et al.,* 2016) (Sotelo *et al.,* 2018) (Dux-Santoy *et al.,* 2020). We briefly explain the methods next. The quantifications were done through an in-house MATLAB toolbox (The MathWorks Inc., Natick, Massachusetts, USA) [37]. The thoracic aorta was semiautomatically segmented, and a segmentation mask was used to generate a tetrahedral mesh (Fang et al., 2009). Afterward, we used cubic interpolation to compute the velocity vector at each mesh node. Thereafter, a finite-element least-squares projection method was

used to obtain several continuous 3D maps, including eccentricity, velocity, forward velocity, backward velocity, velocity angle, regurgitation fraction, WSS, WSS axial, WSS circumferential, oscillatory shear index (OSI), vorticity, axial vorticity, axial circulation, helicity density, viscous dissipation, energy loss, and kinetic energy were generated. Finally, eight different regions were analyzed in the thoracic aorta, four for each segment in the AAo and AArch. In each region, we analyzed the mean value for each hemodynamic parameter at an averaged peak systolic data, corresponding to the average at one time-frame before peak systole, one at peak systole, and one time-frame after to reduce noise in the data, except for regurgitation fraction and oscillatory shear index (OSI). These parameters were calculated using information along the entire cardiac cycle (Rodríguez-Palomares *et al.*, 2018).

4.2.5. Hemodynamic Parameters Analysis: Machine Learning Algorithm

A machine learning model was designed to select hemodynamic parameters that differentiate among three classes: HV, NON-DIL BAV, and DIL BAV. The imaging process pipelines extract seventeen hemodynamic features in each of the two segments of the aorta. Then, the classifiers assigned the extracted features from 4D-flow CMR to one of these classes.

To build the classifiers, we firstly reduced the dimensionality of the data. For this purpose, hemodynamic parameters were selected using sequential forward selection (SFS) and principal component analysis (PCA). We chose five features using SFS with Fisher objective function and exhaustive search, as shown in Supplementary Table C.1. We used singular value decomposition to perform PCA. PCA generates a set of new features; each being a linear transformation of the original elements. We decompose the data matrix X of $n \times p$ size, where n is the number of subjects and p the number of features, using singular value decomposition, i.e.

$$\mathbf{X} = \mathbf{USV}^{\mathbf{T}} \tag{4.1}$$

where **U** is a unitary matrix, **S** is the diagonal matrix of singular values s_i and **V** the right singular vector. Therefore, we can write the covariance matrix as

$$\mathbf{C} = \frac{1}{n}\mathbf{X}\mathbf{X}^{\mathrm{T}} = \frac{1}{(n-1)}\mathbf{V}\mathbf{S}\mathbf{U}^{\mathrm{T}}\mathbf{U}\mathbf{S}\mathbf{V}^{\mathrm{T}} = \mathbf{V}\frac{\mathbf{S}^2}{(n-1)}\mathbf{V}^{T} \tag{4.2}$$

Meaning that the right singular vector **V** are principal directions and that singular values are related to the eigenvalues of covariance matrix **C**, via $\lambda_i = s_i^2/(n-1)$. The principal components are defined by $\mathbf{V} = \mathbf{U}\mathbf{S}\mathbf{V}^{\mathrm{T}}\mathbf{V} = \mathbf{U}\mathbf{S}$. We selected only the dominant eigenvectors, representing 95% of the data. Then, we took each vector's norm in the new space and leveraged scores. Finally, we obtained the indices of the vectors with the largest leverage scores (see Supplementary Table S2) (Wall *et al.*, 2003).

After features selection, we tested different classifiers. We used the following classifiers: k-nearest neighbors (KNN) with 5, 7, 9 neighbors, linear discriminant analysis (LDA), quadratic discriminant analysis (QDA), minimum distance, Mahalanobis distance, support vector machine (SVM) using both the linear and radial basis function kernel (RBF), neural network, and random forest. We used a neural network with multilayer perceptron architecture with one hidden layer that contains 15 nodes. In our network, the activation function in the output layer was a "softmax" unit. Of note, in our experiments, this configuration obtained the highest accuracy. We did not use individual decision trees to develop the random forest because they tend to overfit. To reduce the effects of overfitting and improve generalization, we used bootstrap-aggregated decision trees to combine the results of many decision trees. Therefore, to maximize the variance explanation of the dependent variable, a variable is selected at each spit/node. In each round of training, 1000 decision trees were generated with a maximum allowed tree depth of five.

We used stratified cross-validation to evaluate the performance of the classification. The holdout method was used to divide the data into ten folds (90% of the data were used for training and 10% for testing) because it has become the

standard method in practical terms (Sotelo 2021). To evaluate the stability of the classifier, we repeated this experiment ten times, interchanging training and testing data. For each time, the performance defined as the rate of samples correctly classified was computed as η_i, for $_i$ = 1,…,10. A confusion matrix was constructed based on prediction results in each training and validation sample, and the corresponding accuracy, precision, sensitivity, and specificity were calculated as the mean of the ten percentages of the true classifications that are tabulated in each case: $\eta = (\eta_1 + \ldots + \eta_{10})/10$. In addition, the mean ROC area under the curve (AUC) and 95% confidence interval were computed.

To validate both the algorithms and hemodynamic features, the performance of different pattern recognition classifiers was measured to quantify the amount of variance between the three classes of subjects. High classification accuracy shows that the proposed system of algorithms and features can be used to differentiate among the groups.

On the other hand, we used t-Distributed Stochastic Neighbor Embedding (t-SNE) to visualize high-dimensional datasets (classification with all features, SFS, and PCA features selected) (van der Maaten *et al.,* 2008).

The algorithms were implemented in MATLAB using Balu (Mery 2011) and the Statistics and Machine Learning MATLAB Toolbox.

4.2.6. Hemodynamic Parameters Analysis: Hierarchical Clustering

In order to extract multiple correlation patterns from hemodynamic parameters and identify highly correlated data, we used the correlation matrix-based hierarchical clustering method. This method grants a dataset into a multilevel cluster tree or dendrogram. The distance (dissimilarity) is defined as one minus Pearson's correlation coefficient. It expressed that if two hemodynamic parameters had a shorter distance, they are similar, i.e., the distance is 0, the correlation coefficient is 1. The variable that quantifies an effective representation of the pattern dissimilarities in the dendrogram is the cophenetic correlation (the correlation between original and cophenetic distances). We used the average

linkage method to calculate the cophenetic distance to get an average inter-cluster distance that allows higher cophenetic correlations. It provided the dendrogram illustrating the correlation matrix's hierarchical structure and derived the final cluster. At last, based on inconsistency coefficients, we broke down the dendrogram obtaining clusters visually differentiated by colors (Gu *et al.,* 2010) (Ciaburro *et al.,* 2017).

4.2.7. Statistical Analysis

The software GraphPad Prism version 6.0.1 (GraphPad Software Inc., San Diego, California, USA) was used for statistical analysis. In population demographics, normal distribution was evaluated using the Shapiro-Wilk test. Student *t-test* and Mann-Whitney *U* test were applied to find differences between groups for continuous parameters with normal and non-normal distributions, respectively. For categorical variables we applied $\chi 2$ test. A p-value < 0.05 was considered statistically significant.

4.3. Results

4.3.1. Demographics

Demographical and clinical data are described in Table 4.1. HV and BAV patients were matched in terms of age, sex, and body surface area. The BAV patients presented higher diameter and Z-score than HV at both the aortic root and AAo. Seventy-three percent of BAV patients had AAo dilation. We did not find any differences other than aortic diameters, and Z scores between patients with and without aortic dilation.

Table 4.1. Demographical and clinical data for the healthy volunteers (HV) and BAV patients. Quantitative data are expressed as the mean ± SD. BSA, body surface area; DBP, diastolic blood pressure; EAo, aortic stenosis; SBP, systolic

blood pressure; IAo, aortic insufficiency; and SoV, sinus of Valsalva. * indicates statistically significant differences ($p < 0.05$).

				BAV Dilation Group		
	HV	**BAV**	**p-value**	**NON-DIL**	**DIL**	**p-value**
N	48	67		18	49	
Age (year)	48.71 ± 12.57	47.74 ± 15.06	0.998	46.68 ± 14.35	48.28 ± 15.44	0.698
Sex (female:male)	23:25	31:44	0.514	5:13	24:25	0.121
Weight (kg)	70.81 ± 10.53	72.18 ± 13.25	0.587	74.72 ± 13.05	72.42 ± 13.59	0.534
Height (cm)	171.23 ± 7.82	169.45 ± 10.85	0.364	172.33 ± 8.60	168.69 ± 11.33	0.221
BSA (m2)	1.83 ± 0.16	1.83 ± 0.21	0.995	1.88 ± 0.20	1.82 ± 0.22	0.349
IAo (%)			…			0.246
None	…	73.33		88.89	75.51	
Mild	…	10.67		5.56	12.25	
Moderate	…	16		5.56	12.24	
EAo (%)						0.359
None	…	89.55		94.44	87.76	
Mild	…	5.97		5.56	6.12	
Moderate	…	4.48			6.12	
SBP (mmHg)	130.15 ± 18.85	134.88 ± 17.55	0.114	133.78 ± 18.12	135.17 ± 17.05	0.773
DBP (mmHg)	73.41 ± 10.09	76.43 ± 8.73	0.128	77.39 ± 6.99	77.33 ± 9.03	0.981
Diameter SoV (mm)	30.32 ± 3.92	35.91 ± 4.69	< 0.001*	33.28 ±3.74	36.08 ± 4.41	0.019*
Diameter AAo (mm)	27.89 ± 3.71	39.37 ± 6.74	< 0.001*	32.72 ± 4.17	42.82 ± 5.19	< 0.001*
Z score SoV	-0.25 ± 1.18	1.30 ± 1.30	< 0.001*	0.27 ± 0.82	1.33 ± 1.05	< 0.001*
Z score AAo	-0.14 ± 0.91	2.89 ± 1.52	< 0.001*	0.98 ± 1.07	3.71 ± 0.98	< 0.001*

4.3.2. Hemodynamic Biomarkers Selection with SFS and PCA

From the seventeen hemodynamic features obtained, the five features that best differentiated the three classes (HV, NON-DIL BAV, and DIL BAV) were selected using both SFS and PCA by eliminating highly correlated or constant features that maximized accuracy (see Supplementary Table C.1).

Regarding SFS, figure 4-1.a shows the maximum separability obtained by each of the seventeen hemodynamic features as assessed in both aortic regions. The five variables presenting with the lowest separability and resulting in the higher accuracy once used in the different classifiers (Supplementary Figure C.1) were retained. They correspond to velocity angle, forward velocity, vorticity, backward velocity in AAo, and helicity density in AArch. Figure 4-1.b shows the 3D feature space obtained using three features (velocity angle in AAo, forward velocity in AAo, and helicity density in AArch) for visualization purposes, showing good separability among classes. Figure 4-2. a. shows the two principal components of PCA. Dimension 1 explains 45.21% variation in the data while Dimension 2 explains 23.73% variation. Together they explain 68.94% of the variation.

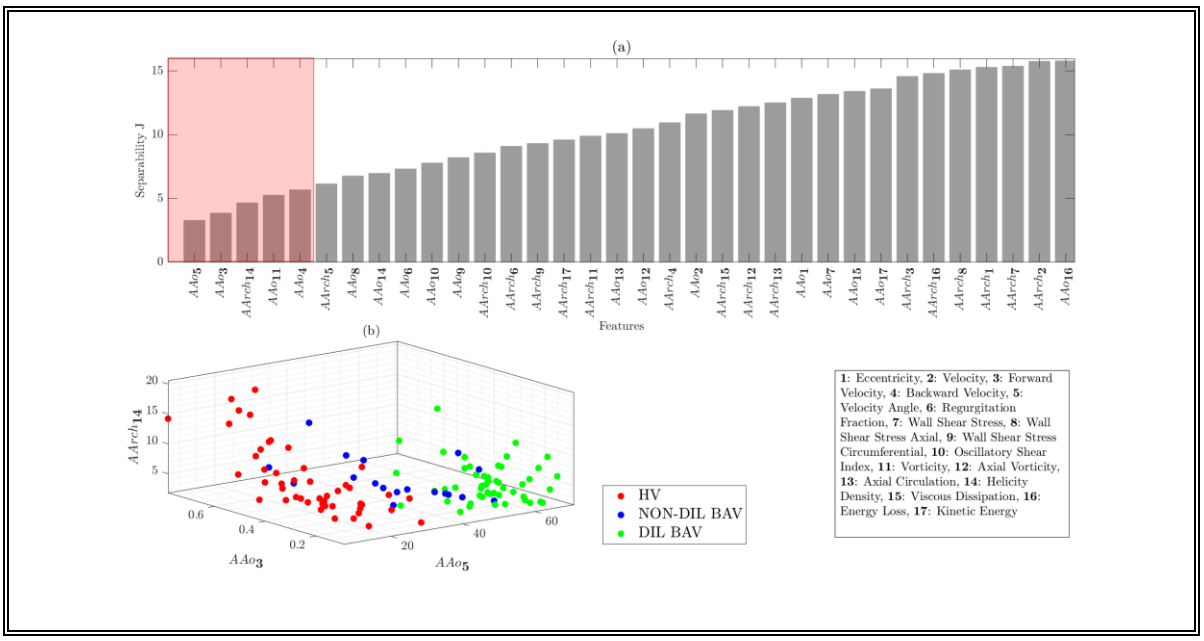

Figure 4-1. (a): Feature selection using sequential forward selection (SFS). There are five selected features, and they correspond to velocity angle in AAo, forward velocity in AAo, helicity density in AArch, vorticity in AAo, and backward velocity in AAo (red rectangle). (b): Feature Space in 3D.

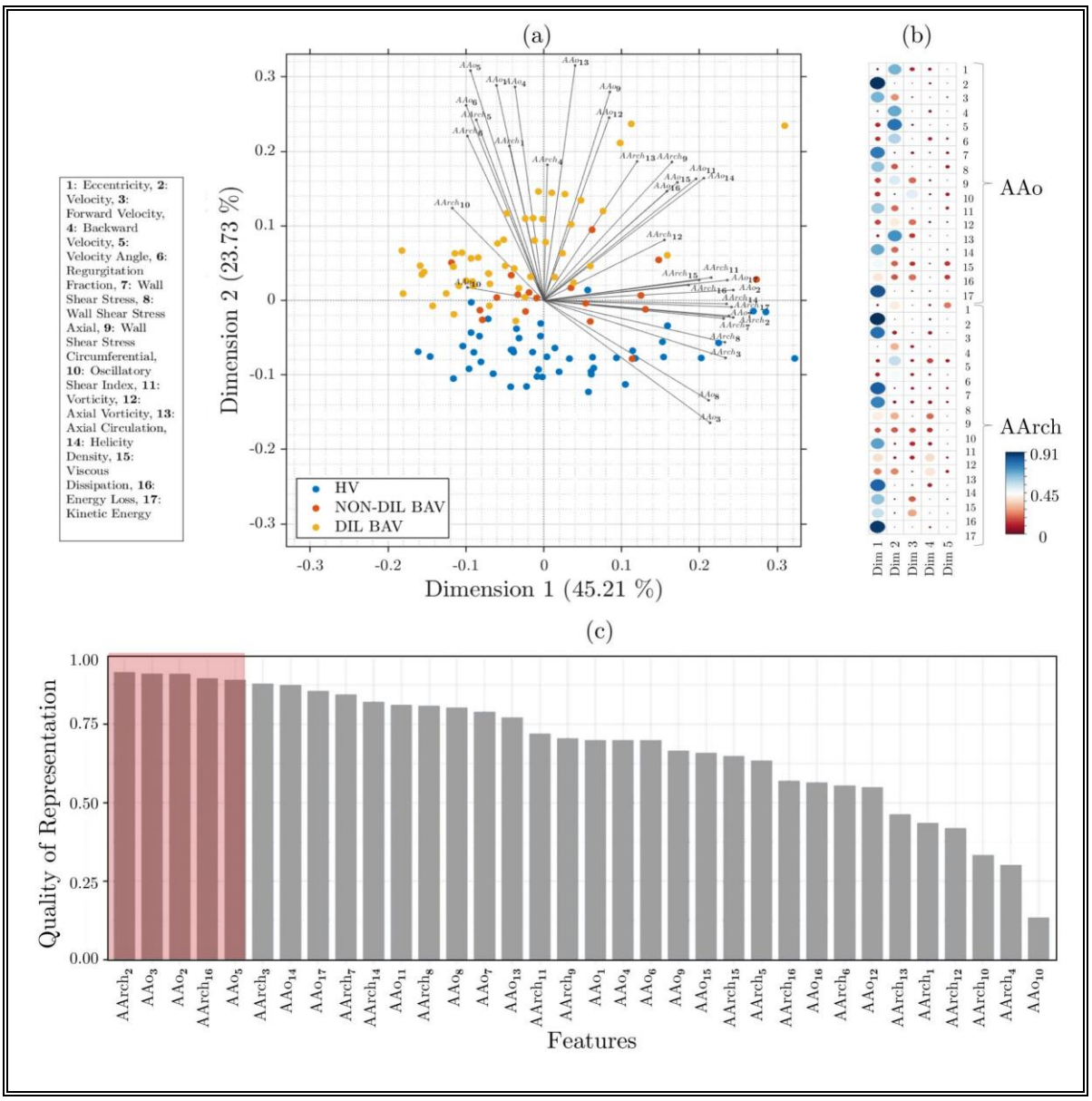

Figure 4-2. (a) The two principal components PCA. The distance between variables and the origin measures the quality of the variables on the factor map. Variables that are away from the origin are well represented on the factor map. (b) PCA correlation circle that represented the quality of representation of the features on factor map. The better its representation on the factor map, is the variable closer to the circle's center. This means that variables located closer than to the center of the plot are less important (c) Bar graph of quality of representation. There are five selected features, and they correspond to velocity in AArch, forward velocity in

AAo, velocity in AAo, energy loss in AArch, and velocity angle in AAo (red rectangle).

Regarding PCA, figure 4-2.b shows PCA correlation circle that represented the quality of representation of the features on a factor map. The better its representation on the factor map, is the variable closer to the circle's center. This means that variables located closer than to the center of the plot are less important. Finally, figure 4-2.c shows a bar graph of the quality of representation of the variables on factor maps on all the dimensions. The five top-performing features were forward velocity, velocity, velocity angle in AAo, and velocity and energy loss in AArch.

The computational time of the feature selection is short (approximate 0.05s) because we are dealing with a small number of features.

4.3.3. Classification Results

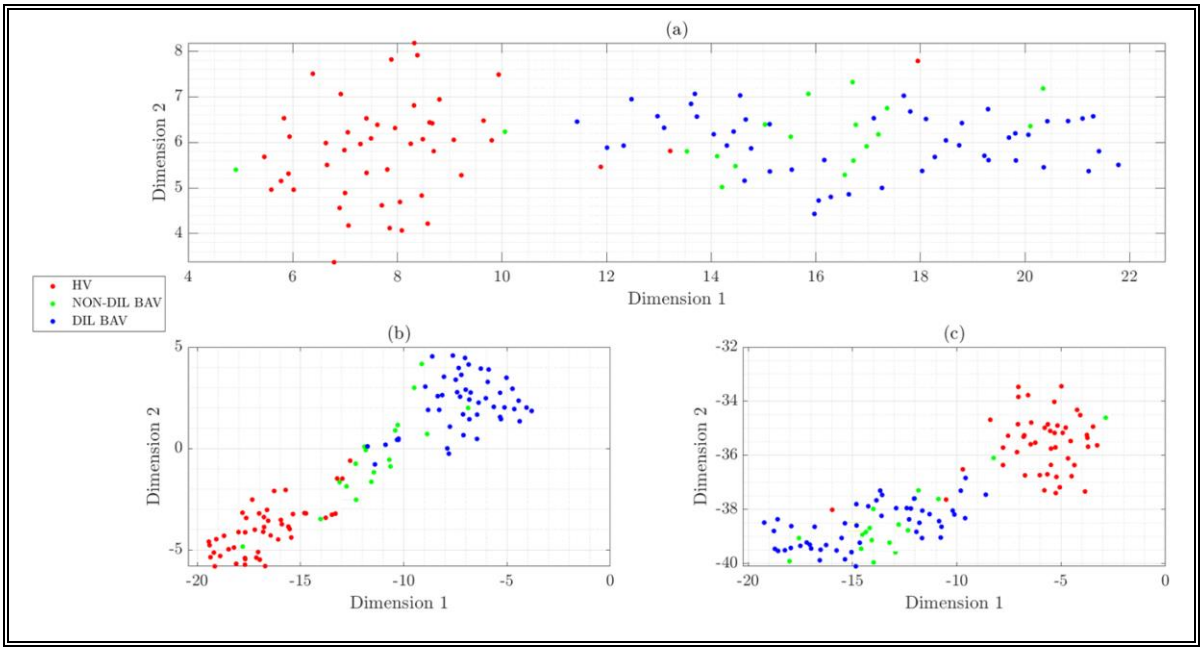

Figure 4-3. t-SNE: t-Distributed Stochastic Neighbor Embedding. (a) All features, five selected features by: (b) SFS, and (c) PCA. SFS and PCA results show a good separation of the groups. But PCA results show a lower distance between

groups, and more NON-DIL BAV subjects can be classified as DIL BAV compared to SFS results.

Table 4-2. Accuracy, precision, specificity, and sensitivity of different combinations of classifiers and all features, and five features selected by SFS and PCA. Each experiment was done using 10-fold cross-validation and repeated 10 times with a confidence interval of 95%. Bold type means statistically significant between the LDA and random forest for all features, SFS, and PCA, respectively (p-value < 0.05).

		LDA			Random Forest		
		All features	**SFS**	**PCA**	**All features**	**SFS**	**PCA**
HV class	**Precision (%)**	100.00 ± 0.00	100.00 ± 0.00	100 .00 ± 0.00	98.01 ± 1.19	99.49 ± 1.12	99.09 ± 1.30
	Specificity (%)	100.00 ± 0.00	100.00 ± 0.00	100.00 ± 0.00	99.05 ± 0.81	99.45 ± 0.84	100.00 ± 0.93
	Sensitivity (%)	94.17 ± 2.01	97.49 ± 6.51	97.48 ± 7.44	95.39 ± 1.51	94.22 ± 1.30	97.13 ± 1.62
NON-DIL BAV class	**Precision**	**69.38 ± 48.42**	**88.42 ± 32.40**	**63.49 ± 4.80**	**67.44 ± 9.45**	**78.02 ± 4.16**	**79.83 ± 9.80**
	Specificity (%)	**96.49 ± 5.51**	**98.41 ± 4.15**	**95.33 ± 7.51**	**94.32 ± 1.53**	**96.39 ± 0.65**	**96.43 ± 1.70**
	Sensitivity (%)	**80.36 ± 37.39**	**86.03 ± 22.05**	**78.42 ± 4.29**	**80.39 ± 6.41**	**99.40 ± 2.71**	**95.02 ± 9.57**
DIL BAV class	**Precision**	92.48 ± 7.02	93.01 ± 1.38	94.01 ± 1.00	95.50 ± 3.22	100.00 ± 0.75	99.03 ± 2.84
	Specificity (%)	95.32 ± 9.80	96.44 ± 7.12	96.43 ± 7.71	97.09 ± 2.19	100.00 ± 0.55	99.44 ± 2.09
	Sensitivity (%)	98.05 ± 6.33	99.59 ± 2.60	93.29 ± 1.10	93.44 ± 2.70	97.04 ± 1.32	95.32 ± 2.70
Accuracy (%)		93.86 ± 2.24	96.31 ± 1.76	91.05 ± 2.29	92.00 ± 1.80	96.00 ± 0.83	96.00 ± 2.70

Both simple (e.g., minimum distance and linear discriminant analysis) and more complex (e.g., SVM and neural networks) classifiers were tested using as input either all features or the five selected by SFS or PCA.

First, we used t-SNE as a tool to visualize high-dimensional data, as showing in Figure 4-3. Figure 4-3.a shows t-SNE with 34 features (17 parameters in each of the two segments). HV (red) and DIL BAV (blue) groups are separated, but few HV are

located close to the DIL BAV group. Nevertheless, the NON-DIL BAV group is not clearly separated from the DIL BAV group, and two NON-DIL BAV subjects are grouped in the HV class. Figure 4-3.b shows t-SNE with five selected features from SFS. Three groups are visualized; still, a few NON-DIL BAV subjects are grouped into HV and DIL BAV groups, respectively. Finally, Figure 4-3.c shows t-SNE with five selected features from PCA. Their behavior is similar to SFS's figure, but the distance in the three groups is lower, and more NON-DIL BAV subjects can be classified as DIL BAV compared to SFS results.

The best result was obtained by combining the five features selected by SFS in LDA, getting a 96.31 ± 1.76 % classification accuracy on HV, NON-DIL, and DIL BAV datasets. Other classifiers, as KNN and SVM-Linear, resulted in an accuracy of over 86% and 91.34% using SFS (Supplementary Table C.2). Using PCA as a feature selection, almost all classifiers were close to 90% accuracy.

The second-best result was obtained by combining the five hemodynamic features selected by SFS and random forest, with a 96.00 ± 0.83 % accuracy. Actually, there were not statistical differences between random forest and the LDA in precision, sensitivity, and specificity in DIL BAV and HV classes, but in NON-DIL BAV class (Table 4-2). The LDA had a better overall performance in the NON-DIL BAV class. However, it showed a larger variance than random forest for precision, sensitivity, and specificity in the cross-validation experiment. A diagram is showing in Supplementary Figure C.1. Each node contains the feature ID and threshold used for splitting. The position of some features, e.g., the relative distance from the root, in the random forest reflects the strength of association between diameter and hemodynamic parameters and BAV disease. For example, backward velocity in AAo is the optimal splitting feature. The optimal splitting feature found for the subsets is forward and backward velocity in AAo in the second layer. We can measure the association between aortic dilation and hemodynamic parameters in BAV disease by summarizing each feature's overall random forest based on these ranks. Moreover, we computed the predictor importance estimates from the random forest that grows trees using all variables extracted, as showed in Figure 4-4. Bar graph stores the increase in mean square error (MSE) averaged over all trees in

ensemble and divided by the standard deviation taken over the trees for each feature. The bars with the highest values contain the information of the most important features. This suggests that velocity angle in AAo is the most important predictor, followed by backward velocity, eccentricity, axial circulation, and regurgitation in AAo. The average processing time for feature selection and classification was 42s in a 2.3 GHz Intel i7 processor equipped with 8GB of RAM.

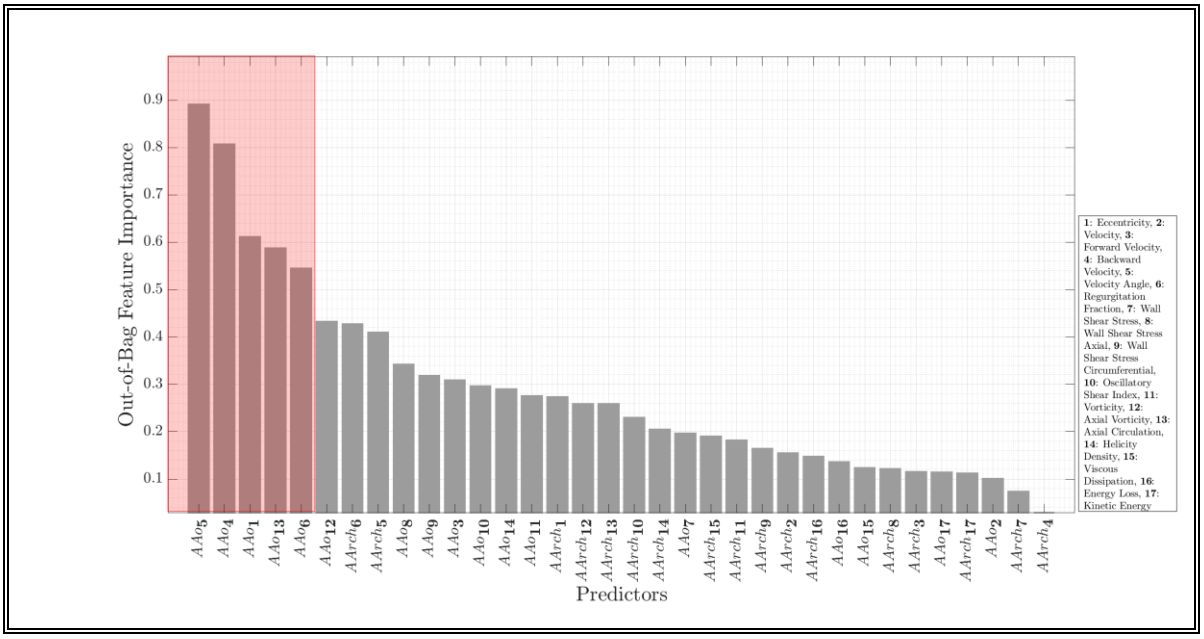

Figure 4-4. Predictors' importance estimation from random forest. The five top-performing features were: velocity angle, backward velocity, eccentricity, axial circulation, and regurgitation fraction in AAo (red rectangle).

Figure 4-5 shows ROC curves for both combinations with the best performance (LDA and random forest) using five features selected by SFS. We noted that the ROC curves for HV and DIL BAV classes are high similar, indicating that the methods can distinguish these classes. Nevertheless, the NON-DIL BAV class has lower results, and this class's imbalance may jeopardize the results. These classification methods achieved the best ROC AUC, sensitivity, specificity, precision across training and validation samples, and stratified cross-validations (Table 4-2).

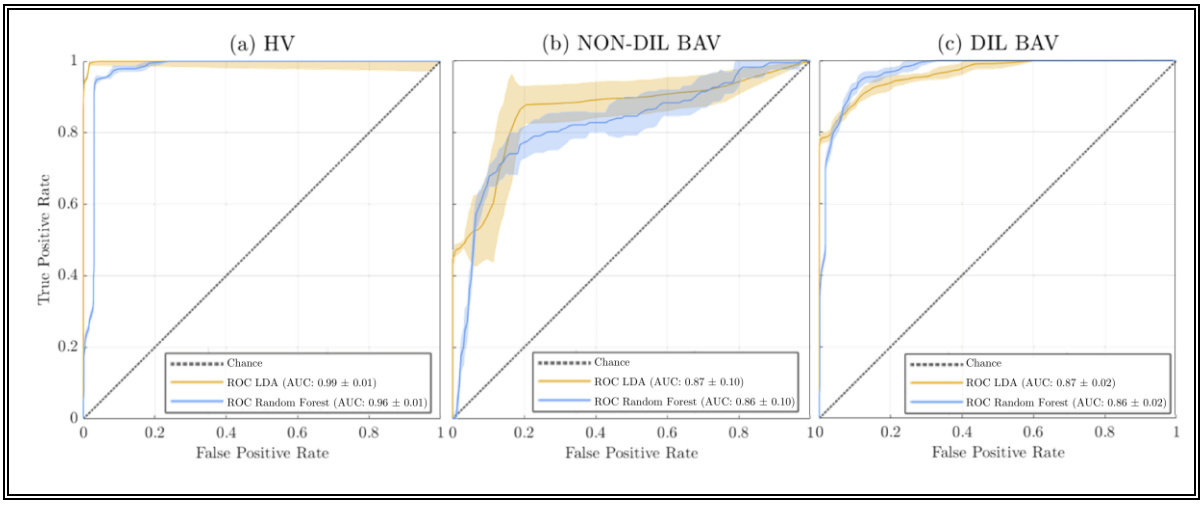

Figure 4-5. The ROC – curve for LDA and random forest with five features selected by SFS, displaying for the three classes in the mean ± SD. The NON-DIL BAV class has lower results in both classifiers, and this class's imbalance may jeopardize the results.

Additionally, we performed another experiment to classify only two classes (NON-DIL BAV and DIL BAV groups). We applied the methodology previously described and used hemodynamic features in AAo and AArch. Feature selection algorithm SFS found their five-top performing features were: velocity angle in AAo, regurgitation fraction in AArch, eccentricity in AAo, backward velocity in AAo, and oscillatory shear index in AAo. PCA's five best-performing features were: velocity in AArch, forward velocity in AArch, velocity in AAo, kinetic energy in AArch, and forward velocity in AAo. Using features selected by PCA, almost all classifiers get close to 86% accuracy. The best results were obtained by combining SFS-selected features using an LDA classifier with 96.18 ± 2.34% (see Supplementary Table C.3).

4.3.4. Hemodynamic Parameters Correlation

Figure 4-6.a shows the Pearson correlation matrix among all hemodynamic parameters for all regions and subjects. Supplementary Figure C.2 shows p-values obtained by the linear regression between all hemodynamic parameters. Several

parameters show good correlations (e.g., eccentricity and WSS in AAo), which indicate that some hemodynamic parameters are highly correlated and can be divided into clusters.

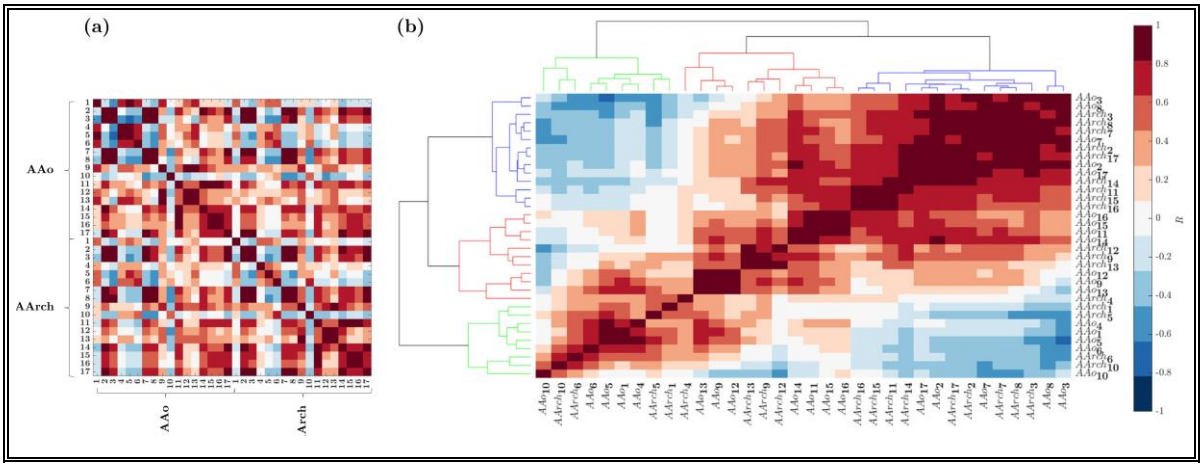

Figure 4-6. (a) Correlation matrix obtained by the linear regression, (b) dendrogram and hierarchical clustering result based on average linkage method, for all hemodynamic parameters of HV and BAV patients, in AAo and AArch regions.

A total of three clusters were identified as shown in Figure 4-6.b All three clusters combine at a much higher dendrogram distance and can be treated as individual groups for analysis. Cluster 1 (green): OSI, regurgitation fraction, velocity angle, and eccentricity in all regions; and backward velocity in AAo. Cluster 2 (red): axial circulation, WSS circumferential, and axial vorticity in all regions; backward velocity in AArch; and helicity density, vorticity, viscous dissipation, and energy loss in AAo. Finally, cluster 3 (blue): kinetic energy, velocity, WSS, WSS axial, and forward velocity in all regions; and energy loss, viscous dissipation, vorticity, and helicity density in AArch. This analysis shows high collinearity between the variables, which would allow us to reduce their size to a few variables.

According to hierarchical cluster analysis, we determined the clustering corresponding to each feature selected by SFS and PCA. SFS: cluster 1(green): velocity angle and backward velocity in AAo, cluster 2 (red): vorticity in AAo; and

cluster 3 (blue): forward velocity and helicity density in AAo and Aarch, respectively. PCA: cluster 1(green): velocity angle in AAo, cluster 2 (red): velocity in AAo, and cluster 3 (blue): forward velocity in AAo, energy loss, and velocity in AArch. Hence, we can assume that features by SFS have a better performance than those selected by PCA because it has a wide representation of each clustering.

Since most parameters were selected from the AAo, we repeated the methodology previously described, by selecting only three features from SFS and PCA in the AAo, by eliminating highly correlated or constant features that maximized accuracy. Each classification experiment is shown in Supplementary Table C.4 and C.5. The best result was obtained with the QDA classifier using three features selected by SFS: cluster 1 (green): velocity angle, cluster 2 (red): vorticity, and cluster 3 (blue): forward velocity, achieving an average of 94.90 ± 2.05 % classification accuracy.

4.4. Discussion

Using ML, we have devised a differentiation algorithm for BAV with aortic dilation based on hemodynamic parameters derived from 4D Flow CMR. After comparing multiple ML methods, the results showed that the accuracy gained with feature selection vs. all features in the final classifiers used is not that considerable (Bissell *et al.,* 2013) (Atkins *et al.,* 2014) (Allen *et al.,* 2015) (Boudoulas *et al.,* 2015) (Pasipoularides *et al.,* 2019) (Soulat *et al.,* 2021) (Guala *et al.,* 2021). Nevertheless, considering the large number of flow descriptors proposed to classify BAV patients with aortic dilation., the use of feature selection algorithms allows for the reduction of the number of input variables used to develop a predictive model without losing accuracy. Therefore, we found that combining five hemodynamic features selected by SFS and applying them to the LDA classification algorithm achieves the best performance with an accuracy of 96.31 ± 1.76%, which is higher than the accuracy of random forest (96.00 ± 2.70 %).

Both classification tasks with LDA and random forest showed better performance when including AAo and AArch than only features in AAo (SFS

reaching 93.27 ± 2.34% accuracy and random forest resulting in 94.00 ± 2.00% accuracy). This result suggests that for the classification it is important to include parameters in AAo and AArch. Further, both classifiers did not show significant differences, but in the NON-DIL BAV class. For this class, the LDA was sensitive to the selected test data as showed large variance for precision, sensitivity, and specificity in the cross-validation experiment.

Feature selection algorithm SFS found five-top performing features including: velocity angle, forward velocity, vorticity, backward velocity in the AAo, and helicity density in the AArch. PCA's five best-performing features were: velocity angle, forward velocity and velocity, in the AAo, and velocity and energy loss in the AArch. Interestingly, the most important parameters found by Random Forest were velocity angle, backward velocity, eccentricity, axial circulation, and regurgitation all of them localized in the AAo. Thus, algorithms consistently identify velocity angle as key descriptors of BAV hemodynamics, a result in line with previous research, and most of them highlighted the importance of forward and backward velocity components and the role of rotational flow descriptors, such as helicity, circulation and vorticity (Bissel *et al.,* 2013) (Lorenz *et al.,* 2014).

Notably, the algorithms did not select WSS or its components, all previously related cross-sectional and longitudinal data with dilation in BAV. This may have resulted from averaging these biomarkers over aortic wall regions or reflect their relatively lower reproducibility than bulk flow measures. Furthermore, the present WSS assessment may be limited in evaluating the spatiotemporal complexity of this biomarker (Calò *et al.,* 2021). Alternatively, the Eulerian method to analyze WSS topological skeleton by identifying and classifying WSS fixed points and manifolds in complex vascular geometries can increase the chance of finding mechanistic explanations to clinical observations as presented by Mazzi *et al.* (Mazzi *et al.,* 2020), analysis that may be added in the ML classification algorithms in future works.

The structure and information of bootstrap-aggregated decision trees were extracted to count and analyze the extent of the influence of various hemodynamic parameters on BAV dilation to determine the parameters most closely related to the

dilation of the aorta in this disease. This suggests that velocity angle in AAo is the most important predictor, followed by backward velocity, eccentricity, axial circulation, and regurgitation in AAo. These variables align with those identified in previous studies, which related high asymmetrical shear stresses with aortic dilation in BAV disease (Rodríguez-Palomares *et al.,* 2018) (Mahadevia *et al.,* 2014). However, a decision tree further allows for the identification of the relative importance of each flow descriptor in the classification task, showing how velocity angle and flow eccentricity, two descriptors of asymmetric flow, backward velocity and axial circulation, and regurgitation bringing information of flow rotation are the dominant factors. The proposed decision tree model could differentiate the three classes with 96.00 ± 0.83 accuracy using five features selected by SFS. Nevertheless, this decision tree was our second-best result and appeared to be most helpful in determining HV and DIL BAV classes. Instead of the LDA that ascertains better the three classes, including the NON-DIL BAV class.

Aortic stenosis in BAV patients has been reported that increased with the patient's age (Ferencik *et al.,* 2013) (Lewin *et al.,* 2015). Therefore, the patient's age can be a possible confounding factor in the classifiers. We executed another experiment, including age as an input parameter. However, features selection algorithms, SFS and PCA, did not find age as their top-best performing features (see Supplementary Table C.6).

In this study, the hierarchical clustering method provided an alternative for reliable correlation between hemodynamic parameters from 4D-flow CMR. By classifying them into three different clusters according to their similarities, the resulting dendrogram provides a good representation of the relationship of various parameters in two aorta regions. According to hierarchical cluster analysis, we can assume that features by SFS have a better performance than those selected by other feature selection algorithms because it has a wide representation of each clustering: cluster 1(green) velocity angle and backward velocity in AAo, cluster 2 (red) vorticity in AAo; and cluster 3 (blue): forward velocity and helicity density in AAo and AArch, respectively. When statistical modeling is used to pursue a predictive aim, Gregorich *et al.,* showed that two highly correlated independent variables will

lead to high variance in the predictions, even if both variables are relevant for prediction. In small samples, it may then be beneficial to omit one of the pair to decrease that variance, even if this incurs some new bias in the predictions (Gregorich *et al.,* 2021). Further, O'Brien shows that multicollinearity is not a sufficient reason to eliminate variables from a model. A more important criterion to consider when contemplating dropping a variable from model is 'model influence' (O'Brien *et al.,* 2017). Although, we studied the correlation and clustering of the features, this information was not used to intervene in the ML model since the latter selects the features automatically. Instead, we used the cluster information to explain the relation of the features selected by ML and the localization of these parameter across the different clusters.

One of the strengths of our study is that it provides a comprehensive overview of the relative performance of different ML algorithms for BAV aortopathy classification. These results can be used to guide researchers in the selection of an appropriate ML algorithm for their studies. Hence, non-linear interactions can be associated with the selected features that better identify HV and BAV patients.

4.4.1. Limitations

Considering the small number of subject data, we did not explore the use of advanced deep learning algorithms. Instead, we used classical ML algorithms such as random forest and SVM. However, with both methods, we achieved a high classification accuracy. Deep networks require extremely large datasets to achieve high performance. In future studies, we will include more data in our dataset to perform advanced deep learning methods and compared them with classical ML algorithms results. Another limitation of the current study is the small number of NON-DIL BAV types, which unbalanced the analyzed classes. However, the cross-validation assessment aimed to reduce the effect of this issue in the classification output.

Additionally, from the acquisition point of view, the movement of the aorta along the cardiac cycle was not considered in this study since technical limitations

in 4D-flow CMR acquisitions, as poor contrast and low signal-to-noise ratio, make it challenging to obtain a time-resolved segmentation of the aorta.

Further, in this study, we averaged parameters along the circumference of each region, which can induce a sub-estimation of local values. Nevertheless, assessing the local impact of all hemodynamic parameters for classification would require more patients from a statistical point of view, as there would be more parameters than subjects.

Finally, another limitation is the absence of longitudinal data. Performing a similar study would elucidate if the parameters that best classify BAV patients with and without aortic dilation would also be the best predictor for aortic dilation in those patients. A paper with longitudinal outcomes was recently published; however, only WSS was assessed as a predictor for dilation in that study (Boudoulas *et al.*, 2015).

4.5. Conclusions

The main contributions of the paper are twofold. On the one hand, we analyzed and extracted multiple correlation patterns of hemodynamic parameters, finding which parameters showed high collinearity between them, which allows us to diminish their size to a few variables. Also, we defined five hemodynamic features that best classify HV and BAV with and without aortic dilation using SFS: velocity angle, forward velocity, vorticity, and backward velocity in AAo, and helicity density in AArch. The best-performing methods were with features selected by SFS in LDA and random forest classifiers with 96.31 ± 1.76 % and 96.00 ± 0.83 %, respectively. Moreover, we found five features by SFS: velocity angle, eccentricity, backward velocity, and oscillatory shear index in AAo, and regurgitation fraction in AArch, that best classified BAV patients' groups (NON-DIL BAV and DIL BAV classes) using LDA classifier with 96.18 ± 2.34 % accuracy.

4.6. Acknowledgements

Millennium Science Initiative of the Ministry of Economy, Development and Tourism, grant Nucleus for Cardiovascular Magnetic Resonance. We are also grateful to Biomedical Imaging Center at Pontificia Universidad Católica de Chile and Hospital Universitari Vall d´Hebron for support this research.

5. FUTURE WORK AND PERSPECTIVES

This section shows three general ideas regarding the three articles to deeper analyze particular issues, and new proposals of different methods.

5.1. First Article: Comparison of Unwrapping Methods in Patients

Concerning the limitations of our study, the method was not assessed in a cohort of patients, only in two volunteers (volunteer 15: female, 60-year-old, and volunteer 22: male, 73-year-old) from our cohort had cardiovascular disease. Specifically, the first one was affected by hypertension and slightly prominent left ventricular walls. The second one suffered from diabetes (Figure 5-1.a). Left ventricular hypertrophy leads to weak suction pumps and has high wall tension, implying lower velocity values than healthy volunteers (Pedrizzetti *et al.*, 2014) (Arvidsson *et al.*, 2016). And diabetes is associated with high blood pressure, which decreases blood and oxygen flow to the heart (Leon *et al.*, 2015). Although the hemodynamic is affected in this particular case, the unwrapping methods had the same behavior as healthy volunteers (Figure 5-1.b.).

Considering the previous results, it will be interesting to compare the unwrapping methods in a cohort of cardiovascular disease patients, especially in aortic stenosis patients. We hypothesize that the unwrapping method will probably have the same behavior as in healthy volunteers. Nevertheless, a noise analysis will be an interesting performance considering the abnormal flows.

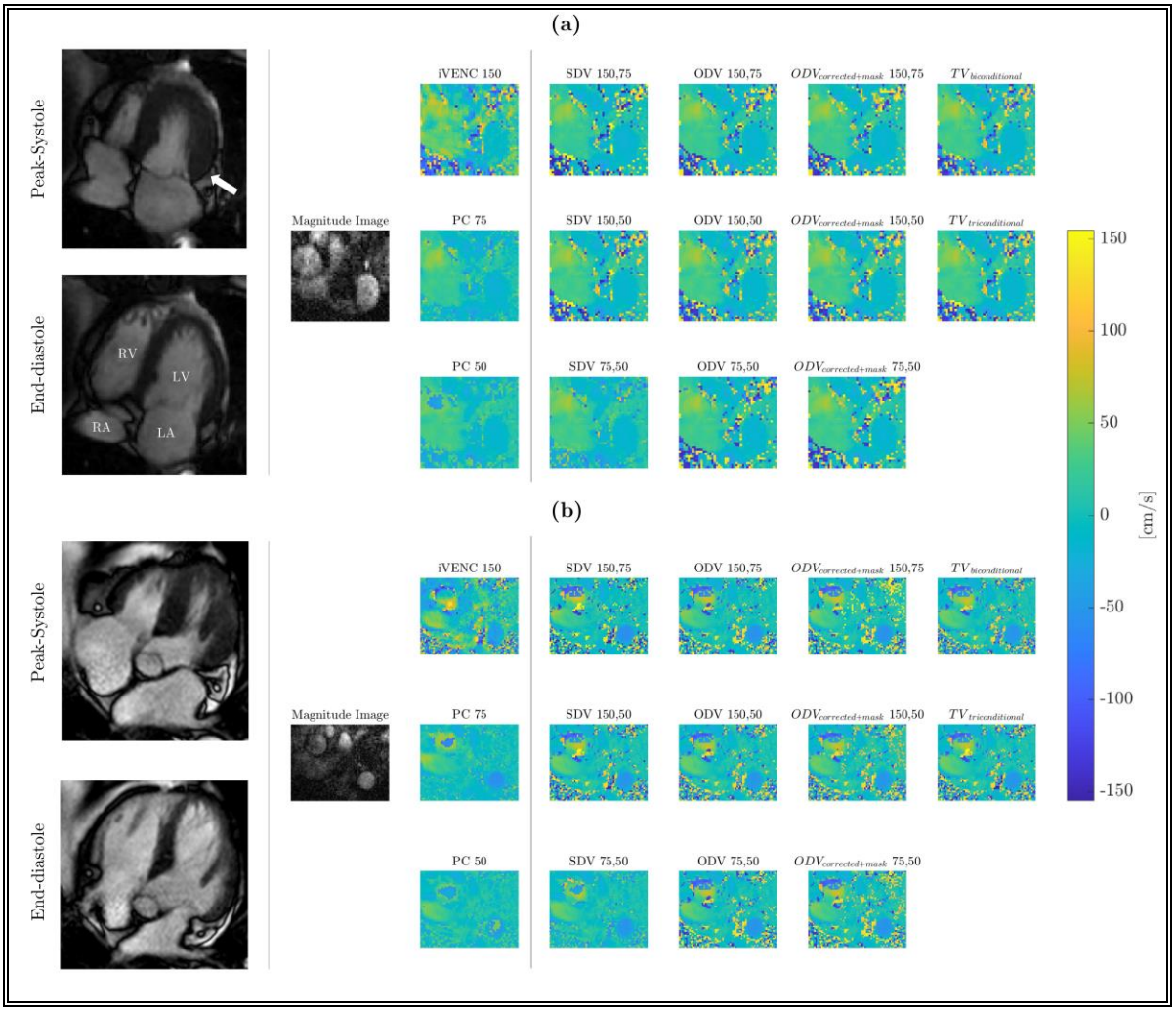

Figure 5-1. Cardiac magnetic resonance images: (a) 60 years old woman (volunteer 15) affected by hypertension and slightly prominent left ventricular walls (white arrow). (b) 73 years old men (volunteer 22) affected by diabetes. From left to right: (left) Multi-slice 2D cine balanced steady-state free precession (b-SSFP) four-chamber images at peak-systole and end-diastole. LA: left atrium; LV: left ventricle; RA: right atrium; RV: right ventricle. (right) Ascending and descending aorta at peak systole. First row: magnitude image, second row: triple-VENC images, third row: SDV images, fourth row: ODV images, fifth row: ODV corrected with masking ROI images, and sixth row: TV bi- and tri-conditional images. PC: single-VENC PC-MRI; SDV: Standard Dual-VENC Method; ODV: Optimal Dual-VENC Method; TV: Triple-VENC Method.

5.2. Second Article: Assessment of Right Intraventricular Hemodynamic Parameters

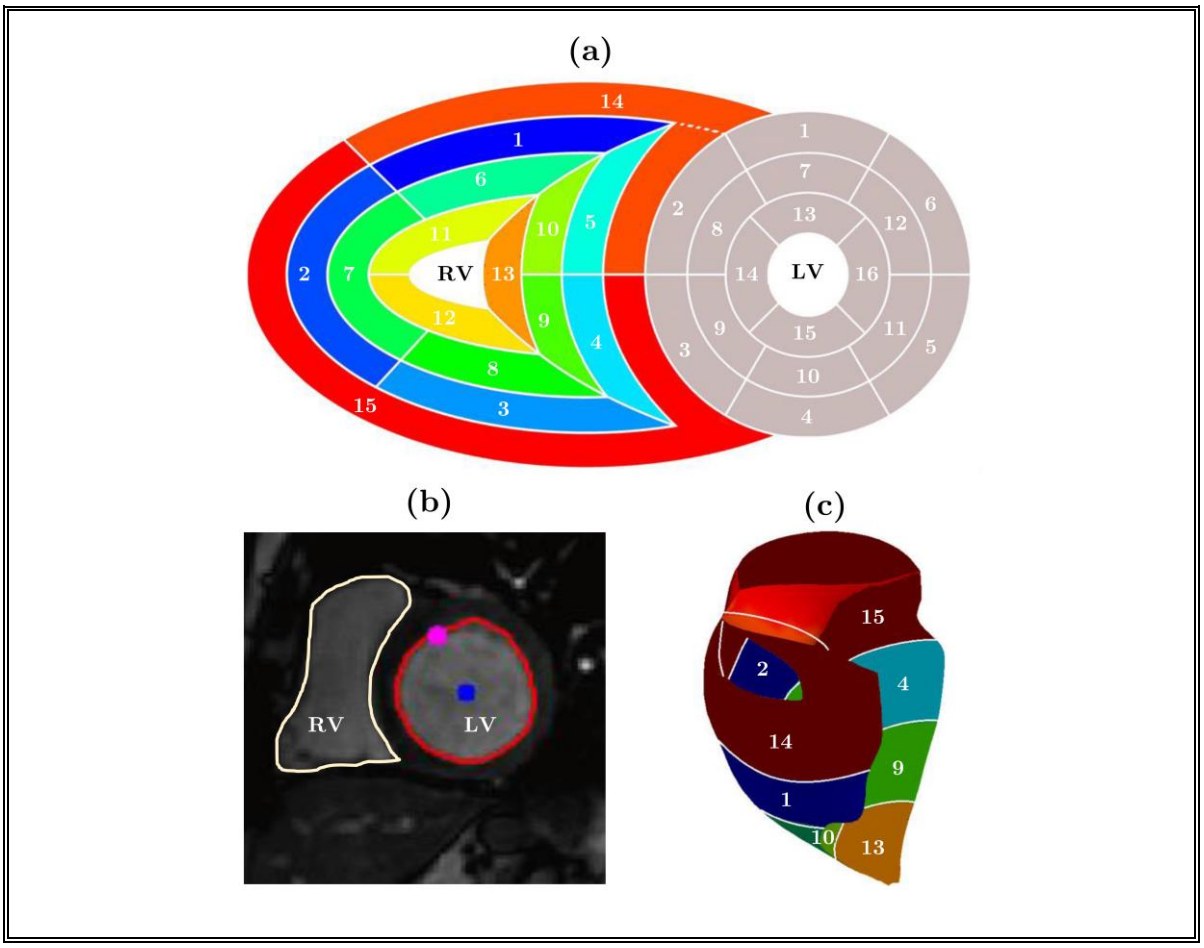

Figure 5-2. (a) 15- and 16- segment models for the RV and LV, respectively. (b) The LV and RV segmentation from short-axis b-SSFP images. (c) Illustration of a tetrahedral mesh of the RV. RV: right ventricle; LV: left ventricle.

The second article developed a method to characterize the left intraventricular hemodynamics in the left ventricle (LV) from 4D Flow MRI using a finite element method, applied in a cohort of dilated cardiomyopathy (DCM) patients. Nevertheless, this methodology could be expanded into more cardiovascular diseases or even in the assessment of right intraventricular hemodynamic parameters (Arvidsson *et al.*, 2016) (Hirtler *et al.*, 2016) (Browning *et al.*, 2017)

(Fredriksson *et al.*, 2018) (Ding *et al.*, 2021). In hypertrophic cardiomyopathy (HCM), its main characteristic is symmetrical or asymmetrical hypertrophy of the LV and/or right ventricle (RV). Most previous studies mainly include the LV for the definition of HCM, thus neglecting the RV. But recently, many studies have reported right ventricular involvement in HCM (Ding *et al.*, 2021).

We must consider that the local hemodynamic analysis is different in the RV than in the LV due to the 15-segment model, as shown in Figure 5-2.a (Tokodi *et al.*, 2021). Therefore, we proposed the following methodology for quantitative evaluated the intraventricular hemodynamics from both LV and RV segmentations from a 4D Flow dataset: First, we can perform registration of the 4D Flow with the b-SSFP images. Second, we double the number of slices in the b-SSFP images. Then, the LV and RV endocardium will be automatically segmented throughout all cardiac phases in the sort-axis b-SSFP images, using the image analysis software Segment, as shown in Figure 5-2.b. The LV and RV centerlines will be calculated automatically by detecting the centroid of the LV and RV contours in each slice and connected to create a line. To determine the three sections of the ventricles (basal, mid-cavity, and apical), we will divide the centerline into three equal parts perpendicular to the long axis of the heart. Note that an additional point (magenta) will be manually placed at the junction between the RV free wall and the interventricular septum from the LV. Landmarks will be uniformly distributed along the boundaries based on these positions and apply the segment-model corresponding to each ventricle. Afterward, we will create a tetrahedral mesh (Figure 5-2.c) and transfer the velocity information at each mesh node from the 4D Flow MRI datasets using cubic interpolation. Finally, we will calculate the hemodynamic parameters under study.

Therefore, this study allows us to estimate global and local analyses of both ventricles. Hence, if the dataset's size is appropriate, we would find the hemodynamic biomarkers of the particular cardiovascular disease, e.g., HCM, using a similar machine learning strategy presented in the third article.

5.3. Third Article: Age as an Output Feature and Longitudinal Study of Bicuspid Aortic Valve

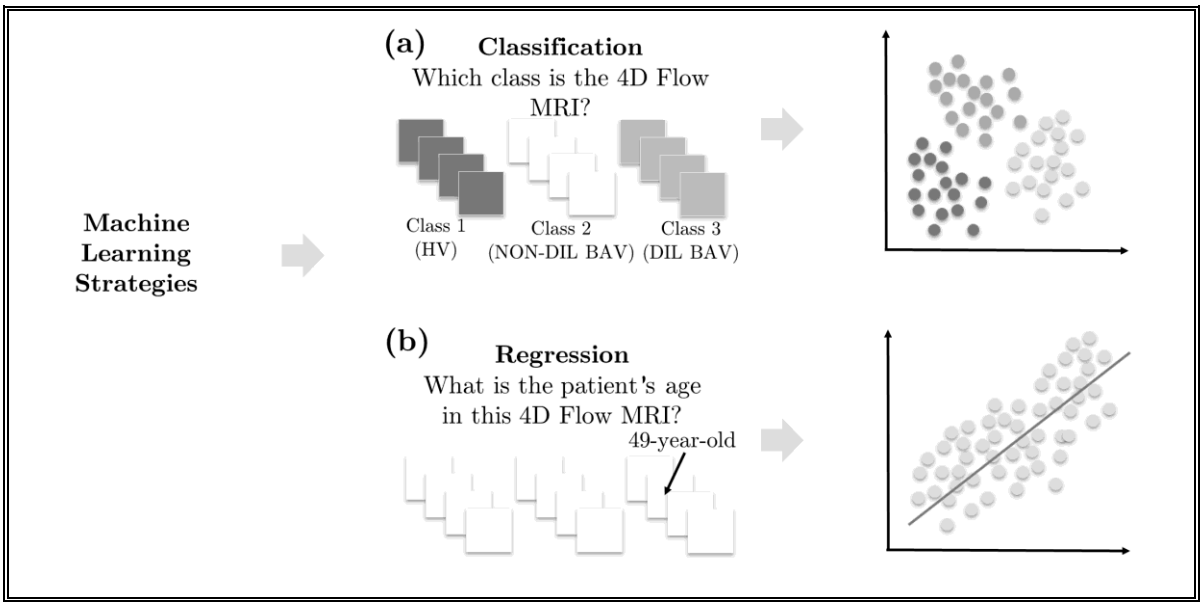

Figure 5-3. Machine Learning Strategies. (a) In our published article, we considered three different classes as input it implies that the output will we one of the three-classes. (b) Nevertheless, our model output is age's patient (a number), we have to deal with a regression problem.

Our machine learning strategy showed that including age as an input parameter. The features selection algorithms, SFS and PCA, did not find their top-best performing features even if Ferencik *et al.* and Lewin *et al.* reported that increased aortic stenosis in bicuspid aortic valve (BAV) with patient's age (Ferencik *et al.*, 2003) (Lewin *et al.*, 2005). Therefore, we would like to reformulate the machine learning strategy and use age as an output using a regression algorithm, e.g., linear regression, as shown in Figure 5-3.

On the other hand, we would like to perform a similar study as published using a longitudinal study of BAV patients with and without aortic dilation. Performing a similar analysis would elucidate if the parameters that best classify BAV patients would also be the best predictor for aortic dilation in those patients. An article with

longitudinal outcomes was recently published; however, this study assessed only wall shear stress as a predictor for dilation (Soulat *et al.*, 2021).

Therefore, we proposed the following strategy to performance a longitudinal study in BAV patients using machine learning, as shown Figure 5-4. The figure illustrates how we can define the observation and prediction window. It also shows how we can model longitudinal hemodynamic parameters in BAV patients. First, we will aggregate each feature across the 3 to 5-year observation window (e.g., velocity, velocity angle in AAo and AArch). Second, we will extract each year value of each feature and concatenate the temporal values from all BAV patients in a two-dimensional matrix for a classifier (e.g., random forest). Finally, we will perform a tensor representation on temporal values from all patients for convolutional neural networks and recurrent neural networks with long short-term memory.

Note that we can also performance a prediction of 10-year using the hemodynamic parameters, comparing to a gold standard achieved.

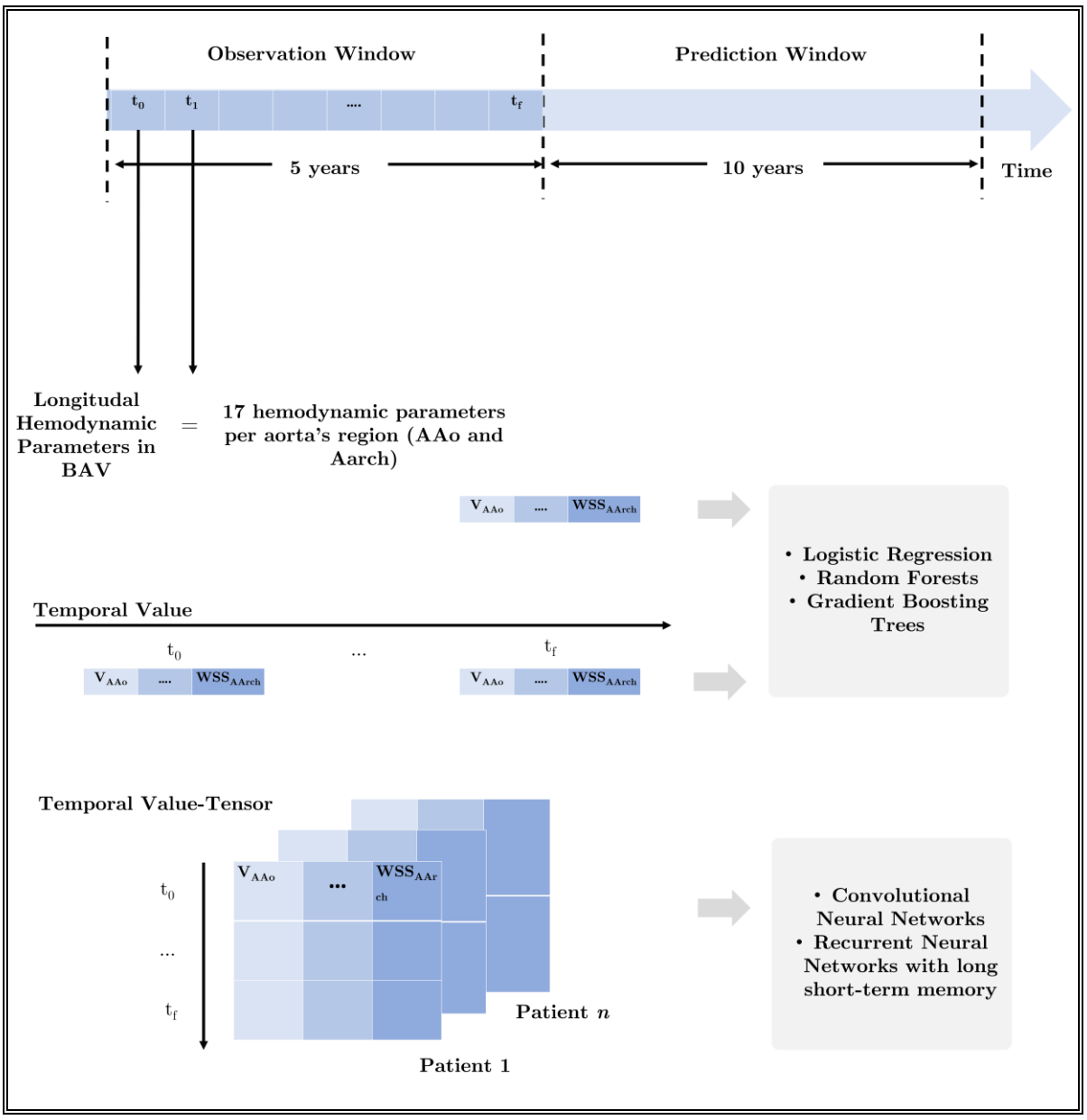

Figure 5-4. A longitudinal study over a, e.g., five years follow-up period review bicuspid aortic valve (BAV) patients using Machine Learning.

6. CONCLUSIONS

In the preceding chapters, a complete framework that allows us to estimate accurate hemodynamic parameters in the heart and great vessels from velocity MR images were presented in a totally non-invasive manner. This investigation performed relevant information on reconstruction techniques, image processing, data quantification, pattern recognition, and machine learning in three independent articles.

The first article reviews and compares dual-VENC unwrapping methods when strictly unidirectional measurements. Furthermore, we developed a correction method based on the information provided by the Optimal Dual-VENC method (ODV). We also present a noise analysis of the velocity estimates of the different methods. We found that the quality of the results depends on the proportion of the VENCs of the input images, with $VENC_L/VENC_H = 0.5$ being the best performing combination for all methods. For that VENC combination, the most robust unwrapping method appears to be the corrected ODV method, while the other methods show similar performance in terms of unwrapping success.

The second article describes a methodology for quantitative evaluation of intraventricular hemodynamics using a single segmentation from a 4D Flow dataset and a finite-element method. To show the applicability in a small cohort of dilated cardiopathy (DCM) patients to find which parameters were different from healthy volunteers (HV). We demonstrate that velocity, vorticity, viscous dissipation, energy loss, and kinetic energy can characterize changes in intraventricular flow in DCM patients compared to HV. Moreover, our evidence shows that although ejection fraction may be recovered, the hemodynamic remain low. Therefore, our approach was able to identify abnormal flow patterns in DCM patients compared to HV and can be applied to any other cardiovascular disease.

The third article provides a comprehensive overview of the relative performance of different machine learning (ML) algorithms for bicuspid aortic valve (BAV) aortopathy classification. We defined five hemodynamic features that best classify HV and BAV with and without aortic dilation using SFS: velocity angle, forward

velocity, vorticity, and backward velocity in ascending aorta (AAo), and helicity density in the aortic arch (AArch). The best-performing methods were with features selected by SFS in LDA and random forest classifiers with 96.31 ± 1.76% and 96.00 ± 0.83%, respectively. Moreover, we found five features by SFS: velocity angle, eccentricity, backward velocity, oscillatory shear index in AAo, and regurgitation fraction in AArch, that best classified BAV patients' groups (NON-DIL BAV and DIL BAV classes) using LDA classifier with 96.18 ± 2.34% accuracy. These results can be used to guide researchers in the selection of an appropriate machine learning algorithm for their studies.

Thought the fact that the topics developed in this thesis were not tested together, future research may combine all these topics to investigate and improve the examination in the cardiovascular system. Therefore, the methods proposed in this thesis could improve the use of 4D Flow MRI for clinical research and potential translation to clinical settings.

REFERENCES

Allen BD, van Ooij P, Barker AJ, et al. Thoracic aorta 3D hemodynamics in pediatric and young adult patients with bicuspid aortic valve. J Magn Reason Imaging. 2015; 42(4): 954-63. doi: 10.1002/jmri.24847

Al-Wakeel N, Fernandes JF, Amiri A, Siniawski H, Goubergrits L, Berger F, Kuehne T. Hemodynamic and energetic aspects of the left ventricle in patients with mitral regurgitation before and after mitral valve surgery. J Magn Reson Imaging. 2015; 42(6):1705-12.

Ambale-Venkatesh B, Yang X, O Wu C, et al. Cardiovascular Event Prediction by Machine Learning: The Multi-Ethnic Study of Atherosclerosis, Circ Res. 2017 Oct 13;121(9):1092-1101. doi: 10.1161/CIRCRESAHA.117.311312

Amorim S, Rodrigues J, Campelo M, Moura B, Martins E, Macedo F, Silva-Cardoso J, Júlia Maciel M. Left ventricular reverse remodeling in dilated cardiomyopathy-maintained subclinical myocardial systolic and diastolic dysfunction. Int J Cardiovasc Imaging 2017 May;33(5):605-613.

Arvidsson PM, Kovács SJ, Töger J, Borgquist R, Heiberg E, Carlsson M, Arheden H. Vortex ring behavior provides the epigenetic blueprint for the human heart. Sci Rep. 2016; 26; 6:22021.

Atkins S, Sucosky P, Etiology of bicuspid aortic valve disease: Focus on hemodynamics, World J Cardiol. 2014 Dec 26; 6(12):1227-1233. doi: 10.4330/wjc.v6.i12.1227

Avendi M, Kheradvar A, Jafarkhani, Automatic segmentation of the right ventricle from cardiac MRI using a learning-based approacg. Magn Reson in Med. 2017 Dec; 78(6):2439-2448. doi: 10.1002/mrm.26631

Aviles J., Maso Talou GD., Camara O., Marcos MC., Morales Ferez X., Romero D., et al. Domain Adaptation for Automatic Aorta Segmentation of 4D Flow Magnetic Resonance Imaging Data from Multiple. Functional Imaging and Modeling of the Heart. FIMH 2021. Lecture Notes in Computer Science, vol. 12738. 2021. pp. 112–21.

Bernstein MA, Grgic Mladen, Brosnan TJ, Pelc NJ. Reconstructions of Phase Contrast, Phased Array Multicoil Data. Magn Reson Med. 1994; 32(3):330-4.

Bernstein MA, Shimakawa A, Pelc N. Minimizing TE in moment-nulled or flow-encoded two- and three-dimensional gradiente-echo imaging. J Magn Reson Imaging 1992; 2(5):583-8. doi:10.1002/jmri.1880020517

Bissell MM, Hess AT, Biasiolli L, et al. Aortic dilation in bicuspid aortic valve disease: flow pattern is a major contributor and differs with valve fusion type. Circ Cardiovasc Imaging 2013; 6:499–507. doi: 10.1161/CIRCIMAGING.113.000528

Boudoulas K, Wolfe B, Lilly S et al. The aortic stenosis complex: aortic valve, atherosclerosis, aortopathy. J Cardiol. 2015; 65:377-382. doi: 10.1016/j.jjcc.2014.12.021

Browning JR, Hertzberg JR, Schroeder JD, Fenster BE. 4D Flow Assessment of Vorticity in Right Ventricular Diastolic Dysfunction. Bioengineering (Basel) 2017 Apr 5;4(2):30.

Calò K, Gallo D, Guala A, Rodriguez-Palomares J, Scarsoglio S, Ridolfi L, Morbiducci U. Combining 4D Flow MRI and Complex Networks Theory to Characterize the Hemodynamic Heterogeneity in Dilated and Non-dilated Human Ascending Aortas. Ann Biomed Eng. 2021 Sep;49(9):2441-2453

Campello M., Gkontra P., Izquierdo C., Mart C., Sojoudi A., Full PM., et al. Multi-Centre, Multi-Vendor and Multi-Disease Cardiac Segmentation: The M&Ms Challenge. IEEE Trans Med Imag 2021:1–12. Doi:10.1109/TMI.2021.3090082.

Campens L, Demulier L, De Groote K, et al. Reference values for echocardiographic assessment of the diameter of the aortic root and ascending aorta spanning all age categories. Am J Cardiol. 2014;114(6):914-20.

Cantor E, Salas R, Rosas H, et al. Biological knowledge-slanted random forest approach for the classification of calcified aortic valve stenosis, BioData Mining 2021 Jul 23;14(1):35. doi: 10.1186/s13040-021-00269-4.

Carrillo H, Osses A, Uribe S and Bertoglio C. Optimal Dual-VENC (ODV) Unwrapping in Phase-Contrast MRI. IEEE Trans Med Imaging. 2019; 38(5):1263-1270.

Ciaburro G. MATLAB for Machine Learning: Practical examples of regression, clustering and neural networks, Publisher: Packt Publishing, 2017, ISBN: 978-1788398435

Della Corte A, Bancone C, Dialetto G, et al. The ascending aorta with bicuspid aortic valve: a phenotypic classification with potential prognostic significance. Eur J Cardiothorac Surg. 2014;46(2):240-7.

Dey D, Slomka P, Leeson P et al. Artificial Intelligence in Cardiovascular Imaging: JACC State-of-the-Art Review. J Am Coll Cardiol. 2019; 73(11); 1317-1335. doi: 10.1016/j.jacc.2018.12.054

Dragulescu A, Mertens L, Friedberg M. Interpretation of Left Ventricular Diastolic Dysfunction in Children With Cardiomyopathy by Echocardiography. Circ Cardiovasc Imaging. 2013; 6:254-261.

Dux-Santoy L, Guala A, Sotelo J, et al. Low and Oscillatory Wall Shear Stress Is Not Related to Aortic Dilation in Patients With Bicuspid Aortic Valve: A Time-Resolved 3-Dimensional Phase-Contrast Magnetic Resonance Imaging Study, Arterioscler Thromb Vasc Biol. 2020 Jan;40(1):e-10-e20.

Dux-Santoy L., Guala A., Teixido-Tura G., Ruiz-Muñoz A., Maldonado G., Villalva N., et al. Increased rotational flow in the proximal aortic arch is associated with its dilation in bicuspid aortic valve disease. Eur Heatr J - Cardiovasc Imaging 2019;20(12):1407–17. Doi: 10.1093/ehjci/jez046.

Dyverfeldt P, Bissell M, Barker AJ, Bolger AF, Carlhäll C-J, Ebbers T, Francios CJ, Frydrychowicz A, Geiger J, Giese D, Hope MD, Kilner PJ, Kozerke S, Myerson S, Neubauer S, Wieben O, Markl M. 4D Flow cardiovascular magnetic resonance consensus statement. J Cardiovasc Magn Reson. 2015; 17(1):72.

Elliott P, Andersson B, Arbustini E, Bilinska Z, Cecchi F, Charron P, Dubourg O, Kühl U, Maisch B, McKenna WJ, Monserrat L, Pankuweit S, Rapezzi C, Seferovic P, Tavazzi L, Keren A. Classification of the cardiomyopathies: a position statement from the European Society Of Cardiology Working Group on Myocardial and Pericardial Diseases. Eur Heart J. 2008 Jan;29(2):270-276.

Eriksson J, Bolger A, Ebbers T, Carlhäll C. Assessment of left ventricular hemodynamic forces in healthy subjects and patients with dilated cardiomyopathy using 4D Flow MRI. Physiol Rep 2016 4(3):e12685.

Eriksson J, Bolger A, Ebbers T, Carlhäll C-J. Four-dimensional blood flow-specific markers of LV dysfunction in dilated cardiomyopathy. Eur Heart Cardiovasc Imaging. 2013 May;14(5):417-24.

Evangelista A, Gallego P, Calvo-Iglesias et al. Anatomical and clinical predictors of valve dysfunction and aortic dilation in bicuspid aortic valve disease. Heart. 2018;104(7):566–573. doi: 10.1136/heartjnl-2017-311560

Fang Q, Boas D. Tetrahedral mesh generation from volumetric binary and gray-scale images. Proceedings of IEEE International Symposium on Biomedical Imaging: From Nano to Macro 2009; 1142-1145.

Ferencik M, Pape LA. Changes in size of ascending aorta and aortic valve function with time in patients with congenitally bicuspid aortic valves. Am J Cardiol. 2003; 92: 43–46.

Foell D, Jung BA, Germann E, Staehle F, Bode C, Henning J, Markl M. Segmental Myocardial Velocities in Dilated Cardiomyopathy With and Without Left Bundle Branch Block. J Magn Reson Imaging 2013 Jan; 37(1):119-26.

Fouras A, Soria J. Accuracy of out-of-plane vorticity measurements derived from in-plane velocity field data. Exp Fluids 1998; 25:409-430.

Frangi AF, Niessen WJ, Viergever MA. Three-dimensional modeling for functional analysis of cardiac images: a review. IEEE Trans Med Imaging 2007; 20(1):2-25.

Fredriksson A, Trzebiatowska-Krzynska A, Dyverfeldt P, Engvall J, Ebbers T, Carlhäll C-J. Turbulent kinetic energy in the right ventricle: Potential MR marker for risk stratification of adults with repaired Tetralogy of Fallot. J Magn Reson Imaging 2018;47(4):1043-1053.

Friedberg MK, Roche SL, Mohammed AF, Balasingam M, Atenafu EG, Kantor PF. Left Ventricular Diastolic Mechanical Dyssynchrony and Associated Clinical Outcomes in Children With Dilated Cardiomyopathy. Circ Cardiovasc Imaging, 2008 1(1):50-7.

Ghiglia D and M. Pritt D, Two-Dimensional Phase Unwrapping: Theory, Algorithms, and Software (Wiley, 1998).

Girdauskas E, Borger M, Secknus M, et al. Is aortopathy in bicuspid aortic valve disease a congenital defect or a result of abnormal hemodynamics? A critical reappraisal of a one-sided argument. Eur J Cardiothorac Surg. 2011; 39:809.14

Girdauskas E, Petersen J, Neumann N et al. Novel Approaches for BAV Aortopathy Predition – Is There a Need for Cohort Studies and Biomrakers? Biomolecules. 2018; 8(3):58. doi: 10.3390/biom8030058

Gregorich M, Strohmaier S, Dunker D, Heinze G. Regression with Highly Correlated Predictors: Variable Omission Is Not the Solution. Int J Environ Res Public Health. 2021 Apr 17;18(8):4259

Gu T, Korosec F, Bloch W, et al. PC VIPR: a high-speed 3D phase-contrast method for flow quantification and high-resolution angiography- AJNR Am J Neuroradiol. 2005;26(4):743-9

Gu Y, Wang C. A Study of Hierarchical Correlation Clustering for Scientific Volume Data, Advances in Visual Computing, 2010, Volume 6455. ISBN: 978-3-642-17276-2

Guala A, Dux-Santoy L, Teixido-Tura G, et al., Wall shear stress predicts aortic dilation in patients with bicuspid aortic valve. In press JACC cardiovascular imaging

Ha H, Kim GB, Kweon J, Lee SJ, Kim YH, Lee DH, Yang DH, Kim N. Hemodynamic Measurement Using Four-Dimensional Phase-Contrast MRI: Quantification of Hemodynamic Parameters and Clinical Applications, Korean J Radiol. 2016; 17(4): 445.62.

Heiberg E, Sjögren J, Ugander M, Carlsson M, Engblom H, Arheden H. Design and validation of Segment–freely available software for cardiovascular image analysis. BMC Medical Imaging 2010; 10(1):1.

Heiberg E, Wigström L, Carlsson M, Bolger AF, Karlsson M. Time Resolved Three-dimensional Segmentation of the Left Ventricle. In proceedings of IEEE Computers in Cardiology. 2005; 32:599-602.

Hershberger RE, Morales A. Dilated Cardiomyopathy Overview. GeneReviews® [Internet]. https://www.ncbi.nlm.nih.gov/books/NBK1309/. Accessed 27 July 2007.

Hill JA, Olson EN. Cardiac plasticity. N Engl J Med 2008; 358(13):1370–80.

Hirtler D, Garcia J, Barker AJ, Geiger J. Assessment of intracardiac flow and vorticity in the right heart of patients after repair of tetralogy of Fallot by flow-sensitive 4D MRI. Eur Radiol 2016(10):3598-607.

Johnson K, Lum D, Turski P, et al. Improved 3D phase contrast MRI with off-resonance corrected dual Echo VIPR. Magn Reson Imaging. 2012;60(6):1329-36. doi: 10.1002/mrm.21763.Improved

Johnson M and Markl M, Improved SNR in Phase Contrast Velocimetry with 5-Point Balanced Flow Encoding. Magn Reson Med. 2010; 63(2): 349-355.

Kang JW, Song HG, Yang DH, Baek S, Kim DH, Song JM, et al. Association between bicuspid aortic valve phenotype and patterns of valvular dysfunction and bicuspid aortopathy: comprehensive evaluation using MDCT and echocardiography. JACC Cardiovasc Imaging.2013;6(2):150-61.

Kanski M, Arvidsson PM, Töger J, Borgquist R, Heiberg E, Carlsson M, Arheden H. Left ventricular fluid kinetic energy time curves in heart failure from cardiovascular magnetic resonance 4D Flow data. J Cardiovasc Magn Reson 2015; 17-111

Kerfoot E, Fovargue L, Rivolo S, Shi W, Rueckert D, Nordsletten D, Lee J, Chabiniok R, Razavi R. Visualization and Computational Framework for Multi-modal Biomedical Data Analysis. In: Zheng G, Liao H, Jannin P, Cattin P, Lee SL (eds) Medical Imaging and Augmented Reality, MIAR 2016. Lecture Notes in Computer Science, vol 9805. Springer, Cham.

Kvitting JP, Ebbers T, Wigstrom L, Engvall J, Olin CL, Bolger AF. Flow patterns in the aortic root and the aorta studied with time-resolved, 3-dimensional, phase-contrast magnetic resonance imaging: implications for aortic valve-sparing surgery. J Thorac Cardiovasc Surg. 2004; 127(6): 1602-1607.

Lan T, Erdogmus D, Hayflick SJ, Szumowski JU. Phase Unwrapping and Background Correction in MRI. IEEE Workshop on Machine Learning for Signal Processing. 2008, pp. 239-243

Lee AT, Pike B and Pelc NJ, Three-Point Phase-Contrast Velocity Measurements with Increased Velocity-to-Noise Ratio, Magn Reson Med. 1995; 33(1):122-6.

Lewin M, Otto C, The Bicuspid Aortic Valve: Advense Outcomes From Infancy to Old Age. Circulation. 2005 Feb 22;111(7):832-4, doi: 10.1161/01.CIR.0000157137.59691.0B.

Liu J, Shar JA, Sucosky P. Wall Shear Stress Directional Abnormalities in BAV Aortas: Toward a New Hemodynamic Predictor of Aortopathy? Front Physiol. 2018; 14;9:993.

Lorenz R, Benk C, Bock J, et al. Closed circuit MR compatible pulsative pump system using a ventricular assist device and pressure control unit. Magn Reson Med. 2012; 67:258-268.

Lorenz R, Bock J, Barker AJ, von Knobelsdorff-Brenkenhoff F, Wallis W, Korvink JG, Bissell MM, Schulz-Menger J, Markl M. 4D Flow MRI in bicuspid aortic valve disease demonstrates altered distribution of aortic blood flow helicity. Magn Reson Med. 2014 Apr;71(4):1542.1553.

Lorenz R, Bock J, Barket AJ, et al., 4D flow magnetic resonance imaging in bicuspid aortic valve disease demonstrates altered distribution of aortic blood flow helicity. Magn Reson Med. 2014 Apr; 71(4):1542-53. doi: 10.1002/mrm.24802

Ma LE, Markl M, Chow K, Vali A, Wu C, Schnell S. Efficient triple-VENC phase-contrast MRI for improved velocity dynamic range. Magn Reson Med. 2020 Feb;83(2):505-520.

Mahadevia R, Barker AJ, Schnell S, et al., Bicuspid aortic cusp fusion morphology alters aortic three-dimensional outflow patterns, all shear stress, and expression of aortopathy. Circulation. 2014, 29:673-682. doi: 10.1161/CIRCULATIONAHA.113.003026.

Mahmaljy H, Yelamanchili VS, Singhal M. Dilated Cardiomyopathy. In: StatPearls [Internet]. Treasure Island (FL): StatPearls Publishing; 2021 Jan–. PMID: 28722940.

Markl M, Frydrychowicz A, Kozerke S, Hope M, Wieben O. 4D flow MRI, J Magn Reson Imaging. 2012; 36(5):1015-36.

Markl M, Harloff A, Bley TA, Zaitev M, Jung B, Weigang E, Langer M, Hennig J, Frydrychowicz A. Time-resolved 3D MR velocity mapping at 3T: improved navigator-gated assessment of vascular anatomy and blood flow. J Magn Reson Imaging. 2007; 25(4):824-831.

Markl M, Kilner PJ, Ebbers T. Comprehensive 4D velocity mapping of the heart and great vessels by cardiovascular magnetic resonance. J Cardiovasc Magn Reson. 2011 14;13(1):7.

Mazzi V, Gallo D, Calò K, Njafi M, Khan MO, De Nisco G, Steinman DA, Morbiducci U. A Eulerian method to analyze wall shear stress fixed points and manifolds in cardiovascular flows. Biomech Model Mechanobiol 2020 Oct;19(5):1403-1423

McNally EM, Mestroni L. Dilated Cardiomyopathy: Genetic Determinants and Mechanisms. Circ Res 2007; 121(7):731-748.

Mery D. BALU: A Matlab toolbox for computer vision, pattern recognition and image processing. 2011 http://dmery.ing.puc.cl/index.php/balu

Mery D. Computer Vision for X-Ray Testing: Imaging, Systems, Image Databases, and Algorithms, Springer (1st ed) 2015

Nett EJ, Johnson KM, Frydrychowicz A, Munoz del Rio A, Schrauben E, Francois CJ, Weiben O. Four-dimensional phase contrast MRI with accelerated dual velocity enconding. J Magn Reson Imaging. 2012;35(6):1462-71.

O'Brien, Dropping Highly Collinear Variables from a Model: Why it Typically is Not a Good Idea. Social Science Quarterly. 2017,98:360-75

Pape LA., Tsai TT., Isselbacher EM., Oh JK., Gara PTO., Evangelista A., et al. Aortic Diameter > 5.5 cm Is Not a Good Predictor of Type A Aortic Dissection Observations From the International Registry of Acute Aortic Dissection (IRAD). Circulation 2007; 116:1120–7. Doi: 10.1161/CIRCULATIONAHA.107.702720.

Pasipoularides A. Clinical-pathological correlations of BAV and the attendant thoracic aortopathies. Part 1: Pluridisciplinary perspective on their hemodynamics and morphomechanics. J Mol Cell Cardiol. 2019; 133:223-232. doi: 10.1016/j.yjmcc.2019.05.017

Pedrizzetti G, La Canna G, Alfieri O, Tonti G. The vortex—an early predictor of cardiovascular outcome? Nat Rev Cardiol 2014; 11(9):545-53.

Pelc NJ, Bernstein MA, Shimakawa A, Glover GH, Encoding strategies for three-direction phase-contrast MR imaging of flow, Journal of Magnetic Resonance Imaging. J Magn Reson Imaging. 1991;1(4), 405-413

Rodríguez-Palomares J, Dux-Santoy L, Guala A, et al. Aortic Flow patterns and wall shear stress maps by 4D-flow cardiovascular magnetic resonance in the assessment of aortic dilatation in bicuspid aortic valve disease.J Cardiovasc Magn Reson. 2018 Apr 26;20(1):28. doi:/10.1186/s12968-018-0451-1

Schaefer BM, Lewin MB, Stout KK, Gill E, et al. The bicuspid aortic valve: an integrated phenotypic classification of leaflet morphology and aortic root shape. Heat. 2008; 94:1634-1638

Schnell S, Ansari SA, Wu C, Garcia J, Murphy IG, Rahman OZ, Rshsepar AA, Aristova M, Collins JD, Carr JC, and Markl M, Accelerated Dual-VENC 4D flow MRI for neurovascular applications, J Magn Reson Imaging. 2017; 46(1): 102-114.

Siu SC, Silversides CK. Bicuspid aortic valve disease. J Am Coll Cardiol 2010;22;55(25):2789-800. doi: 10.1016/j.jacc.2009.12.068

Sjöberg P, Heiberg E, Wingren P, Johansson JR, Malm T, Arheden H, Liuba P, Carlsson M. Decreased Diastolic Ventricular Kinetic Energy in Young Patients with Fontan Circulation Demonstrated by Four-Dimensional Cardiac Magnetic Resonance Imaging. Pediatr Cardiol 2017; 8(4): 669-680.

Sotelo J, Dux-Santoy L, Guala A, et al. 3D axial and circumferential wall shear stress from 4D flow MRI data using a finite element method and a laplacian approach. Magn Reson Med 2018 May;79(5):2816-2823. 10.1002/mrm.26927

Sotelo J, Dux-Santoy L, Guala A, et al. Comprehensive analysis of Hemodynamic parameters in patients with bicuspid aortic valve using 4D Flow data and a finite element method, 2018. ISMRM annual meeting, Jun 16-21th, Paris, France.

Sotelo J, Dux-Santoy L, Guala A, Rodríguez-Palomares J, Evangelista A, Sing-Long C, Urbina J, Mura J, Hurtado D, Uribe S. 3D axial and circumferential wall shear stress from 4D Flow MRI data using a finite element method and a laplacian approach. Magn Reson Med. 2018; 79(5):2816-2823.

Sotelo J, Urbina J, Valverde I, et al. 3D Quantification of Wall Shear Stress and Oscillatory Shear Index Using a Finite-Element Method in 3D CINE PC-MRI Data of the Thoracic Aorta. IEEE Trans Med Imaging. 2016 Jun;35(6):1475-87. doi: 10.1109/TMI.2016.2517406. Epub 2016 Jan 14. PMID: 26780787

Sotelo J, Urbina J, Valverde I, Irarrázaval P, Hurtado D, Uribe S. Quantification of wall shear stress using a finite-element method in multidimensional phase-contrast MR data of the thoracic aorta. J Biomech. 2015 16;48(10):1817-27.

Sotelo J, Urbina J, Valverde I, Tejos C, Andia M, Hurtado D, Uribe S. Three-dimensional quantification of vorticity and helicity from 3D cine PC-MRI using finite-element interpolations. Magn Reson Med. 2018; 79(1):541-553.

Sotelo J, Urbina J, Valverde I, Tejos J, Irarrazaval P, Andia M, Uribe S, Hurtado D. 3D Quantification of Wall Shear Stress and Oscillatory Shear Index Using a Finite-Element Method in 3D CINE PC-MRI Data of the Thoracic Aorta. IEEE Trans Med Imaging 2016; 35(6):1475-87.

Sotelo J.4D-Flow-Matlab-Toolbox. 2021 https://github.com/JulioSoteloParraguez/4D-Flow-Matlab-Toolbox

Soulat G, Scott MB, Allen BD, et al., Association of Regional Wall Shear Stress and Progressive Ascending Aorta Dilation in Bicuspid Aortic Valve. JACC Cardiovasc Imaging. 2021 Aug 11; S1936-878X(21)00510-6. doi: 10.1016/j.jcmg.2021.06.020.

Stadler A, Schima W, Ba-Ssalamah A, Kettenbach J, Eisenhuber E. Artifacts in body MR imaging: their appearance and how to eliminate them. Eur Radiol. 2007; 17:1242-1255

Stalder AF, Russe MF, Frydrychowicz A, Bock J, Henning J, Markl M. Quantitative 2D and 3Dphase contrast MRI: Optimized analysis of blood flow and vessel wall parameters. Magn Reson Med. 2008; 60(5):1218-1231.

Stoll V, Hess A, Rodgers C, Bissell M, Dyverfeldt P, Ebbers T, Myerson SG, Carlhäll C-J, Neubauer S. Left Ventricular Flow Analysis: Novel Imaging Biomarkers and Predictors of Exercise Capacity in Heart Failure. Circ Cardiovasc Imaging. 2019 May;12(5): e008130.

Suwa K, Saitoh T, Takehara Y, Sano M, Saotome M, Urushida T, Katoh H, Satoh H, Sugiyama M, Wakayama T, Alley M, Sakahara H, Hayashi H. Intra-left ventricular flow dynamics in patients with preserved and impaired left ventricular function: Analysis with 3D cine phase contrast MRI (4D-Flow). J Magn Reson Imaging, 2016; 44(6):1493-1503.

Svalbring E, Fredriksson A, Eriksson J, Dyverfeldt P, Ebbers T, Bolder AF, Engvall J, Carlhäll C-J. Altered Diastolic Flow Patterns and Kinetic Energy in Subtle Left Ventricular Remodeling and Dysfunction Detected by 4D Flow MRI. PLoS One 2016; 11(8):e0161391.

Tan L, McLaughlin R, Lim E, et al. Fully automated segmentation of the left ventricle in cine cardiac MRI using neural network regression. J Magn Reson Imaging. 2018 Jul;48(1):140-152. doi: 10.1002/jmri.25932

Tao Q, Yan W, Wang Y, et al. Deep Learning-based Method for Fully Automatic Quantification of Left Ventricle Function from Cine MR Images: A Multivendor, Multicenter Study, Radiology. 2019, 290(1):81-88.

Töger J, Kanski M, Carlsson M, Kovács SJ, Söderlind G, Arheden H, Heiberg E. Vortex ring formation in the left ventricle of the heart: analysis by 4D Flow MRI and Lagrangian coherent structures. Ann Biomed Eng 2012;40(12):2652-62.

Tufvesson J, Hedstrom E, Steding-Ehrenborg K, Carlsson M, Arheden H, Heiberg E. Validation and Development of a New Automatic Algorithm for Time-Resolved Segmentation of the Left Ventricle in Magnetic Resonance Imaging, Biomed Res Int 2015; 2015;970357.

Uribe S, Beerbaum P, Sørensen TS, Rasmusson A, Razavi R, Schaeffter T. Four-dimensional (4D) flow of the whole heart and great vessels using real-time respiratory selft-gating. Magn Reson Med. 2009;62(4):984-92.

van der Maaten L, Hinton G. Visualizing Data using t-SNE, Journal of Machine Learning Research, 2008, 9(86):2579-2605.

Wall ME, Rechtsteiner A, Rocha LM. Singular value decomposition and principal component analysis In: Berrar DP, Dubitzky, Granzow M (eds). A Practical Approach to Microarray Data Analysis. Springer, Boston, MA. 2003, 91-109.

Wigstrom L, Ebbers T, Fyrenius A, Karlsson M, Engvall J, Wranne B, Bolger AF. Particle trace visualization of intracardiac flow using time-resolved 3D phase contrast MRI. Magn Reson Med. 199; 41(4):793-799.

Witten I and Frank E, Data mining: practical machine learning tools and techniques, San Mateo (2nd ed.), 2005

Wojnarski C, Roselli E, Idrees J, et al. Machine-learning phenotypic classification of bicuspid aortopathy, J Thorac Cardiovasc Surg. 2018 Feb;155(2):461-469.e4. doi: 10.1016/j.jtcvs.2017.08.123

Wong KK, Kelso RM, Worthley SG, Sanders P, Mazumdar J, Abbott D. Cardiac flow analysis applied to phase contrast magnetic resonance imaging of the heart. Ann Biomed Eng 2009;37(8):1495-515.

Wong M, Staszewsky L, Latini R, Barlera S, Glazer R, Aknay N, Hester A, Anand I, Cohn JN. Severity of left ventricular remodeling defines outcomes and response to therapy in heart failure: Valsartan heart failure trial (Val-HeFT) echocardiographic data. J Am Coll Cardiol 2004;43(11):2022-7.

Wu SP, Ringgaard S, Pedersen EM, Three-dimensional phase contrast velocity mapping acquisition improves wall shear stress estimation in vivo. Magn Reson Imaging. 2004; 22(3):345-351.

Yang GZ, Burger P, Kilner PJ, Karatowski SP, Firmin DN. Dynamic range extension of cine velocity measurements using motion-registered spatiotemporal phase unwrapping. J Magn Reson Imaging. 1996; 6(3): 495-502.

Zajac J, Eriksson J, Dyverfeldt P, Bolder AF, Carlhäll C-J. Turbulent kinetic energy in normal and myopathic left ventricles. J Magn Reson Imaging; 2015; 41(4):1021-9

Zwart NR, Pipe JG. Multidirectional High-Moment Encoding in Phase Contrast MRI. Magn Reson Med. 2013. 69:1553-1564.

APPENDIX

A. APPENDIX FOR PUBLICATION I

A.1. Variance Analysis of the ODV Method

In order to calculate the statistical properties of u_*, in the ODV method, we first need to obtain a closed expression for (an approximation of) it. Indeed, since the global minimum is also a local minimum, we calculated u_* using the fact that the solution is a local minimum of the cost function. Namely, we search for $J'_{dual}(u_*) = 0$, with

$$\begin{aligned} J'_{dual}(u_*) &= -\frac{\pi}{VENC_h}\sin\left(\frac{\pi}{VENC_h}(u_H - u_*)\right) - \frac{\pi}{VENC_l}\sin\left(\frac{\pi}{VENC_l}(u_L - u_*)\right) \\ &= -\frac{\pi}{VENC_h}\sin\left(\frac{\pi}{VENC_h}(u_H - u_* + 2k_H VENC_H)\right) - \frac{\pi}{VENC_l}\sin\left(\frac{\pi}{VENC_l}(u_L - u_* + 2k_L VENC_L)\right) = 0 \end{aligned} \tag{A.1}$$

In consequence, we can approximate the sin-terms by its arguments leading to:

$$u_* \approx (VENC_H^{-2} + VENC_L^{-2})^{-1}\left(u_H VENC_H^{-2} + u_L VENC_L^{-2} + 2(k_H VENC_H^{-1} + k_L VENC_L^{-1})\right) \tag{A.2}$$

Note first that the phases φ_0, φ_H, and φ_L are statistically independent with an expected value of $E[\varphi_i] = E[\varphi_o] + \frac{\overline{u_i}}{d_i}\pi$, where I = H,L are related to velocities acquired with high and low VENCs. As a consequence, u_H and u_L are statistically dependent because both VENC images share the background phase. Therefore, the variance of u_* (equation A.2) has the form,

$$\begin{aligned} Var(u_*) &= (VENC_H^{-2} + VENC_L^{-2})^{-2}(Var(u_H)VENC_H^{-4} + Var(u_L)VENC_L^{-4} + 2VENC_H^{-2}VENC_L^{-2}Cov(u_H,u_L)) \\ &= (VENC_H^{-2} + VENC_L^{-2})^{-2}\left(2\sigma_\varphi^2 VENC_H^{-2} + 2\sigma_\varphi^2 VENC_L^{-2} + 2VENC_H^{-2}VENC_l^{-2}Cov(u_H,u_L)\right) \\ &= \left(\frac{VENC_H^2 VENC_L^2}{VENC_H^2 + VENC_L^2}\right)^2 \left(2\sigma_\varphi^2 VENC_H^{-2} + 2\sigma_\varphi^2 VENC_L^{-2} + 2VENC_H^{-2}VENC_L^{-2}Cov(u_H,u_L)\right) \end{aligned}$$

$$= 2\sigma_\varphi^2(VENC_H^{-2} + VENC_L^{-2})\left(\frac{VENC_H^2 VENC_L^2}{VENC_H^2 + VENC_L^2}\right)^2 + 2VENC_H^{-2}VENC_L^{-2}\left(\frac{VENC_H^2 VENC_L^2}{VENC_H^2 + VENC_L^2}\right)^2 Cov(u_H, u_L)$$

$$= 2\sigma_\varphi^2 \frac{VENC_H^2 VENC_L^2}{VENC_H^2 + VENC_L^2} + 2\frac{VENC_H^2 VENC_L^2}{(VENC_H^2 + VENC_L^2)^2} Cov(u_H, u_L)$$

$$= \frac{Var(u_H)}{1+\beta^2} + \frac{2VENC_H^2 VENC_L^2}{(VENC_H^2 + VENC_L^2)^2} Cov(u_H, u_L)$$

$$= \frac{Var(u_H)}{1+\beta^2} + \frac{2VENC_H^2 VENC_L^2}{(VENC_H^2 + VENC_L^2)^2} E[(u_H - Eu_H)(u_L - Eu_L)]$$

$$= \frac{Var(u_L)}{1+\beta^2} + \frac{2VENC_H^2 VENC_{L2}^2}{(VENC_H^2 + VENC_L^2)^2}\left(E\left[\left(\frac{\varphi_H - \varphi_o}{\pi} VENC_H\right)\left(\frac{\varphi_L - \varphi_o}{\pi} VENC_L\right)\right] - \overline{u_H u_L}\right)$$

$$= \frac{Var(u_L)}{1+\beta^2} + \frac{2VENC_H^2 VENC_L^2}{(VENC_H^2 + VENC_L^2)^2}\left(\frac{VENC_H VENC_L}{\pi^2}(E[\varphi_0^2] - E[\varphi_0]^2)\right)$$

$$= \frac{Var(u_L)}{1+\beta^2} + \frac{2VENC_H VENC_L}{(1+\beta^2)\pi^2} Var(\varphi_0)$$

$$= \frac{Var(u_L)}{1+\beta^2}\left(1 + \frac{\beta}{(1+\beta^2)}\right) \quad \text{(A.3)}$$

For this calculation, we considered $Var(\varphi_0) = \pi^2\sigma_\varphi^2$, $Var(u_L) = 2\sigma_\varphi^2 VENC_L^2$, and $Var(u_H) = 2\sigma_\varphi^2 VENC_H^2$. Note that the covariance is defined as the expected value of the product of their deviations from their individual expected values $Cov(u_H, u_L) = E[(u_H - Eu_H)(u_L - Eu_L)]$ and the expression for the variance e.g., for the φ_0 can be expanded as, $Var(\varphi_0) = E[(\varphi_0 - E[\varphi_0])^2] = E[\varphi_0^2 - 2\varphi_0 E[\varphi_0] + E[\varphi_0]^2] = E[\varphi_0^2] - 2E[\varphi_0]E[\varphi_0] + E[\varphi_0]^2 = E[\varphi_0^2] - E[\varphi_0]^2$
.

Now we want to calculate the β values ($VENC_L = \beta VENC_H$, $0 < \beta < 1$) such that the variance of the result with the ODV method is equal to or lower than the low VENC image, i.e., $Var(u_*) \leq Var(u_L)$,

$$Var(u_*) = \frac{Var(u_L)}{1+\beta^2}\left(1 + \frac{\beta}{(1+\beta^2)}\right) \leq Var(u_L) \quad \text{(A.4)}$$

Equation (A.3) becomes

$$\beta^4 + \beta^2 - \beta \geq 0 \tag{A.5}$$

We could find the solutions for equation (A.5), factorizing by β and using the zero-factor theorem for $\beta \neq 0$,

$$\beta^3 + \beta - 1 \geq 0 \tag{A.6}$$

Therefore, an improved estimate in terms of variance is obtained,

$$\frac{Var(u_L)}{1+\beta^2}\left(1 + \frac{\beta}{(1+\beta^2)}\right) \leq Var(u_H), \text{ if } \beta \geq 0.682 \tag{A.7}$$

A.2. Supplementary Material

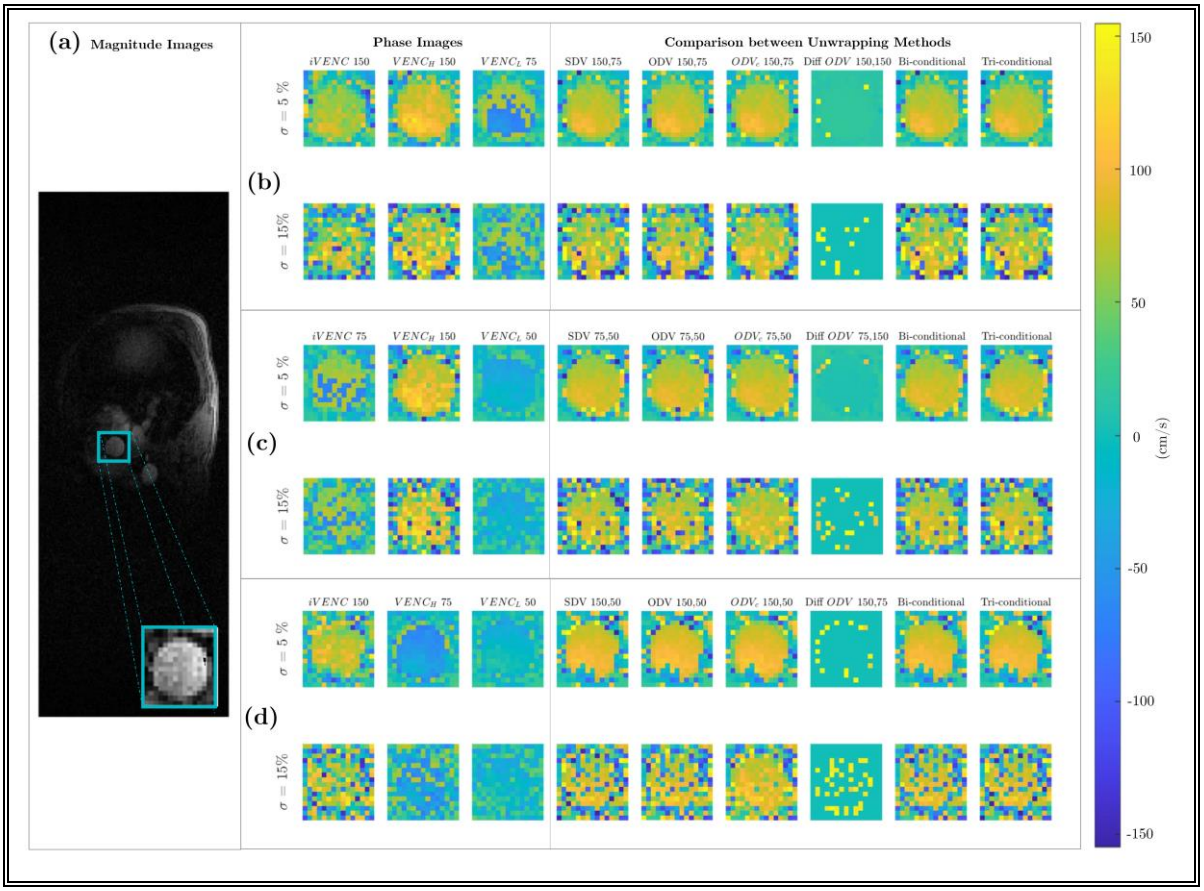

Figure A.1. Ascending aorta at peak systole of a representative volunteer (same as Figure 2). (a) Magnitude Images: slice prescription and region-of-interest. Phase-differences images with VENCs combination of (b) (iVENC, $VENC_H$, $VENC_L$) = (150, 150, 75), (c) (iVENC, $VENC_H$, $VENC_L$) = (75, 150, 50) cm/s and (d) (iVENC, $VENC_H$, $VENC_L$) = (150, 75, 50) cm/s with different levels of synthetic noise,σ. The VENCs used by the SDV and ODV methods are in the top part of the figures. First column: iVENC, second column: $VENC_H$, third column $VENC_L$, fourth column: SDV, fifth column: ODV, sixth column: ODV corrected, seventh column: Different between the ODV and ODC corrected method, eighth column: bi-conditional, and ninth column: tri-conditional methods.

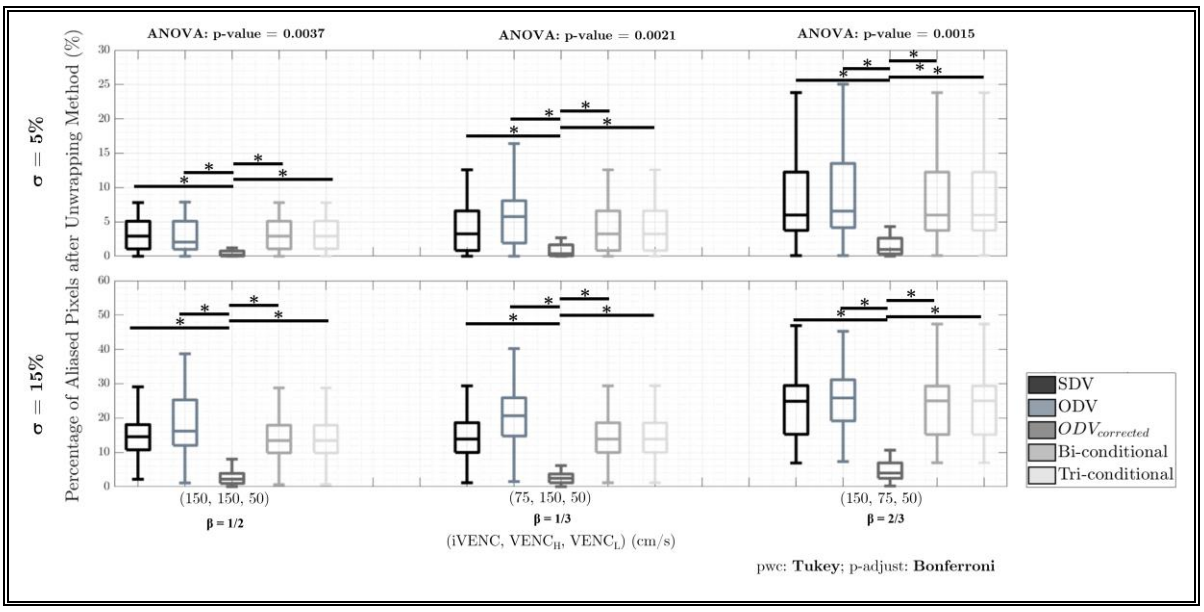

Figure A.2. Box whisker plots for the evaluation of unwrapping methods of the volunteers at peak-systole in the ascending aorta with different levels of synthetic noise, σ, with VENCs combination of (first column) (iVENC, $VENC_H$, $VENC_L$) = (150, 150, 75) cm/s, (second column) (iVENC, $VENC_H$, $VENC_L$) = (75, 150, 50) cm/s, and (third column) (iVENC, $VENC_H$, $VENC_L$) = (150, 75, 50) cm/s. The SDV and ODV methods used in (first column) ($VENC_H$, $VENC_L$) = (150,75) cm/s β =1/2, (second column) ($VENC_H$, $VENC_L$) = (150, 50) cm/s β = 1/3, and (third column) the SDV (iVENC, $VENC_L$) = (150, 50) cm/s β = 1/3 and the ODV method ($VENC_H$, $VENC_L$) = (75, 50) cm/s β = 2/3. Aliased number of pixels after the unwrapping methods were performed as a percentage. On each box, the central mark is the median, the bottom and top edges of the box are the 25th and 75th percentiles, respectively, and the whiskers extend to the most extreme data points not considered outliers. The significance of the interaction between noise levels and the unwrapping method for the different VENCs combinations is in the top part of the figures with their p-values. The symbol * indicates statistically significant differences ($p < 0.05$).

B. APPENDIX FOR PUBLICATION II

B.1. Intra- and Inter-Observer Reproducibility

As shown in Figure B.1, excellent intra-observer agreement with minimal mean differences and small limits of agreement were found for peak systole. Mean differences were: velocity magnitude −0.0003 ± 0.0118 m/s, kinetic energy (−0.4580 ± 0.7490) × 10−9 J, vorticity magnitude 0.0029 ± 0.0249 1/s, helicity density (−0.0978 ± 0.5345) × 10−3 m/s^2, viscous dissipation −0.0070 ± 0.0578 $1/s^2$, and energy loss (−0.0124 ± 0.2563) × 10^{-9} W. Similar results were obtained at e-wave and end-diastole, as shown in Figures B.2 and B.3, respectively. Figure B.4 demonstrates excellent inter-observer analysis agreement for peak systole. Mean differences were: velocity magnitude −0.0024 ± 0.0124 m/s, kinetic energy (−0.0349 ± 0.1093) × 10^{-5} J, vorticity magnitude 0.1122 ± 0.7634 1/s, helicity density −0.0001 ± 0.0139 m/s^2, viscous dissipation −2.1652 ± 11.8205 $1/s^2$, and energy loss (0.0012 ± 0.3008) × 10^{-8} W. Figures B.5 and B.6 show the results obtained at e-wave and end-diastole, respectively, with comparable results at peak systole.

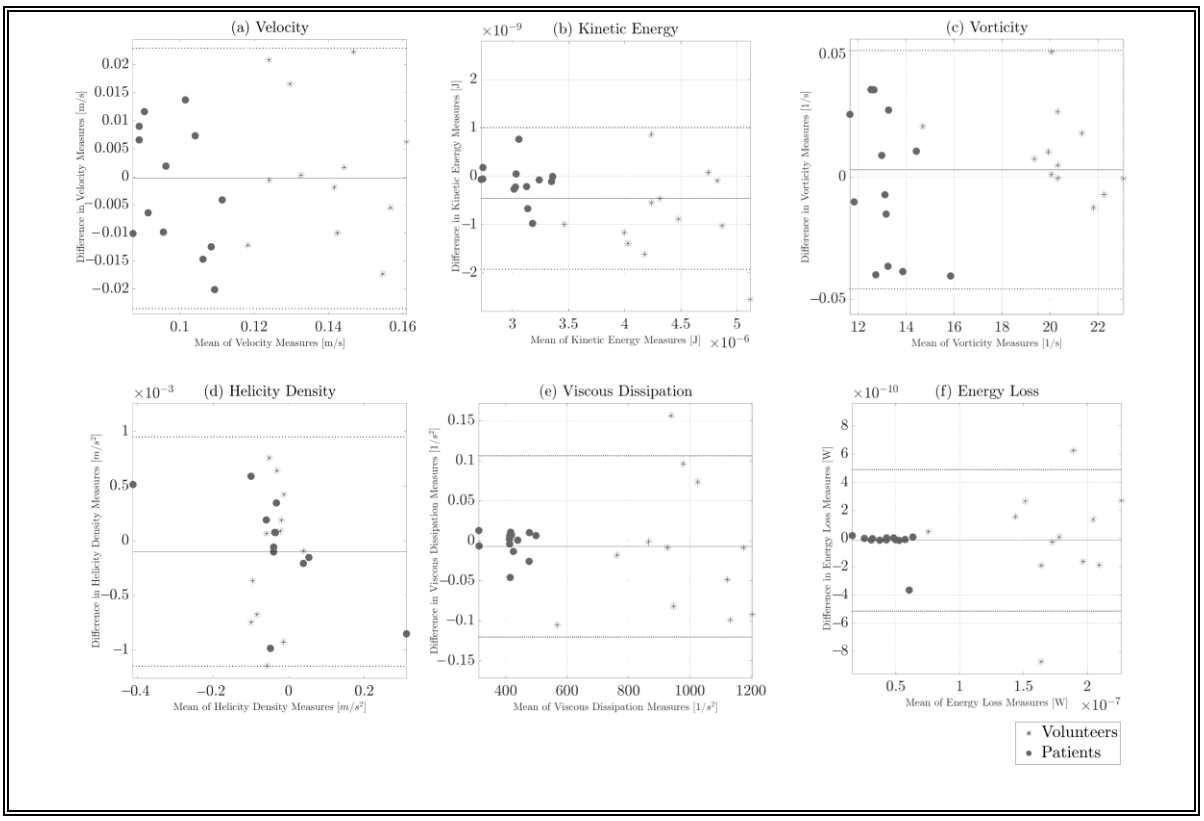

Figure B.1. Bland-Altman plots represent the intra-observer reproducibility in the measurements of LV global hemodynamic parameters (**a**–**f**) at peak systole. The thick line represents the mean difference, and the thin lines represent the limits agreement (1.96 SD).

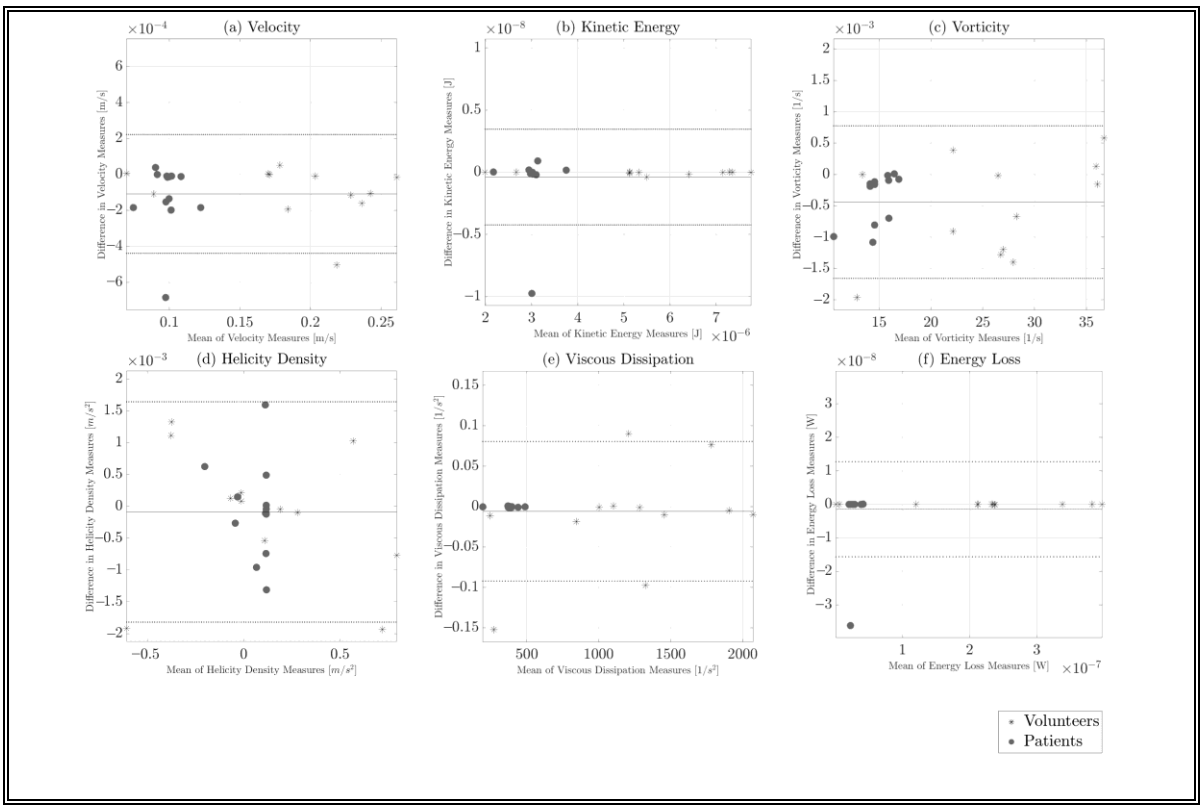

Figure B.2. Bland-Altman plots represent the intra-observer reproducibility in the measurements of LV global hemodynamic parameters (**a**–**f**) at e-wave. The thick line represents the mean difference, and the thin lines represent the limits agreement (1.96 SD).

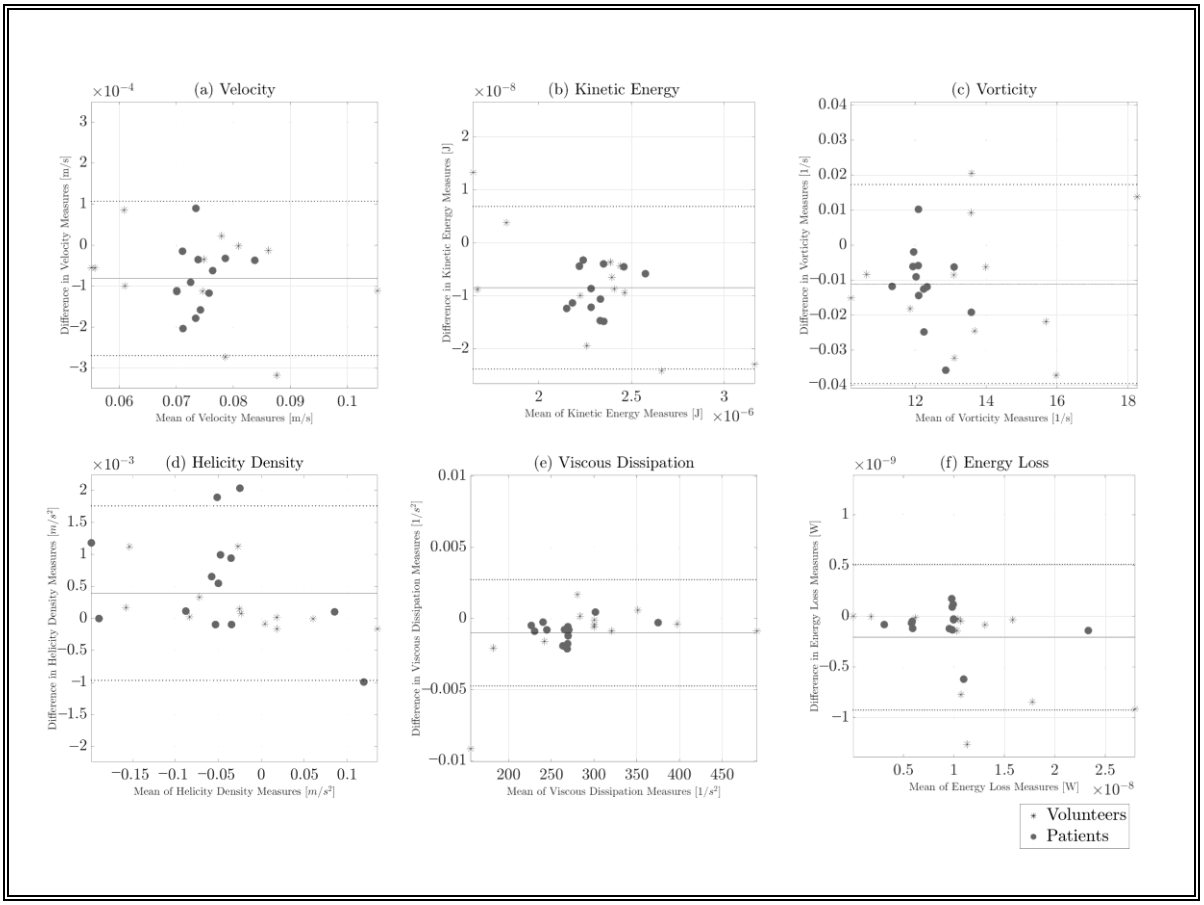

Figure B.3. Bland-Altman plots represent the intra-observer reproducibility in the measurements of LV global hemodynamic parameters (**a**–**f**) at end-diastole. The thick line represents the mean difference, and the thin lines represent the limits agreement (1.96 SD).

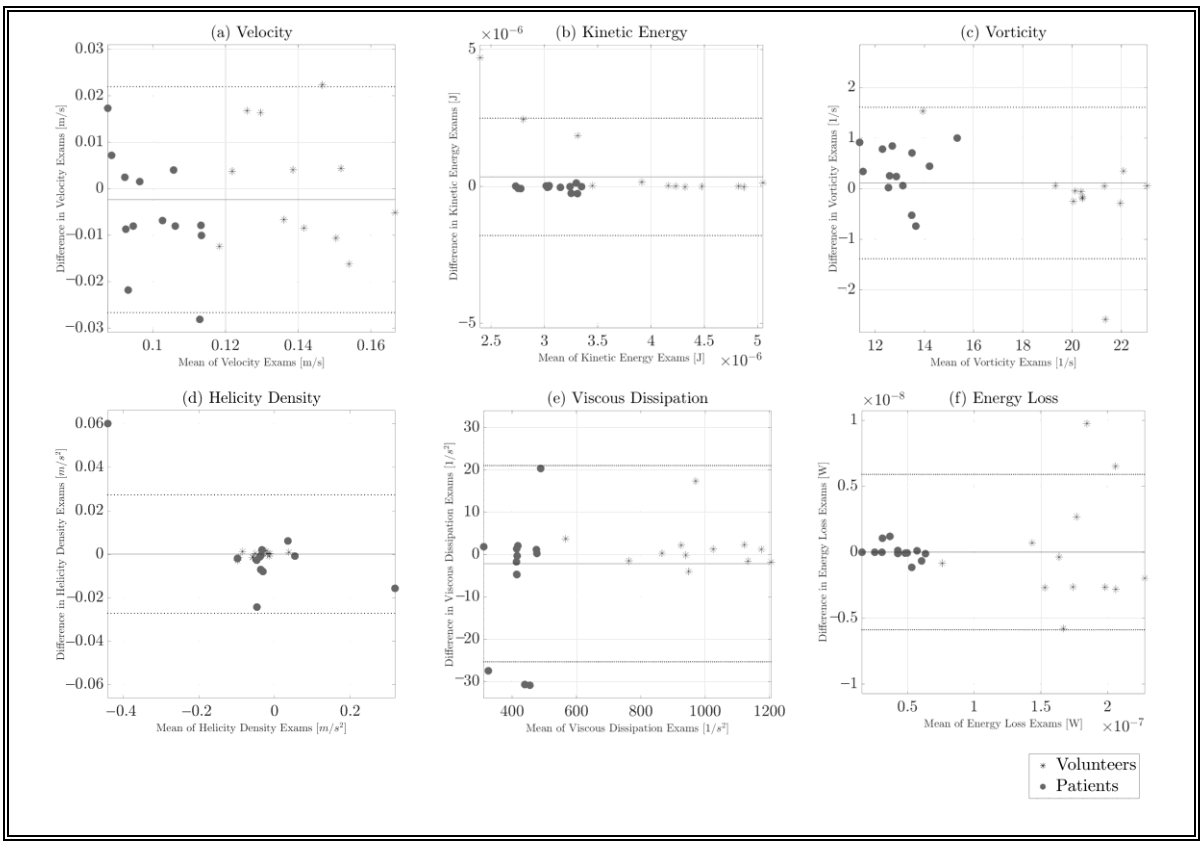

Figure B.4. Bland-Altman plots represent the inter-observer reproducibility in the exams of LV global hemodynamic parameters (**a**–**f**) at peak systole. The thick line represents the mean difference, and the thin lines represent the limits agreement (1.96 SD).

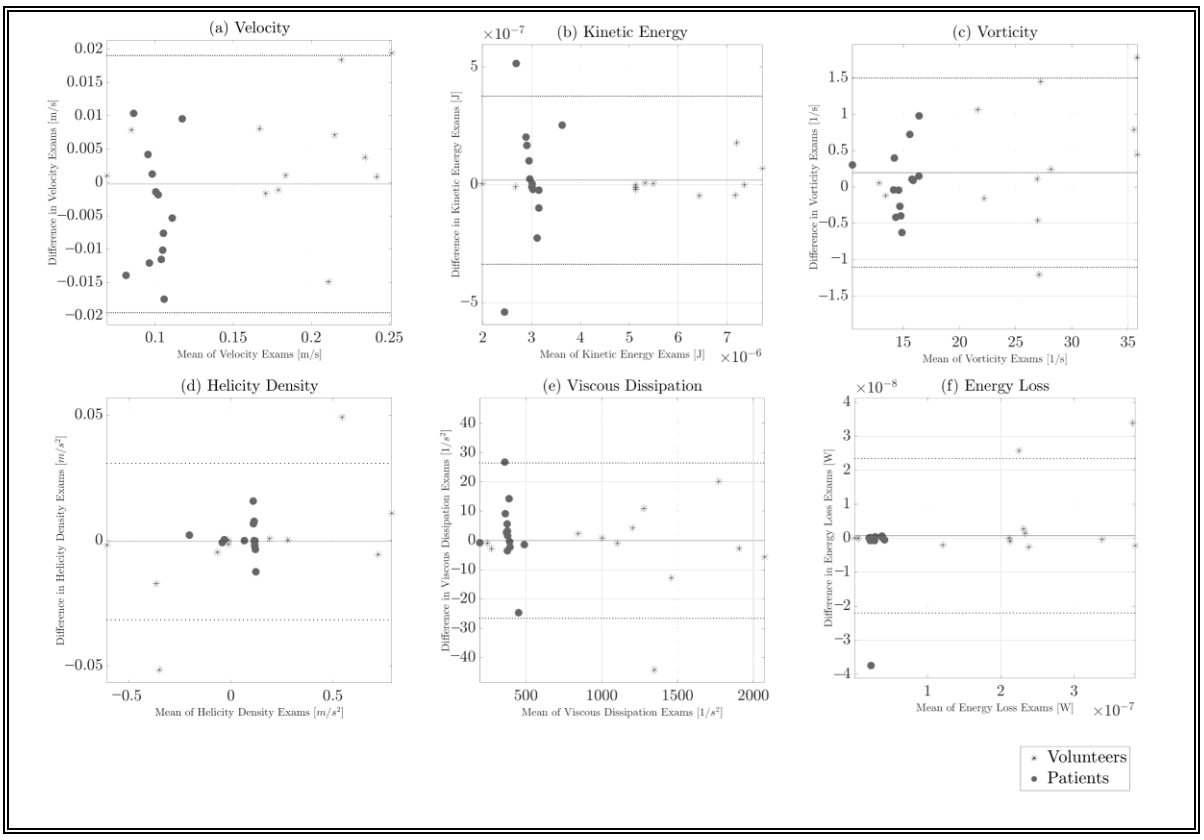

Figure B.5. Bland-Altman plots represent the inter-observer reproducibility in the exams of LV global hemodynamic parameters (**a**–**f**) at e-wave. The thick line represents the mean difference, and the thin lines represent the limits agreement (1.96 SD).

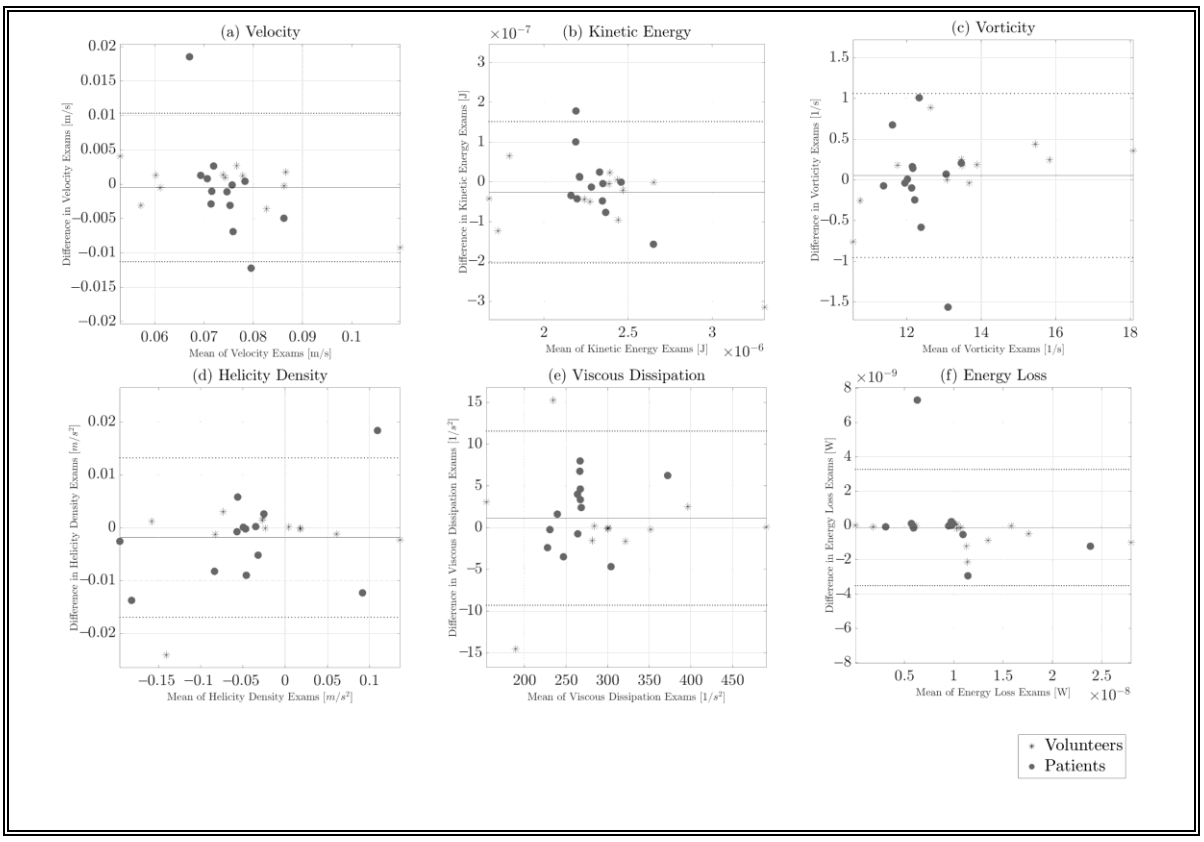

Figure B.6. Bland-Altman plots represent the inter-observer reproducibility in the exams of LV global hemodynamic parameters (**a**–**f**) at end-diastole. The thick line represents the mean difference, and the thin lines represent the limits agreement (1.96 SD).

B.2 Supplementary Material

Table B.1. Equations used to calculate each hemodynamic parameter

Parameter name	Equation	Description
Kinetic energy (J)	$KE = \frac{1}{2}\rho V\lvert v\rvert^2$	Where ρ is the density (1060 kg/m^3), V is the Voronoi volume around each node, and v is the velocity vector.
Vorticity (1/s)	$\omega = \nabla \times v$	operator $\nabla \times$ is the curl of the velocity vector v.
Helicity Density (m/s^2)	$Hd = v \cdot \omega$	v is the velocity vector. ω is the vorticity.
Viscous Dissipation (1/s^2)	$\phi_v = \frac{1}{2}\sum_i\sum_j\left[\left(\frac{\partial v_i}{\partial x_j}+\frac{\partial v_j}{\partial x_i}\right)-\frac{2}{3}(\nabla \cdot v)\delta_{ij}\right]^2$	v is the velocity vector. i, j are the component of the vector v (directions x, y, z). δ_{ij} is the identity matrix.
Energy Loss (W)	$EL = \mu\phi_v V$	μ is the viscosity (4.5 cP). V is the Voronoi volume around each node

Table B.2. Mean parameter values across 16 segments of the LV, during peak systole. Where bold type means statistically significant between volunteers and patients ($p < 0.05$). υ: Velocity Magnitude, ω: vorticity magnitude, H_d: helicity density, VD: viscous dissipation, EL: energy loss, and K: kinetic energy.

Segmental Area	LV Segment	Group	Peak Systole					
			v (m/s)	ω (1/s)	H_d (m/s²)	VD (k 1/s²)	EL (μW)	K × 10-⁴ (J)
Basal	1	V	0.18	21.72	0.41	1.29	0.26	0.05
		P	0.07	11.31	0.03	0.24	0.01	0.02
	2	V	**0.12**	**18.00**	-0.01	0.77	0.11	**0.03**
		P	**0.06**	**10.75**	0.08	0.28	0.02	**0.02**
	3	V	0.13	24.77	0.17	1.20	0.23	0.04
		P	0.11	21.39	-0.01	0.79	0.10	0.04
	4	V	**0.37**	40.67	-3.17	3.49	0.80	**0.11**
		P	**0.35**	33.01	-0.55	2.3	0.51	**0.10**
	5	V	**0.19**	32.45	0.44	2.33	0.53	**0.06**
		P	**0.18**	23.97	0.38	1.12	0.16	**0.05**
	6	V	0.11	21.65	-0.08	1.05	0.20	0.03
		P	0.07	13.43	0.06	0.28	0.01	0.02
Mid-cavity	7	V	**0.11**	14.68	0.13	0.48	0.04	**0.03**
		P	**0.06**	9.03	-0.06	0.15	0.00	**0.02**
	8	V	0.11	15.88	-0.14	0.49	0.03	0.03
		P	0.06	9.52	0.13	0.15	0.00	0.02
	9	V	**0.13**	**17.31**	-0.40	0.65	**0.07**	**0.04**
		P	**0.11**	**15.11**	0.39	0.41	**0.02**	**0.03**
	10	V	**0.19**	24.29	-1.99	1.07	0.17	**0.06**
		P	**0.19**	20.79	0.69	0.76	0.07	**0.06**
	11	V	**0.14**	23.14	-0.89	0.93	**0.16**	**0.04**
		P	**0.13**	17.74	-0.14	0.56	**0.04**	**0.04**
	12	V	0.10	16.23	0.15	0.54	0.07	0.03
		P	0.06	10.89	-0.17	0.24	0.01	0.02
Apical	13	V	**0.07**	10.11	-0.23	0.20	**0.00**	**0.02**
		P	**0.05**	7.36	-0.10	0.10	**0.00**	**0.01**
	14	V	**0.06**	9.19	-0.17	0.16	**0.00**	**0.02**
		P	**0.04**	6.13	-0.04	0.10	**0.00**	**0.01**
	15	V	0.08	10.66	-0.32	0.21	**0.00**	0.02
		P	0.07	9.60	0.17	0.15	**0.00**	0.02
	16	V	**0.08**	11.25	-0.37	0.25	0.00	**0.02**
		P	**0.08**	9.15	0.05	0.18	0.01	**0.02**

Table B.3. Mean parameter values across 16 segments of the LV, during e-wave. Where bold type means statistically significant between volunteers and patients ($p < 0.05$). υ: Velocity Magnitude, ω: vorticity magnitude, H_d: helicity density, VD: viscous dissipation, EL: energy loss, and K: kinetic energy.

Segmental Area	LV Segment	Group	E - Wave					
			υ (m/s)	ω (1/s)	H_d (m/s^2)	VD (k 1/s^2)	EL (μW)	K × 10^{-5} (J)
Basal	1	V	0.20	33.46	0.88	1.79	0.36	0.61
		P	0.16	24.96	0.58	0.85	0.13	0.51
	2	V	**0.28**	**35.11**	1.97	1.80	0.33	**0.85**
		P	**0.20**	**29.27**	0.86	1.10	0.16	**0.63**
	3	V	0.31	33.50	1.69	0.53	0.25	0.91
		P	0.17	23.65	0.24	0.64	0.05	0.53
	4	V	**0.27**	36.75	0.74	1.95	0.38	**0.78**
		P	**0.11**	20.90	-0.05	0.50	0.03	**0.34**
	5	V	**0.23**	35.52	-0.10	1.74	0.34	**0.67**
		P	**0.14**	24.07	0.08	0.63	0.05	**0.44**
	6	V	0.19	32.07	-0.06	1.54	0.29	0.58
		P	0.18	25.59	0.28	0.81	0.10	0.56
Mid-cavity	7	V	**0.16**	25.16	0.42	1.16	0.21	**0.49**
		P	**0.09**	14.09	0.21	0.37	0.02	**0.29**
	8	V	0.22	27.96	0.94	1.48	0.26	0.65
		P	0.11	13.83	0.14	0.43	0.03	0.35
	9	V	**0.23**	26.99	0.28	1.27	0.23	**0.68**
		P	**0.11**	14.2	0.02	0.35	0.01	**0.33**
	10	V	**0.18**	28.78	-0.07	1.25	0.23	**0.55**
		P	**0.09**	15.43	-0.12	0.31	0.01	**0.30**
	11	V	**0.13**	24.72	0.07	1.04	0.20	**0.40**
		P	**0.10**	15.01	-0.59	0.33	0.01	**0.31**
	12	V	0.13	23.64	0.11	0.96	0.18	0.41
		P	0.08	13.39	-0.01	0.39	0.03	0.27
Apical	13	V	**0.07**	10.43	0.03	**0.24**	**0.01**	**0.18**
		P	**0.04**	6.63	-0.08	**0.08**	**0.00**	**0.12**
	14	V	**0.08**	**10.88**	-0.09	**0.27**	**0.01**	**0.21**
		P	**0.04**	**6.98**	-0.02	**0.09**	**0.00**	**0.12**
	15	V	0.10	12.68	0.01	0.40	0.03	0.26
		P	0.05	6.56	-0.02	0.09	0.00	0.14
	16	V	**0.08**	**10.38**	0.18	**0.29**	**0.01**	**0.20**
		P	**0.05**	**6.49**	-0.06	**0.09**	**0.00**	**0.16**

Table B.4. Mean parameter values across 16 segments of the LV, during e-wave. Where bold type means statistically significant between volunteers and patients ($p < 0.05$). υ: Velocity Magnitude, ω: vorticity magnitude, H_d: helicity density, VD: viscous dissipation, EL: energy loss, and K: kinetic energy.

Segmental Area	**LV Segment**	**Group**	**End-diastole**					
			v (m/s)	ω (1/s)	H_d (m/s^2)	VD (k $1/s^2$)	EL × 10^{-7} (W)	K × 10^{-5} (J)
Basal	1	V	0.08	14.92	0.21	0.35	0.13	0.24
		P	0.06	12.72	0.13	0.29	0.07	0.20
	2	V	0.09	15.58	0.26	0.37	0.13	0.28
		P	0.06	12.62	0.01	0.29	0.07	0.20
	3	V	0.10	16.82	0.15	0.41	0.19	0.30
		P	0.08	14.50	0.23	0.33	0.14	0.24
	4	V	0.12	20.44	0.00	0.64	0.72	0.35
		P	0.13	19.57	0.07	0.68	0.67	0.39
	5	V	0.09	17.92	-0.06	0.48	0.29	0.27
		P	0.11	19.15	-0.02	0.51	0.33	0.35
	6	V	0.09	15.31	0.14	0.39	0.16	0.26
		P	0.08	14.49	0.07	0.31	0.07	0.25
Mid-cavity	7	V	0.07	13.77	-0.13	0.28	0.03	0.21
		P	0.07	11.12	0.07	0.22	0.02	0.22
	8	V	0.09	14.62	0.07	0.34	0.06	0.29
		P	0.06	10.79	0.09	0.18	0.01	0.20
	9	V	0.09	15.81	-0.11	0.31	0.05	0.28
		P	0.07	12.30	0.12	0.25	0.05	0.23
	10	V	0.08	15.06	0.18	0.30	0.07	0.23
		P	0.11	16.08	0.24	0.37	0.22	0.35
	11	V	0.07	12.99	-0.22	0.27	0.02	0.20
		P	0.09	14.83	-0.32	0.29	0.07	0.28
	12	V	0.06	11.75	-0.06	0.23	0.04	0.17
		P	0.07	11.59	0.15	0.26	0.08	0.22
Apical	13	V	0.04	8.25	-0.11	0.12	0.00	0.12
		P	0.05	7.67	-0.07	0.11	0.00	0.15
	14	V	0.05	9.64	-0.11	0.15	0.00	0.14
		P	0.04	7.36	0.02	0.10	0.00	0.13
	15	V	0.06	9.78	-0.08	0.18	0.00	0.18
		P	0.06	8.98	0.07	0.14	0.00	0.17
	16	V	0.05	8.63	0.01	0.15	0.00	0.14
		P	0.07	8.73	-0.04	0.16	0.00	0.21

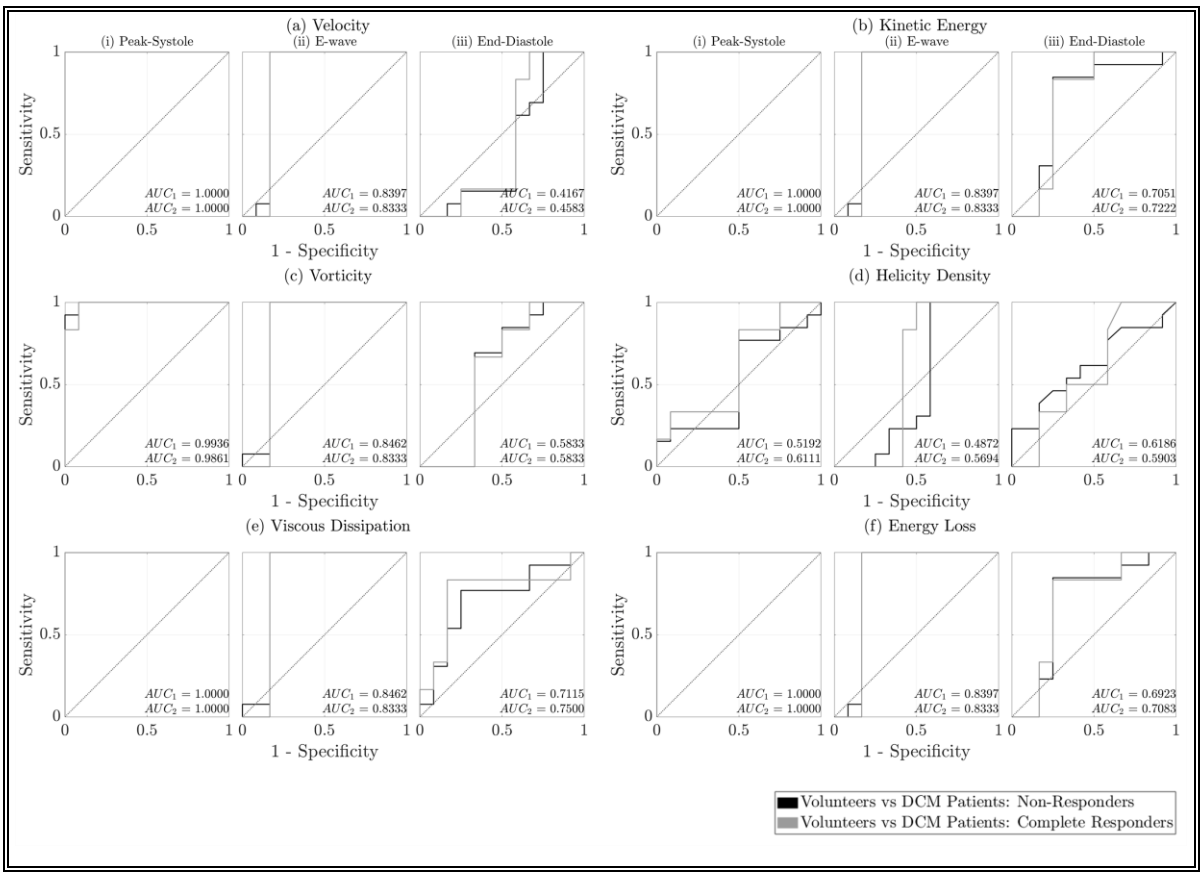

Figure B.7. ROC-curves for hemodynamic parameters (a–f) in the entire LV cavity of the groups of volunteers and patients at peak-systole, e-wave, and end-diastole.

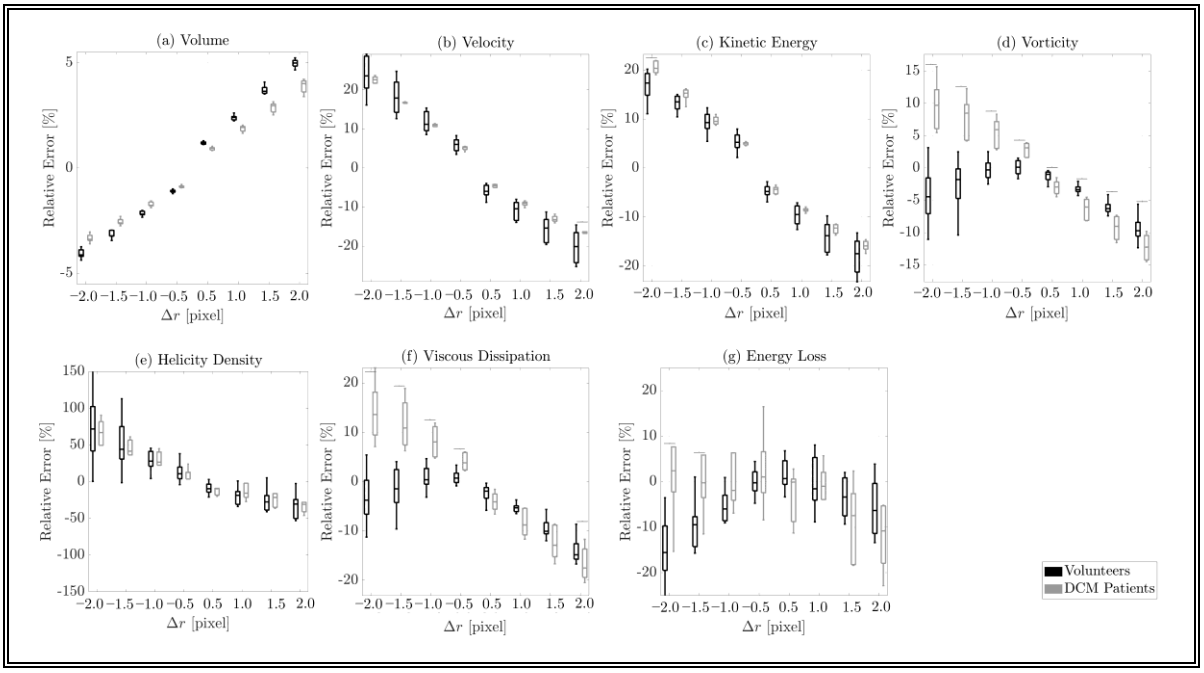

Figure B.8. Relative error values of volume (a) and each hemodynamic parameter (b–g), obtained comparing the reference segmentation with segmentations given by erosion or dilation, for each group of volunteers and patients at e-wave. * indicates statistical significant differences ($p < 0.05$).

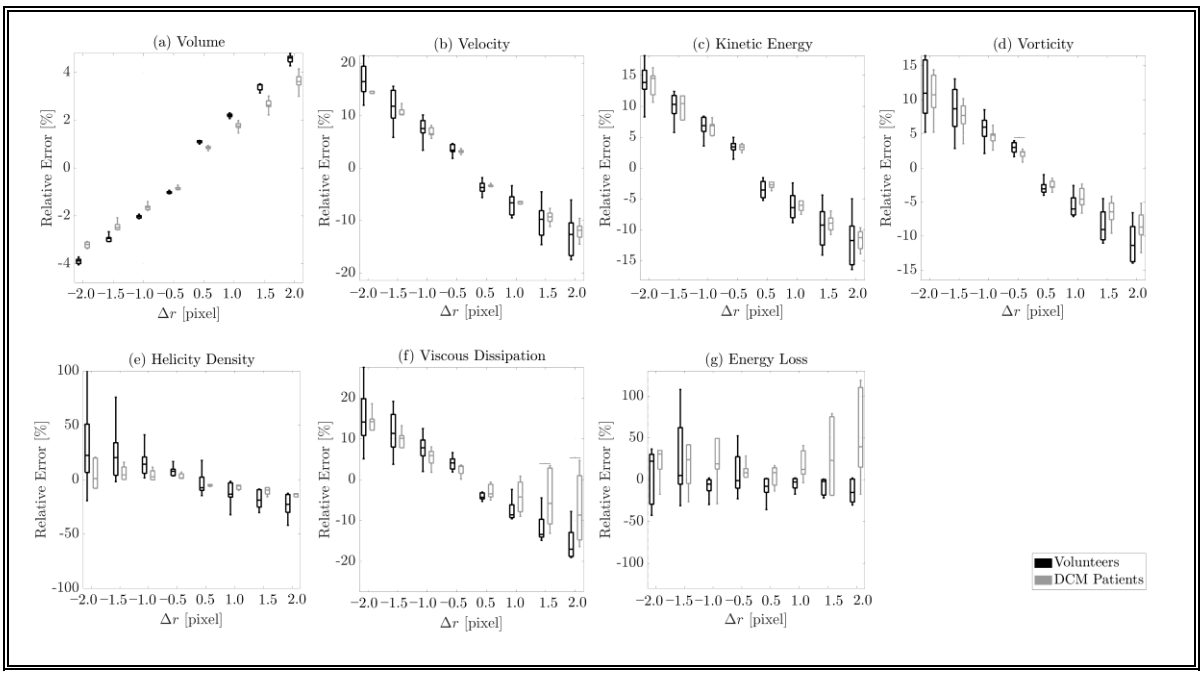

Figure B.9. Relative error values of volume (a) and each hemodynamic parameter (b–g), obtained comparing the reference segmentation with segmentations given by erosion or dilation, for each group of volunteers and patients at end-diastole. * indicates statistical significant differences ($p < 0.05$).

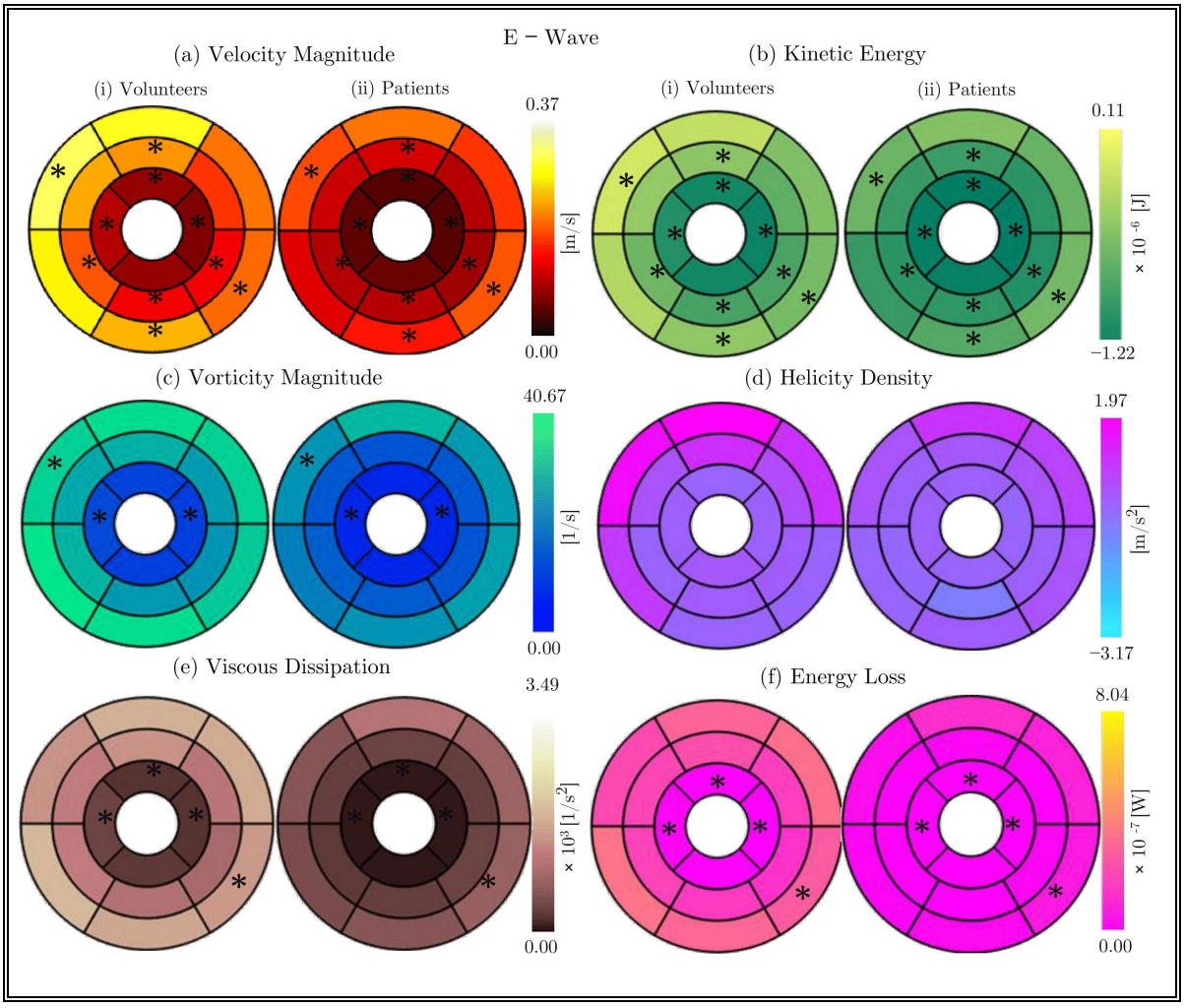

Figure B.10. Bullseye plots of mean hemodynamic parameters (a–f), across 16 segments for volunteers (i) and patients (ii), at the e-wave. * indicates statistical significant differences ($p < 0.05$).

C. APPENDIX FOR PUBLICATION 3

C.1. Supplementary Material

Table C.1. Election of a number of features selected using SFS and PCA, according to the increased accuracy (mean ± standard deviation) of different classifiers with different chosen features. Each experiment was done using 10-fold cross-validation and repeated 10 times with confidence interval 95%.

Classifiers	Accuracy (%)												
	All Features	SFS						PCA					
		1	2	3	4	5	6	1	2	3	4	5	6
KNN-5	87.65 ± 3.07	83.50± 3.46	84.54 ± 3.34	83.5 ± 3.46	87.94 ± 3.04	87.65 ± 3.07	88.46 ± 2.98	73.14 ± 3.46	83.43 ± 3.46	87.94 ± 3.15	88.76 ± 3.07	86.54 ± 3.04	89.35 ± 3.07
KNN-7	84.61 ± 3.37	84.9 ± 3.34	84.25 ± 3.53	86.01 ± 3.23	86.24 ± 3.21	86.54 ± 3.18	90.69 ± 2.71	72.91 ± 3.34	87.35 ± 3.23	87.94 ± 3.15	86.83 ± 3.18	87.94 ± 3.21	87.65 ± 3.26
KNN-9	86.24 ± 3.21	88.76 ± 2.95	80.92 ± 2.81	88.24 ± 3.00	92.09 ± 2.52	88.46 ± 2.98	89.05 ± 2.91	78.17 ± 2.95	88.17 ± 3.00	85.65 ± 3.15	87.06 ± 2.98	86.24 ± 2.52	85.13 ± 2.85
LDA	93.86 ± 2.24	88.24± 3.00	83.73 ± 2.66	92.68 ± 2.43	93.56 ± 2.29	96.31 ± 1.76	95.78 ± 1.87	80.92 ± 3.00	85.49 ± 2.43	90.75 ± 2.09	91.34 ± 1.76	91.05 ± 2.29	91.08 ± 2.42
QDA	13.76 ± 3.21	88.24± 3.00	81.50 ± 2.52	89.64 ± 2.84	94.08 ± 2.20	88.27± 3.00	87.75 ± 3.06	79.28 ± 3.00	87.65 ± 2.84	92.91 ± 3.24	87.09 ± 3.00	89.35 ± 2.20	84.67 ± 2.11
Euclidean Distance	71.21 ± 4.22	83.79 ± 3.44	70.39 ± 3.12	84.08 ± 3.41	85.2 ± 3.31	87.94 ± 3.04	87.71 ± 3.06	65.95 ± 3.44	70.92 ± 3.41	73.43 ± 2.91	70.10 ± 3.04	67.88 ± 3.31	69.87 ± 3.28
Mahalanobis Distance	27.75 ± 4.18	83.5 ± 3.46	64.02 ± 3.34	84.31 ± 3.39	93.2 ± 2.35	88.92 ± 2.93	89.87 ± 2.81	70.92 ± 3.46	85.49 ± 3.39	89.51 ± 2.79	87.06 ± 2.93	92.39 ± 2.35	86.69 ± 2.15
SVM – Linear	86.83 ± 3.15	88.24 ± 3.00	83.43 ± 3.27	89.87 ± 2.81	89.87 ± 2.81	91.34 ± 2.62	86.54 ± 3.18	80.69 ± 3.00	89.28 ± 2.81	87.06 ± 2.81	88.99 ± 2.62	92.09 ± 2.81	94.08 ± 2.95
SVM - RBF	45.23 ± 4.64	88.46 ± 2.98	48.27 ± 2.98	83.2 ± 3.49	72.25 ± 4.18	61.37 ± 4.54	61.67 ± 4.53	61.90 ± 2.98	83.43 ± 3.46	44.41 ± 4.42	46.05 ± 4.54	45.23 ± 4.18	46.05 ± 4.11
Neural Network	81.80 ± 3.60	84.90 ± 3.34	83.73 ± 3.00	90.46 ± 2.74	91.05 ± 2.66	84.08 ± 3.41	84.02 ± 3.42	82.32 ± 3.34	87.35 ± 3.23	82.68 ± 3.31	83.27 ± 3.41	93.79 ± 2.66	91.06 ± 1.99
Random Forest	92.00 ± 1.80	91.00 ± 1.40	92.00 ± 1.40	93.00 ± 1.90	96.00 ± 0.75	96.00 ± 2.70	94.00 ± 2.20	86.00 ± 0.43	87.00 ± 1.40	95.00 ± 0.97	96.00 ± 0.75	96.00 ± 0.83	95.00 ± 0.67

Table C.2. Precision, specificity, sensitivity, and accuracy of different combinations of classifiers and features. Each experiment was done using 10-fold cross-validation and repeated 10 times with confidence interval 95%.

		HV class			NON-DIL BAV class			DIL BAV class			Accuracy (%)
		Precision (%)	Specificity (%)	Sensitivity (%)	Precision (%)	Specificity (%)	Sensitivity (%)	Precision (%)	Specificity (%)	Sensitivity (%)	
KNN-5	**All features**	95.00 ± 1.54	96.67 ± 7.03	93.23 ± 9.43	20.00 ± 4.22	89.30 ± 7.34	37.50 ± 4.79	95.00 ± 1.05	96.33 ± 7.77	86.36 ± 1.54	87.65 ± 3.07
	SFS	95.00 ± 1.54	96.67 ± 7.03	98.57 ± 4.52	64.44 ± 4.77	94.66 ± 7.06	64.44 ± 4.19	94.23 ± 1.04	95.81 ± 7.67	91.50 ± 1.11	87.65 ± 3.07
	PCA	94.17 ± 1.43	95.83 ± 7.67	91.36 ± 1.12	41.11 ± 5.08	91.94 ± 8.12	70.00 ± 2.74	95.96 ± 8.81	97.08 ± 6.23	90.11 ± 1.39	86.54 ± 3.04
KNN-7	**All features**	94.17 ± 1.43	95.86 ± 7.67	91.96 ± 1.06	51.11 ± 5.16	92.99 ± 8.32	78.57 ± 3.93	90.00 ± 1.29	92.17 ± 1.04	86.00 ± 1.59	84.61 ± 3.37
	SFS	100.00 ± 0.00	100.00 ± 0.00	93.5 ± 1.06	51.11 ± 5.16	92.78 ± 8.58	60.42 ± 4.54	89.23 ± 1.72	92.92 ± 1.07	93.00 ± 1.14	86.54 ± 3.18
	PCA	92.50 ± 1.08	94.67 ± 8.64	94.73 ± 9.47	43.33 ± 4.98	92.31 ± 7.13	79.17 ± 4.01	99.23 ± 2.43	99.41 ± 1.86	87.06 ± 1.15	87.94 ± 3.21
KNN-9	**All features**	95.83 ± 9.00	97.09 ± 6.65	93.83 ± 1.01	42.22 ± 5.02	92.12 ± 7.51	83.33 ± 4.08	95.00 ± 1.05	95.5 ± 9.56	86.00 ± 1.59	86.24 ± 3.21
	SFS	97.50 ± 7.91	98.33 ± 5.27	94.00 ± 9.66	52.22 ± 5.08	93.23 ± 7.79	71.43 ± 3.93	92.50 ± 1.21	95.00 ± 8.05	91.65 ± 1.08	88.46 ± 2.98
	PCA	95.00 ± 1.05	96.67 ± 7.03	96.00 ± 8.43	31.11 ± 4.77	90.77 ± 7.52	70.00 ± 4.47	96.73 ± 8.01	97.38 ± 6.41	84.83 ± 1.39	86.24 ± 2.52
QDA	**All features**	12.50 ± 3.17	61.05 ± 1.43	55.56 ± 5.09	80.00 ± 4.22	71.88 ± 4.83	10.88 ± 7.41	7.50 ± 16.87	57.9 ± 5.91	66.67 ± 5.77	13.76 ± 3.21
	SFS	95.00 ± 1.05	96.67 ± 7.03	97.50 ± 7.91	73.33 ± 4.39	95.64 ± 7.37	73.15 ± 3.72	94.23 ± 1.57	96.64 ± 9.00	94.57 ± 8.88	88.27 ± 3.00
	PCA	95.83 ± 9.00	97.50 ± 5.62	98.00 ± 6.32	65.56 ± 4.73	94.93 ± 6.68	75.69 ± 3.73	95.96 ± 8.81	97.28 ± 5.91	93.33 ± 1.09	89.35 ± 2.20
Minimum Distance	**All features**	91.67 ± 1.66	94.98 ± 9.81	95.86 ± 8.74	65.56 ± 4.73	92.76 ± 9.40	38.01 ± 3.71	55.58 ± 2.78	75.12 ± 1.44	89.05 ± 1.78	71.21 ± 4.22
	SFS	90.00 ± 1.74	93.81 ± 1.05	94.57 ± 8.88	84.44 ± 3.44	97.03 ± 6.37	57.17 ± 3.59	81.73 ± 1.62	88.28 ± 9.78	98.00 ± 6.32	87.94 ± 3.04
	PCA	90.00 ± 2.42	94.58 ± 1.24	94.00 ± 9.66	75.56 ± 4.22	94.75 ± 8.56	30.83 ± 1.89	49.62 ± 3.12	73.30 ± 1.46	85.24 ± 3.19	67.88 ± 3.31
Mahalanobis Distance	**All features**	57.50 ± 3.34	72.47 ± 2.15	58.21 ± 1.93	22.22 ± 4.16	82.67 ± 1.46	10.37 ± 1.41	45.19 ± 3.09	71.65 ± 1.22	100.00 ± 0.00	27.75 ± 4.18
	SFS	97.50 ± 7.91	98.33 ± 5.27	96.57 ± 7.35	74.44 ± 4.29	96.11 ± 6.44	79.17 ± 2.92	92.50 ± 1.69	95.48 ± 9.94	96.13 ± 8.17	88.92 ± 2.93
	PCA	92.50 ± 1.69	95.48 ± 9.94	99.23 ± 2.43	66.67 ± 4.71	94.9 ± 6.77	61.11 ± 4.17	90.00 ± 1.29	92.67 ± 9.53	91.67 ± 1.12	92.39 ± 2.35
SVM-Linear	**All features**	87.50 ± 1.77	91.00 ± 1.24	88.9 ± 1.33	74.44 ± 4.29	95.6 ± 7.18	63.00 ± 3.97	89.23 ± 1.25	92.78 ± 8.30	95.50 ± 9.56	86.83 ± 3.15
	SFS	96.67 ± 8.05	97.83 ± 5.33	95.86 ± 8.74	53.33 ± 5.02	93.27 ± 7.70	64.29 ± 3.78	92.69 ± 1.18	95.17 ± 7.80	91.14 ± 1.17	91.34 ± 2.62
	PCA	99.17 ± 2.64	99.52 ± 1.51	96.46 ± 7.54	66.67 ± 4.71	95.42 ± 5.93	66.96 ± 3.58	89.23 ± 1.25	92.50 ± 8.79	94.07 ± 9.87	92.09 ± 2.81
SVM-RBF	**All features**	5.83 ± 1.043	58.06 ± 4.18	100.00 ± 0.00	0.00 ± 0.00	87.35 ± 4.86	0.00 ± 0.00	100.00 ± 0.00	100.00 ± 0.00	45.05 ± 3.05	45.23 ± 4.64
	SFS	77.50 ± 2.49	85.92 ± 1.40	88.97 ± 1.89	0.00 ± 0.00	87.08 ± 4.79	0.00 ± 0.00	87.12 ± 1.86	89.37 ± 1.41	67.50 ± 1.15	61.37 ± 4.54
	PCA	4.17 ± 9.00	57.57 ± 4.49	100.00 ± 0.00	0.00 ± 0.00	87.35 ± 4.86	0.00 ± 0.00	100.00 ± 0.00	100.00 ± 0.00	44.62 ± 2.24	45.23 ± 4.18
Neural Network	**All features**	97.50 ± 7.91	98.33 ± 5.27	93.90 ± 1.15	75.56 ± 4.22	96.08 ± 6.36	77.78 ± 3.63	87.50 ± 2.13	92.14 ± 1.33	94.79 ± 1.15	81.80 ± 3.60
	SFS	95.83 ± 9.00	97.46 ± 5.67	97.09 ± 6.65	57.78 ± 5.02	94.62 ± 5.78	63.49 ± 4.09	90.00 ± 1.75	93.48 ± 1.09	92.79 ± 1.03	84.08 ± 3.41
	PCA	4.17 ± 9.00	57.57 ± 4.49	100.00 ± 0.00	0.00 ± 0.00	87.35 ± 4.86	0.00 ± 0.00	100.00 ± 0.00	100.00 ± 0.00	44.62 ± 2.24	93.79 ± 2.66

Table C.3. Average accuracy and standard deviation of different combinations of classifiers and features for two classes (NON-DIL BAV and DIL BAV). Each experiment was done using 10-fold cross-validation and repeated 10 times with confidence interval 95%.

	Accuracy (%)				
Classifiers	**Hemodynamic Parameters**	**Hemodynamic Parameters + Age**	**SFS**	**PCA (*)**	**PCA (**)**
KNN-5	87.91 ± 3.98	81.27 ± 4.77	85.73 ± 4.27	84.82 ± 4.38	82.36 ± 4.66
KNN-7	82.82 ± 4.61	88.36 ± 3.92	87.73 ± 4.01	86.82 ± 4.13	82.82 ± 4.61
KNN-9	80.36 ± 4.85	82.36 ± 4.66	82.36 ± 4.66	75.91 ± 5.22	87.45 ± 4.05
LDA	89.45 ± 3.75	89.73 ± 3.71	96.18 ± 2.34	82.64 ± 4.63	85.27 ± 4.33
QDA	24.09 ± 5.22	20.09 ± 4.90	92.64 ± 3.19	86.82 ± 4.13	80.82 ± 4.81
Minimum Distance	53.91 ± 6.09	57.45 ± 6.04	82.64 ± 4.63	53.91 ± 6.09	60.36 ± 5.98
Mahalanobis Distance	52.36 ± 6.10	57.45 ± 6.04	89.27 ± 3.78	86.64 ± 4.16	84.82 ± 4.38
SVM – Linear	80.82 ± 4.81	87.27 ± 4.07	93.73 ± 2.96	88.64 ± 3.88	82.18 ± 4.68
SVM - RBF	77.91 ± 5.07	77.91 ± 5.07	75.91 ± 5.22	77.91 ± 5.07	77.91 ± 5.07
Neural Network	81.27 ± 4.77	82.82 ± 4.61	88.82 ± 3.85	88.18 ± 3.94	88.64 ± 3.88
Random Forest	95.00 ± 2.80	95.00 ± 2.90	91.00 ± 1.90	95.00 ± 1.18	93.00 ± 2.10

SFS's five top-performing features were: velocity angle in AAo, regurgitation fraction in AArch, eccentricity in AAo, backward velocity in AAo, and Oscillatory Shear Index in AAo
PCA's five top-performing features were: velocity in AArch, forward velocity in AArch, velocity in AAo, kinetic energy in AArch, and forward velocity in AAo

Hemodynamic Parameters (*)
Hemodynamic Parameters + Age (**)

Table C.4. Election of the number of features selected using SFS (velocity angle, forward velocity, and vorticity) and PCA (forward velocity, velocity, and velocity angle), according to the increased in the accuracy (mean ± standard deviation) of different classifiers with different features selected, using only hemodynamic features in AAo. Each experiment was done using 10-fold cross-validation and repeated 10 times with confidence interval 95%.

Classifiers	**Accuracy (%)**								
	All features	**SFS**				**PCA**			
		1	**2**	**3**	**4**	**1**	**2**	**3**	**4**
KNN-5	89.35 ± 2.88	78.17 ± 3.85	87.35 ± 3.10	86.83 ± 3.15	87.94 ± 3.04	75.13 ± 3.85	89.80 ± 3.10	89.05 ± 3.15	90.98 ± 3.04
KNN-7	87.65 ± 3.07	87.35 ± 3.10	84.90 ± 3.34	86.54 ± 3.18	84.90 ± 3.34	81.21 ± 3.10	87.06 ± 3.34	87.35 ± 3.18	91.80 ± 3.34
KNN-9	88.99 ± 2.92	85.42 ± 3.29	89.05 ± 2.91	89.58 ± 2.85	89.05 ± 2.91	81.80 ± 3.29	86.54 ± 2.91	84.54 ± 2.85	84.31 ± 2.91
LDA	91.93 ± 2.54	89.87 ± 2.81	89.35 ± 2.88	93.27 ± 2.34	92.97 ± 2.38	77.58 ± 2.81	91.50 ± 2.88	88.76 ± 2.34	86.01 ± 2.38
QDA	53.59 ± 4.65	84.61 ± 3.37	91.27 ± 2.63	94.90 ± 2.05	89.12 ± 2.90	81.21 ± 3.37	87.94 ± 2.63	86.01± 2.05	86.54 ± 2.90
Euclidean Distance	69.80 ± 4.28	87.12 ± 3.12	87.94 ± 3.04	89.05 ± 2.91	86.83 ± 3.15	67.06 ± 3.12	71.44 ± 3.04	73.07 ± 2.91	69.05 ± 3.15
Mahalanobis Distance	56.86 ± 4.62	81.27 ± 3.64	82.16 ± 3.57	92.16 ± 2.51	91.05 ± 2.66	67.06 ± 3.64	84.61 ± 3.57	84.90 ± 2.51	81.05 ± 2.66
SVM – Linear	89.05 ± 2.91	85.72 ± 3.26	89.05 ± 2.91	89.35 ± 2.88	87.88 ± 3.04	81.50 ± 3.26	89.05 ± 2.91	87.71 ± 2.88	89.58 ± 3.04
SVM - RBF	48.86 ± 4.66	86.54 ± 3.18	88.46 ± 2.98	67.22 ± 4.38	70.26 ± 4.26	57.81 ± 3.18	50.49 ± 2.98	46.05 ± 4.38	45.52 ± 4.26
Neural Network	85.95 ± 3.24	87.94 ± 3.04	87.42 ± 3.09	91.86 ± 2.55	86.83 ± 3.15	81.50 ± 3.04	87.94 ± 3.09	90.69 ± 2.55	87.35 ± 3.15
Random Forest	94.00 ± 2.60	78.17 ± 3.85	87.35 ± 3.10	94.00 ± 2.00	87.94 ± 3.04	75.13 ± 3.85	89.80 ± 3.10	92.00 ± 0.99	90.98 ± 3.04

Table C.5. Precision, specificity, sensitivity, and accuracy of different combinations of classifiers and features in AAo. Each experiment was done using 10-fold cross-validation and repeated 10 times with confidence interval 95%.

		HV class			NON-DIL BAV class			DIL BAV class			Accuracy (%)
		Precision (%)	Specificity (%)	Sensitivity (%)	Precision (%)	Specificity (%)	Sensitivity (%)	Precision (%)	Specificity (%)	Sensitivity (%)	
KNN-5	**All features**	92.50 ± 1.69	95.14 ± 1.04	94.07 ± 9.87	62.22 ± 4.92	94.34 ± 7.90	66.67 ± 3.88	95.00 ± 1.05	96.67 ± 7.03	95.22 ± 1.02	89.35 ± 2.88
	SFS	97.50 ± 7.91	98.33 ± 5.27	96.57 ± 7.35	44.44 ± 4.97	92.50 ± 6.65	61.90 ± 4.88	92.50 ± 1.69	95.14 ± 1.04	89.63 ± 1.11	86.83 ± 3.15
	PCA	95.00 ± 1.05	96.33 ± 7.77	96.07 ± 8.66	51.11 ± 5.16	92.78 ± 8.58	56.25 ± 4.17	94.23 ± 1.04	95.71 ± 7.69	90.17 ± 1.32	89.05 ± 3.15
KNN-7	**All features**	95.00 ± 1.05	96.67 ± 7.03	96.57 ± 7.35	51.11 ± 5.16	92.92 ± 8.50	64.29 ± 3.78	96.73 ± 8.01	97.71 ± 5.42	90.67 ± 1.27	87.65 ± 3.07
	SFS	97.50 ± 7.91	98.33 ± 5.27	96.57 ± 7.35	44.44 ± 4.97	92.50 ± 6.65	61.90 ± 4.88	92.5 ± 1.69	95.14 ± 1.04	89.63 ± 1.11	86.54 ± 3.18
	PCA	95.00 ± 1.05	96.67 ± 7.03	96.57 ± 7.35	51.11 ± 5.16	93.06 ± 8.41	75.00 ± 2.74	96.73 ± 8.01	97.71 ± 5.42	89.33 ± 1.45	87.35 ± 3.18
KNN-9	**All features**	96.67 ± 8.05	97.86 ± 5.32	95.13 ± 1.11	41.11 ± 5.08	92.02 ± 7.95	70.00 ± 2.74	92.50 ± 1.21	95.00 ± 8.05	88.50 ± 1.29	88.99 ± 2.92
	SFS	97.50 ± 7.91	98.33 ± 5.27	92.00 ± 1.03	33.33 ± 4.71	91.12 ± 6.60	58.33 ± 4.92	92.50 ± 1.69	95.48 ± 9.94	90.13 ± 1.04	89.58 ± 2.85
	PCA	92.50 ± 1.21	94.67 ± 8.64	94.73 ± 9.47	52.22 ± 5.08	92.98 ± 8.11	73.81 ± 3.83	96.73 ± 8.01	97.38 ± 6.41	90.17 ± 1.32	84.54 ± 2.85
LDA	**All features**	99.17 ± 2.64	99.50 ± 1.58	97.86 ± 6.78	86.67 ± 3.22	97.78 ± 4.68	81.75 ± 2.43	91.73 ± 1.18	94.52 ± 7.86	97.23 ± 6.52	91.93 ± 2.54
	SFS	100.00 ± 0.00	100.00 ± 0.00	97.23 ± 6.52	67.78 ± 4.73	95.80 ± 5.47	94.81 ± 1.37	96.92 ± 9.73	98.33 ± 5.27	95.00 ± 8.50	93.27 ± 2.34
	PCA	100.00 ± 0.00	100.00 ± 0.00	96.00 ± 8.43	53.33 ± 5.02	93.14 ± 7.61	63.89 ± 4.86	91.73 ± 1.18	94.04 ± 8.43	92.17 ± 1.30	88.76 ± 2.34
QDA	**All features**	87.50 ± 3.17	94.80 ± 1.18	95.56 ± 8.82	70.00 ± 4.83	96.30 ± 5.56	89.50 ± 2.78	90.00 ± 3.16	96.18 ± 1.21	95.56±8.82	53.59 ± 4.65
	SFS	97.50 ± 7.91	98.33 ± 5.27	98.57 ± 4.52	75.56 ± 4.22	96.26 ± 6.06	77.78 ± 3.63	95.00 ± 1.05	96.67 ± 7.03	94.67±8.78	94.90 ± 2.05
	PCA	99.17 ± 2.64	99.55 ± 1.44	99.17 ± 2.64	43.33 ± 4.98	92.06 ± 7.42	60.00 ± 3.74	88.46 ± 1.72	92.16 ± 1.15	85.14±13.94	86.01 ± 2.05
Minimum Distance	**All features**	90.00 ± 1.29	92.17 ± 1.04	90.73 ± 1.42	34.44 ± 4.73	88.97 ± 7.99	16.42 ± 2.11	51.15 ± 2.66	71.94 ± 1.32	81.67±21.08	69.80 ± 4.28
	SFS	93.33 ± 1.61	96.23 ± 9.17	96.33 ± 7.77	77.78 ± 4.16	96.59 ± 5.57	49.17 ± 3.39	82.69 ± 1.19	88.42 ± 8.19	97.50 ± 7.91	89.05 ± 2.91
	PCA	95.00 ± 1.05	97.08 ± 6.23	93.00 ± 9.49	44.44 ± 4.97	90.80 ± 9.01	18.33 ± 1.58	53.85 ± 2.88	73.97 ± 1.51	84.72 ± 2.08	73.07 ± 2.91
Mahalanobis Distance	**All features**	87.50 ± 3.17	94.80 ± 1.18	100.00 ± 0.00	58.89 ± 5.08	85.56 ± 3.06	87.37 ± 3.09	90.00 ± 3.16	96.06 ± 1.25	80.00 ± 2.98	56.86 ± 4.62
	SFS	96.67 ± 8.05	97.88 ± 5.31	97.17 ± 6.58	78.89 ± 4.17	97.38 ± 4.64	69.44 ± 3.06	87.50 ± 2.13	92.62 ± 1.23	98.00 ± 6.32	92.16 ± 2.51
	PCA	87.50 ± 2.43	92.92 ± 1.27	98.00 ± 6.32	67.78 ± 4.73	95.62 ± 5.80	43.06 ± 3.49	84.23 ± 1.69	89.64 ± 1.06	94.07 ± 9.87	84.90 ± 2.51
SVM-Linear	**All features**	95.00 ± 1.05	96.75 ± 7.08	92.50 ± 1.04	64.44 ± 4.77	94.54 ± 7.31	61.90 ± 4.15	90.00 ± 1.75	93.81 ± 1.05	95.65 ± 9.21	89.05 ± 2.91
	SFS	95.00 ± 1.05	96.67 ± 7.03	96.00 ± 8.43	43.33 ± 4.98	91.99 ± 7.37	60.71 ± 4.53	94.23 ± 1.04	95.81 ± 7.67	89.50 ± 1.12	89.35 ± 2.88
	PCA	95.00 ± 1.05	96.67 ± 7.03	95.23 ± 8.38	27.78 ± 4.51	90.94 ± 4.91	27.27 ± 3.03	89.42 ± 1.38	93.00 ± 9.09	88.50 ± 1.06	87.71 ± 2.88
SVM-RBF	**All features**	11.67 ± 1.26	59.65 ± 4.70	100.00 ± 0.00	0.00 ± 0.00	87.35 ± 4.86	0.00 ± 0.00	100.00 ± 0.00	100.00 ± 0.00	46.28 ± 3.40	48.86 ± 4.66
	SFS	61.67 ± 2.76	78.45 ± 1.56	88.00 ± 1.78	0.00 ± 0.00	87.21 ± 4.83	0.00 ± 0.00	97.50 ± 7.91	96.67 ± 1.54	65.17 ± 1.67	67.22 ± 4.38
	PCA	5.00 ± 1.05	57.86 ± 3.76	100.00 ± 0.00	0.00 ± 0.00	87.35 ± 4.86	0.00 ± 0.00	100.00 ± 0.00	100.00 ± 0.00	44.93 ± 3.30	46.05 ± 4.38
Neural Network	**All features**	86.67 ± 1.26	90.11 ± 9.48	89.38 ± 1.38	45.56 ± 4.98	92.55 ± 6.49	58.93 ± 4.97	88.65 ± 1.52	91.83 ± 1.06	82.44 ± 1.27	85.95 ± 3.24
	SFS	95.00 ± 1.05	96.33 ± 7.77	96.73 ± 8.01	75.56 ± 4.22	96.35 ± 5.94	83.33 ± 2.67	94.23 ± 1.04	96.14 ± 6.95	94.00 ± 9.66	91.86 ± 2.55
	PCA	99.17 ± 2.64	99.55 ± 1.44	99.17 ± 2.64	43.33 ± 4.98	92.3 ± 7.33	70.00 ± 2.74	93.46 ± 1.09	95.56 ± 7.31	86.88 ± 1.18	90.69 ± 2.55
Random Forest	**All features**	99.73 ± 1.13	99.81 ± 0.77	96.85 ± 1.30	76.04 ± 7.72	95.70 ± 1.29	90.37 ± 9.79	96.67 ± 4.40	97.60 ± 2.93	94.49 ± 2.22	94.00 ± 2.60
	SFS	98.91 ± 2.97	99.24 ± 2.02	95.80 ± 0.76	67.26 ± 7.91	94.23 ± 1.25	89.13 ± 9.62	97.61 ± 2.02	98.19 ± 1.51	92.75 ± 2.42	94.00 ± 2.00
	PCA	97.41 ± 0.78	98.10 ± 0.55	93.97 ± 1.02	69.87 ± 5.10	94.52 ± 0.84	78.68 ± 4.39	95.46 ± 1.61	96.65 ± 1.12	95.10 ± 1.12	92.00 ± 0.99

Table C.6. Average accuracy and standard deviation of different combinations of classifiers and features for three classes (HV, NON-DIL BAV, and DIL BAV). Each experiment was done using 10-fold cross-validation and repeated 10 times with confidence interval 95%.

	Accuracy (%)				
Classifiers	**Hemodynamic Parameters**	**Hemodynamic Parameters + Age**	**SFS**	**PCA (*)**	**PCA (**)**
KNN-5	87.65 ± 3.07	85.42 ± 3.29	87.65 ± 3.07	86.54 ± 3.04	87.35 ± 3.10
KNN-7	84.61 ± 3.37	84.84 ± 3.34	86.54 ± 3.18	87.94 ± 3.21	84.31 ± 3.39
KNN-9	86.24 ± 3.21	89.87 ± 2.81	88.46 ± 2.98	86.24 ± 2.52	86.24 ± 3.21
LDA	93.86 ± 2.24	93.86 ± 2.24	96.31 ± 1.76	91.05 ± 2.29	93.04 ± 2.37
QDA	13.76 ± 3.21	15.98 ± 3.42	88.27 ± 3.00	89.35 ± 2.20	12.65 ± 3.10
Minimum Distance	71.21 ± 4.22	67.12 ± 4.38	87.94 ± 3.04	67.88 ± 3.31	70.10 ± 4.27
Mahalanobis Distance	27.75 ± 4.18	37.97 ± 4.53	88.92 ± 2.93	92.39 ± 2.35	48.86 ± 4.66
SVM – Linear	86.83 ± 3.15	86.01 ± 3.23	91.34 ± 2.62	92.09 ± 2.81	77.71 ± 3.88
SVM - RBF	45.23 ± 4.64	45.23 ± 4.64	61.37 ± 4.54	45.23 ± 4.18	46.05 ± 4.65
Neural Network	81.80 ± 3.60	89.05 ± 2.91	84.08 ± 3.41	93.79 ± 2.66	89.35 ± 2.88
Random Forest	92.00 ± 1.80	92.00 ± 1.90	96.00 ± 2.70	96.00 ± 0.83	96.00 ± 0.78

SFS's five top-performing features were: velocity angle in AAo, forward velocity in AAo, helicity density in AArch, vorticity in AAo, and backward velocity in AAo

PCA's five top-performing features were: forward velocity in AAo, velocity in AArch, velocity in AAo, velocity angle in AAo, and kinetic energy in AArch.

Hemodynamic Parameters (*)
Hemodynamic Parameters + Age (**)

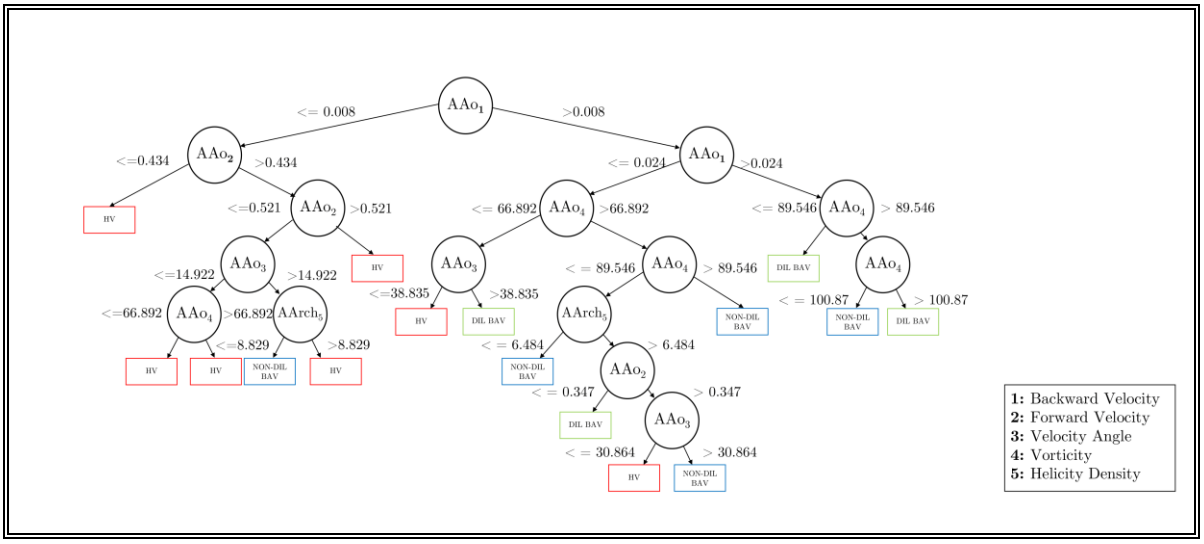

Figure C.1. Schematic diagram of random forest with five features selected by SFS. Random forest has nodes, and every node includes a feature ID and split threshold.

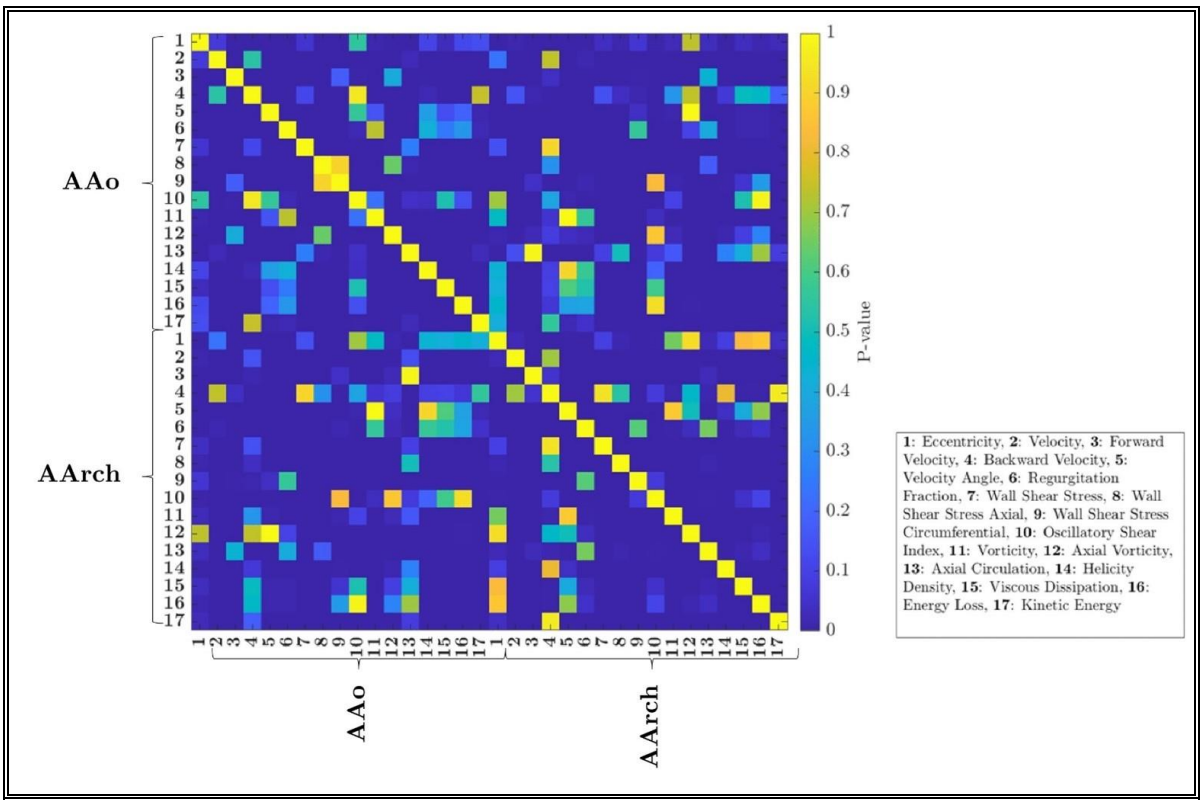

Figure C.2. Correlation matrix (p-values) obtained by the linear regression between all hemodynamic parameters of volunteers and BAV patients, for AAo and AArch regions.

D. SUMMARY OF PARTICIPATION IN OTHER RESEARCH PROJECTS

D.1. Research Articles

- Franco P, Ma Liliana, Schnell S, Carrillo H, Montalba C, Markl M, Bertoglio C, Uribe S. Comparison of and Improved Uni-Directional Dual Velocity-Encoding MRI Methods. *J Magn Reson Imaging*. 2022.
- Sotelo J, Franco P, Ruiz-Muñoz A, Evangelista A, Mella H, Mura J, Hurtado D, Rodríguez-Palomares J, Uribe S. Fully Three-Dimensional Hemodynamic Characterization of Altered Blood Flow in Bicuspid Aortic Valve Patients With Respect to Aortic Dilatation: A Finite Element Approach. *Front Cardiovasc Med*. 2022. doi:10.3389/fcvm.2022.885338

- Franco P, Sotelo J, Guala A, Dux-Santoy L, Evangelista A, Rodríguez-Palomares J, Mery D, Salas R, Uribe S, Identification of hemodynamic biomarkers for bicuspid aortic valve induced aortic dilation using machine learning, *Computers in Biology and Medicine*, Volume 141, 2022, 105147, ISSN 0010-4825, https://doi.org/10.1016/j.compbiomed.2021.105147.
- Franco P, Sotelo J, Montalba C, Ruijsink B, Kerfoot E, Nordsletten D, Mura J, Hurtado D, Uribe S, Comprehensive Assessment of Left Intraventricular Hemodynamics Using a Finite Element Method: An Application to Dilated Cardiomyopathy Patients, *Appl. Sci.* 2021, 11, 11165
- Giannini E, Franco P, Montalba Z, López D, Astudillo C. Neurología por Resonancia Magnética: Aspectos técnicos y aplicaciones técnicas. *Rev Chil Radiol*, 2021; vol.27, n.2, pp.88-103. ISSN 0717-9308. http://dx.doi.org/10.4067/S0717-93082021000200088.

D.2. International Conferences

- 'Identification of Subcortical White Matter Biomarkers in Multiple Sclerosis Patients according to AVLT Performance using Random Forest, digital poster and second author, ISMRM 31st annual meeting, London, UK, 7-12 May 2022
- 'Identification of Hemodynamic Biomarkers for Bicuspid Aortic Valve induced Aortic Dilation using Machine Learning', oral presentation and first author, ISMRM 31st annual meeting, London, UK, 7-12 May 2022
- 'A Review and Comparison of Unwrapping Methods in Dual Velocity-Encoding MRI', poster presentation and first author, ISMRM 31st annual meeting, London, UK, 7-12 May 2022
- 'Identification of Hemodynamic Biomarkers for Bicuspid Aortic Valve induced Aortic Dilation using Machine Learning', oral presentation and first author, SCMR 25th scientific sessions, 2-5 February 2022
- 'A Review and Comparison of Unwrapping Methods in Dual Velocity-Encoding MRI', poster presentation and first author, SCMR 25th scientific sessions, 2-5 February 2022

- ‘Identification of Hemodynamic Biomarkers for Bicuspid Aortic Valve Patients using Machine Learning’, poster presentation and first author, ISMRM 30th annual meeting, Virtual Conference & Exhibition, 15-20 May 2021
- ‘Left Ventricular Reverse Remodeling in Dilated Cardiomyopathy: Does Ejection Fraction Reflect Subtle Ventricular Dysfunction?’, poster presentation and first author, ISMRM 29th annual meeting, Virtual Conference & Exhibition, 08-14 August 2020
- ‘Sensitivity Study of 4D Flow Left Ventricular Hemodynamics Parameters in Healthy Volunteers and Dilated Cardiomyopathy Patients’, oral presentation and first author, ISMRM 28th annual meeting, Montréal, Canada, 11-16 May 2019
- ‘Comprehensive 3D flow characterization in patients with Dilated Cardiomyopathy (DCM) from 4D Flow MRI data using a finite element method and 17- Segment Bullseyes’, oral presentation and first author, ISMRM 27th annual meeting, Paris, France, 16-21 Jun 2018
- ‘A model of tumour response to radiation considering 3D vascular architectures and vascular damage’, poster presentation and co-author, ESTRO 37, Barcelona, Spain, 20-24 April 2018
- ‘Comprehensive 3D flow characterization in patients with Dilated Cardiomyopathy (DCM) from 4D Flow MRI data using a finite element method and 17- Segment Bullseyes’, poster presentation and first author, 5th Edition CMR, Barcelona, Spain, 31 January – 03 February 2018
- ‘Comprehensive 3D flow characterization in patients with Dilated Cardiomyopathy (DCM) from 4D Flow MRI data using a finite element method and 17- Segment Bullseyes’, oral presentation and first author, ISMRM Workshop on Magnetic Resonance Imaging of Cardiac Function, New York, USA, 17- 20 August 2017

D.3. National Conferences

- ‘Identification of Hemodynamic Biomarkers for Bicuspid Aortic Valve Patients using Machine Learning’, oral presentation and first author, Workshop: Avances en Resonancia Magnética Cardiovascular – CardioMR, 2021
- ‘Caracterización del flujo 4D obtenido por resonancia magnética mediante el uso de elementos finitos: aplicado a pacientes con miocardiopatía dilatada’, poster presentation and first author, LIV Congreso Chileno de Cardiología y Cirugía Vascular’, Santiago, Chile, 01 Dic 2018.
- ‘Caracterización del flujo 4D obtenido por resonancia magnética en pacientes con miocardiopatía dilatada y el uso de elementos finitos’, oral presentation and first author, XVI Jornada de Mécanica Computacional, La Serena, Chile, 05-06 October 2017
- ‘Estimación semi-automática de velocidad de onda en arterias mediante 4D Flow MRI, oral presentation and co-author, XVI Jornada de Mécanica Computacional, La Serena, Chile, 05-06 October 2017
- ‘Caracterización del flujo 4D obtenido por resonancia magnética mediante el uso de elementos finitos: aplicado a pacientes con miocardiopatía dilatada’, oral presentation and first author, II Congreso de Estudiantes de Ingeniería de USM y PUC, Valparaíso, Chile, 1 September 2017